JAERI-M
8510

IAEA INTOR WORKSHOP REPORT, GROUP 6
— MATERIALS —

October 1979

Kensuke SHIRAISHI, Tatsuo KONDO, Shoichi NASU
Saburo TAKAMURA , Tatsuo OKU and Yoshio
MURAKAMI

日　本　原　子　力　研　究　所
Japan Atomic Energy Research Institute

JAERI-M 8510

IAEA INTOR Workshop Report, Group 6
——Materials——

Kensuke SHIRAISHI, Tatsuo KONDO, Shoichi NASU
Saburo TAKAMURA†, Tatsuo OKU†† and Yoshio MURAKAMI†††
Division of Nuclear Fuel Research,
Tokai Research Establishment, JAERI

(Received September 27, 1979)

For materials data base assessment, selected propertics of the materials important in INTOR are evaluated on the basis of data obtained in Japan. Materials covered are austenitic steels, non-magnetic steels, and titanium alloys as structural materials; helium and water for coolant; lithium oxide for breeder; aluminum and copper for stabilizer and organic insulator as magnet materials; graphite for non-metallic materials.

Key words ; INTOR, Tokamak Reactor, Fusion Reactor, Materials Structural Materials, Stainless Steel, Non-magnetic Steel, Titainum Alloys, Helium, Lithium Oxide, Super-Conducting Magnet Stabilizer, Thermal Insulator, Electrical Insulator, Graphite, Radiation Damage.

---

†)Division of Physics, Tokai Research Establishment, JAERI

††)Division of High Temperature Engineering, Tokai Research Establishment, JAERI

†††)Division of Thermonuclear Fusion Research, Tokai Research Establishment, JAERI

IAEA INTOR ワークショップ検討報告書・グループ 6
－材　料－

日本原子力研究所東海研究所燃料工学部
白石健介・近藤達男・那須昭一・高村三郎[+]
奥　達雄[++]・村上義夫[+++]

（1979年9月27日 受理）

INTORの設計に用いる材料を選択するためのデータベースの現状を把握することを目的として，構造材料としてはステンレス鋼，非磁性鋼およびチタン合金，冷却材としてはヘリウムおよび水，トリチウム増殖材としては酸化リチウム，磁石材料としては安定材であるアルミニウム，銅，および有機絶縁材，非金属材料としては黒鉛を採りあげ，日本国内で得られる材料物性のデータを調査収集し，INTORでの使用の可能性，使用中の特性変化について考察を加えた。

[+] 東海研究所物理部

[++] 東海研究所高温工学室

[+++] 東海研究所核融合研究部

Contents

1. Introduction 1

2. Data Base for Structural Material Choice (Shiraishi, K.) ... 3

3. Data Base for Coolant Choice (Kondo, T.) 30

4. Data Base for Breeder Choice (Nasu, S.) 38

5. Data Base for Magnet Material Choice (Takamura, S.) 63

6. Data Base for Non-Metallic Material Choice (Oku, T.) 76

Appendix Homework between Sessions 2 and 3 90

目　　　次

1. 序 ………………………………………………………………………… 1
2. 構造材料選定のためのデータベース（白石健介） ………………………… 3
3. 冷却材選定のためのデータベース（近藤達男） …………………………… 30
4. 増殖材選定のためのデータベース（那須昭一） …………………………… 38
5. 磁石材料選定のためのデータベース（高村三郎） ………………………… 63
6. 非金属材料選定のためのデータベース（奥　達雄） ………………………… 76

付録

第２会期から第３会期までに行った検討事項 ……………………………… 90

1. INTRODUCTION

Essential features of INTOR for material choice are as follows:

average neutron wall loading	1 MW/m^2
burning duration	200 sec
dwelling time	100 sec including start-up and shut-down
operation mode	1 month continuous operation three times operation per year
reactor life	10 years
divertor	yes/no
heat load to first wall	
with divertor	10-20 w/cm^2
without divertor	30 w/cm^2
heat load to divertor plate	100-200 w/cm^2
sputtering and other surface characteristics	

At choice of INTOR material, it is almost impossible to expect new development of material within five years. Naturally, materials will be chosen from available ones or moderately modefied ones. The material choice of INTOR is summarized in Table 1.

Table 1 Main Mateirals of INTOR

Components	Material	Max. Temperature
Torus Material		
protection wall	low Z material or low Z covered refractory metal (e.g. TZM)	1400 °C
coolant pannel	SUS 316 (He cooled)	400
blanket vessel	SUS 316 (He cooled)	400
shielding block	SUS 316 (water cooled)	250
primary shield	stainless steel + tungsten + borated water (coolant)	150
additional sheild	Pb or Pb compound	50
blanket breeding material	Li_2O (He cooled)	550
vacuum vessel	stainless steel (water cooled)	150
Divertor Material		
divertor plate	low z coated copper base alloy (He or water cooled) or any other suitable material	300
Coil Material		
toroidal field coil		
conductor	Nb_3Sn + Cu	
insulator	epoxy - glass - fibre etc.	
structural material	stainless steel	
poloidal field coil		
conductor	NbTi + Cu with some of normal conductor of Cu	
insulator	epoxy - glass - fibre etc.	
structural material	stainless steel	

2. DATA BASE FOR STRUCTURAL MATERIALS CHOICE

A. Selected Properties of Unirradiated Alloy Important to INTOR

1. Austenitic Steel

Austenitic stainless steel have widely been used as corrosion- and heat-resisting material. No serious problems are considered to arise on industrial capability, fabrication, welding and compatibility with helium below 500°C. Type 304 and 316 steels have a large body of data on neutron irradiation damage in fast breeder reactors. The 316 steel is superior to the 304 steel in mechanical properties at elevated temperature and resistance to neutron irradiation damage. The report reviews briefly on the mechanical properties of Type 316 stainless steel.

Tensile properties of Type 316 steel is given in Fig. 2.A.1.1 as a function of test temperature. Although strength of the steel decreases with increase in test temperature, a little change in the strength is observed in the temperature range from 200 to 500°C. The tensile properties of welded joint are shown in Fig. 2.A.1.2; fracture occurs in the base metal at temperatures below 500°C.

Creep-rupture strengths of Type 316 steel at temperatures of 600, 700 and 800°C are shown in Fig. 2.A.1.3. The rupture strength at lower temperatures can be estimated with Fig. 2.A.1.4 and 5; the strength at 500°C in 10^5 hr is about 25 kg/mm^2. For creep-rupture properties, welded joint is compared with base and weld metals in Fig. 2.A.1.6. As welded condition, creep-rupture strength is lower in welded joint than in base and weld metals themselves and fracture of the welded joint occurs in the base metal. When the welded joint is heated to 950°C for 1 hr, the joint ruptures at weldment in testing at 650°C.

Fatigue properties of Type 316 steel is shown in Fig. 2.A.1.7; solid and dotted lines indicate that the fatigue specimens used were cooled with air and water, respectively. Strength at fatigue limit of the steel is shown in Fig. 2.A.1.8 as a function of test temperature; the strength is about 20 kg/mm^2 at temperatures of 200 to 500°C. Low cycle fatigue data at 300 and 550°C are given in Figs. 2.A.1.9 ~ 11. Effect of atmosphere on the fatigue properties is not observed in testing at 300°C; the fatigue life is longer in vacuum than in air at 550°C.

Probability for stress corrosion cracking of Type 316 steel in high temperature and high pressure water is compared in Fig. 2.A.1.12 with other austenitic stainless steels.

References

1) Kobe Steel, Ltd. : The Elevaled Temperature Properties of Type 304, 316, 321 and 347 Stainless Steel Tubes (1972).
2) Nippon Steel Co. : Stainless Steel Technical Data (1978).
3) Report on Fusion Reactor Materials Subcomittee in the 122 Committee of Japan Society for the Promotion of Science (1976).
4) ibid. No.3 (1978).

2. High Manganese Non-Magnetic Steel

In JT-60, three kinds of high manganese non-magnetic steel are used for toroidal field coil case, poloidal field coil case, coil spacer, structural supports, etc.; 14Mn - 2Cr - 2Ni (30 kg/mm^2), 18Mn - 5 Cr (30 kg/mm^2), and 18Mn - 5Cr (40 kg/mm^2). The specifications for the steel with permeability of $\leq$ 1.02 at 100 Oe are as follows:

Chemical Compositions (%)

Materials	C	Si	Mn	P	S	Ni	Cr	N	V
14Mn-2Cr-2Ni (30 kg/mm^2)	0.55 ~0.65	<0.50	13.0 ~14.0	<0.030	<0.010	1.80 ~2.20	1.80 ~2.20	0.01 ~0.03	-
18Mn-5Cr (30 kg/mm^2)	0.40 ~0.60	0.20 ~0.65	16.00 ~20.00	<0.08	<0.025	<2.00	3.50 ~6.00	-	-
18Mn-5Cr (40 kg/mm^2)	0.40 ~0.60	0.20 ~0.65	16.00 ~20.00	<0.08	<0.025	<2.00	3.50 ~6.00	0.08 ~0.20	0.10 ~0.30

Mechanical Properties at Room Temperature

Materials	Tensile Test			Bent Test	
	Proof Stress (kg/mm^2)	Tensile Stress (kg/mm^2)	Elongation (%)	Bend Angle	Ratio of Inside Diameter to Thickness of Specimen
14Mn-2Cr-2Ni (30 kg/mm^2)	>30	>60	>30	180°	1.5
18Mn-5Cr (30 kg/mm^2)					
18Mn-5Cr (40 kg/mm^2)	>40	>80	>30	180°	1.5

Charpy V-Notch Impact Value

Materials	Test Temperature (°C)	Impact Value ($kg \cdot m/cm^2$)	
		Average	Minimum
14Mn-2Cr-2Ni (30 kg/mm^2) 18Mn-5Cr (30 kg/mm^2) 18Mn-5Cr (40 kg/mm^2)	0	>5	>3.5

The materials can be strengthened by cold working without increase in permeability (Figs. 2.A.2.1 and 2). Fatigue properties of 18Mn-5Cr steel (30 kg/mm^2) at room temperature are shown in Figs. 2.A.2.3~5. The steel can easily welded without preheating; a little hardeness change is observed in welded joint of 18Mn-5Cr steel with 14Mn-2Cr steel (Fig. 2.A.2.6).

References

1) Kobe Steel, Ltd. : private communication

2) The Japan Steel Works, Ltd. : private communication

3. Titanium Alloys

Titanium and some of its alloys are well-established industrial materials and are annually produced about 6,000 ton in Japan. The materials are used aero-industry and chemical plants for their high strength-weight ratio and good resistance to chemicals.

Tensile properties of Ti-6Al-4V, Ti-5Al-2Cr-1Fe and Ti-13V-11Cr-3Al alloys are shown in Figs. 2.A.3.1~3 as a function of testing temperature. The ratio of tensile strength in notched specimen to that in smoothed specimen is given in Figs. 2.A.3.4 and 5 for Ti-6Al-4V alloy. The alloy is strengthened with the notch in tensile testing.

The alloy Ti-6Al-4V has good creep-rupture properties at temperatures up to 500°C as shown in Fig. 2.A.3.6, although long term rupture strength drops steeply at a temperature of 500°C.

Fatigue property of Ti-6Al-4V at room temperature is given in Fig. 2.A.3.7; The fatigue limit to tensile strength ratio is relatively high, 0.53~0.58. The fatigue limit is markedly reduced in notched or roughly-finished surface specimen of the alloy. Sampling direction to the cold rolling also affects the fatigue property (Fig. 2.A.3.8).

Impact strength of Ti-6Al-4V decreases as lowering the test temperature (Fig. 2.A.3.9); V-notch impact energy at room temperature is about 3.5 $kg \cdot m/cm^2$. Fracture toughness of the alloy is shown in Fig. 2.A.3.10 as a function of test temperature.

The alloy Ti-6Al-4V has good weldability and a little change in hardness is observed in the welded joint (Fig. 2.A.3.11). Although tensile and creep-rupture properties are not much affected with welding, impact and fatigue strengths are greatly reduced by welding (Figs. 2.A.3.12~16).

Stress corrosion cracking sensitivity in chloride and change in tensile property with with oxygen and hydrogen contents are shown in Figs. 2.A.3.17~19 for Ti-6Al-4V alloy.

References

1) Kobe Steel, Ltd. : Titanium Alloys - Groperties in general and Heat Resistance, No.612040.

2) Kobe Steel, Ltd. : Titanium Alloy, KS130AV (Ti-6Al-4V), No.612010.

3) Kobe Steel, Ltd. : Welding of Titanium and its Alloys, No.61071.

B. Irradiation Effects on Structural Steels

1. Austenitic Steel

Alloy development programs for core materials in liquid metal cooled fast breeder reactor have been in progress at Power Reactor and Nuclear Fuel Development Coporation in cooperation with Kobe Steel, Ltd., Sumitomo Metal Industries, Ltd., Tokyo Shibaura Electric Co., Ltd., National Research Institute for Metals, Japan Atomic Energy Research Institute and University of Tokyo.

A program is modification of Type 316 steel with change in minior constituent elements in order to increase high temperature creep strength and to reduce void swelling. The elements considered in the program are carbone, silicon, phosphorus, boron, molybdenum, niobium, titanium and zirconium.

Development of advanced materials is the other program. Contents of nickel and chromium, and also combined effect of the minor elements are investigated in terms of high temperature strength and swelling behavior.

The candidate materials in the programs are primarily selected with high temperature tensile tests, creep-rupture tests at 700°C and swelling behavior in ion and electron irradiations. The selected materials will be irradiated in Mark II core of experimental breeder reactor, "JOYO".

C. General Comments on Wall loading and Lifetime Considerations

In the austenitic stainless steel (Type 316), ductility loss and void swelling are supposed to be enhanced by He-production when the temperature exceeds 500°C under fusion reactor irradiation environment.

The effect of the transmuted He on the mechanical properties and also on the dimensional change is expected, for the first approximation, to be smaller than the effect of atomic displacements when the irradiation is made at temperatures below 500°C, so long as abnormally high concentration of He is not produced in the material.

Neutron wall loading of 1 MW/m^2 is appropriate for INTOR, because the wall loading corresponds to a flux of 0.8×10^{15} $n/cm^2 \cdot sec$ ($En > 0.1$ MeV) in a fast breeder reactor based on atomic displacement rate in the stainless steel.

The flux is a little smaller than the flux of core region of fast breeder reactors. Thus, the radiation damage of the steel in INTOR can be estimated with experimental data for core materials in the fast breeder reactor; it should be confirmed that the transmuted He does not enhance the radiation damage at the maximum temperature of the first wall.

The maximum temperature is designed to be about 400°C, because swelling increases abruptly at around 450°C for highly irradiated Type 316 steel.

Cold-worked stainless steel shows smaller swelling and less embrittlement than solution annealed materials when the irradiation is made at temperatures below 500°C.

The lifetime of 6 $MW \cdot yr/m^2$ may be expected in cold worked Type 316 steel used at temperature of 400°C and below. The lifetime is equivalent to 1.4×10^{23} n/cm^2 irradiation in a fast breeder reactor, which produces ~2% in swelling.

Ductility of the steel after 6 MW·yr/m^2 irradiation at 400°C is anticipated to be more than 2% in total elongation; more reduction in ductility with radiation hardening may arise at lower temperatures.

Limited irradiation data preclude the opimization of design and operation conditions in terms of neutron wall loading, maximum temperature and lifetime of the first wall material.

Much effort is required to predict radiation damage of the austenitic stainless steel under fusion reactor environments.

Experiments with the fast breeder reactor and the high flux mixed-spectrum reactor are, respectively, useful for evaluation of displacement damage at relatively low temperatures ($\lesssim$ 450°C) and synergetic effect of He to the displacements at higher temperatures ($\gtrsim$ 450°C).

Dual ion beam, say Ni$^+$ and He$^+$ irradiation in accelerators is also beneficial to understand the radiation damage in fusion reactor environment.

Correlation of neutron irradiation damage in the fusion reactor with the damage in fission reactors and accelerators must be established; theoretical and experimental studies for damage analysis as well as experiments with 14 MeV intense neutron sources are required for establishment of the correlation.

As a function of neutron fluence, He content and temperature, experimental data are urgent to accumulate for following properties:

Tensile properties
Swelling with and without applied stress
Creep under irradiation
Interaction between swelling and creep deformations
Post-irradiation fatigue properties (Crack initiation, crack propagation and life)
Fatigue properties under irradiation
Interaction of fatigue with creep under irradiation.

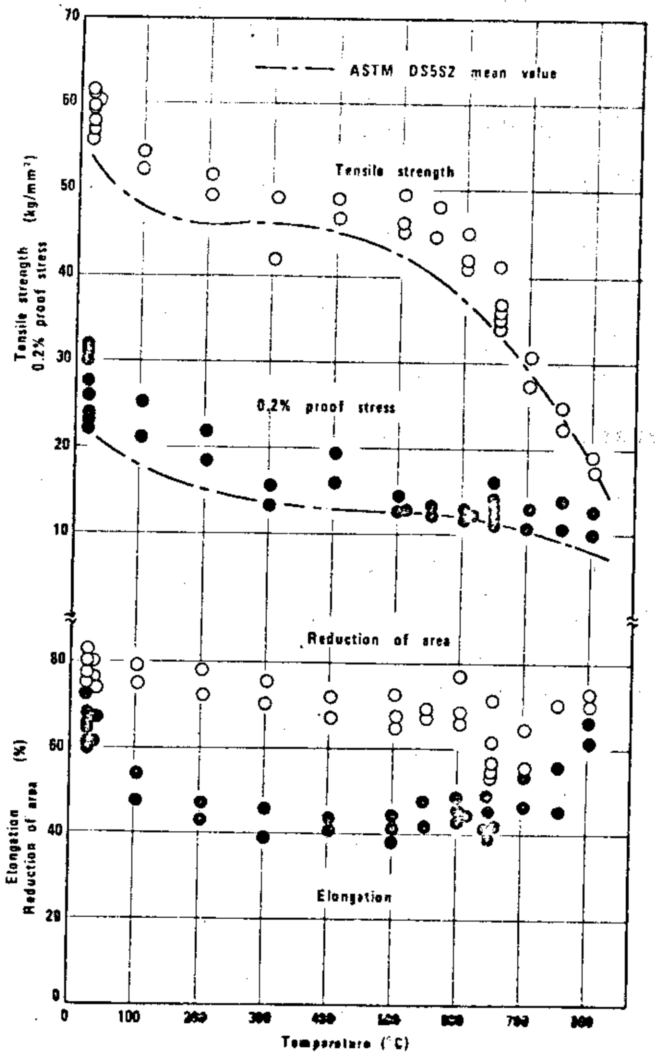

Fig. 2.A.1.1 Elevated Temperature Tensile Properties of Type 316 Steel.

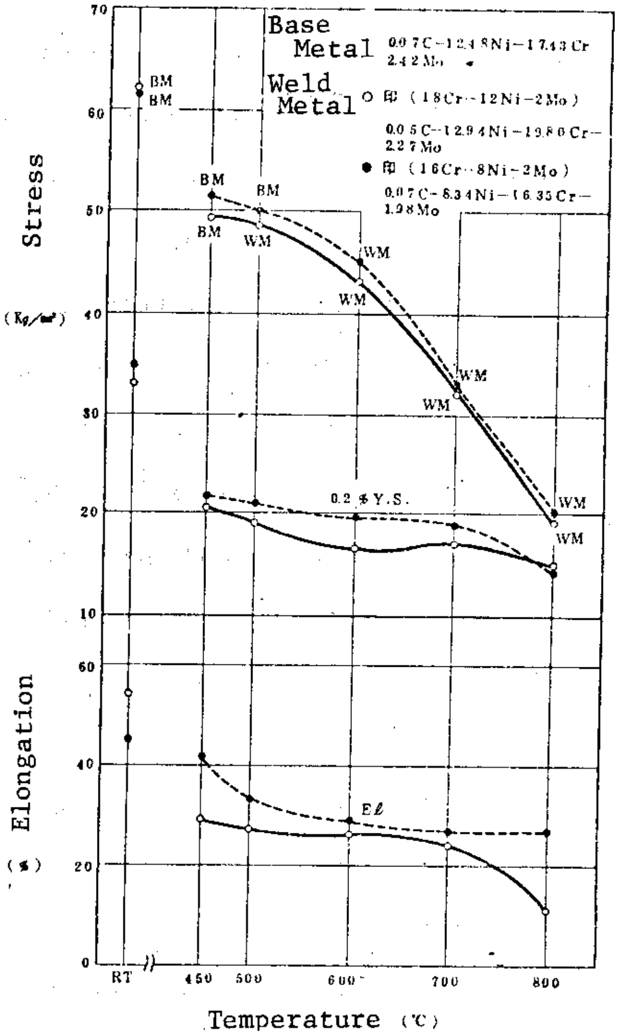

Fig. 2.A.1.2 Elevated Temperature Tensile Properties of Welded Joint in Type 316 Steel.

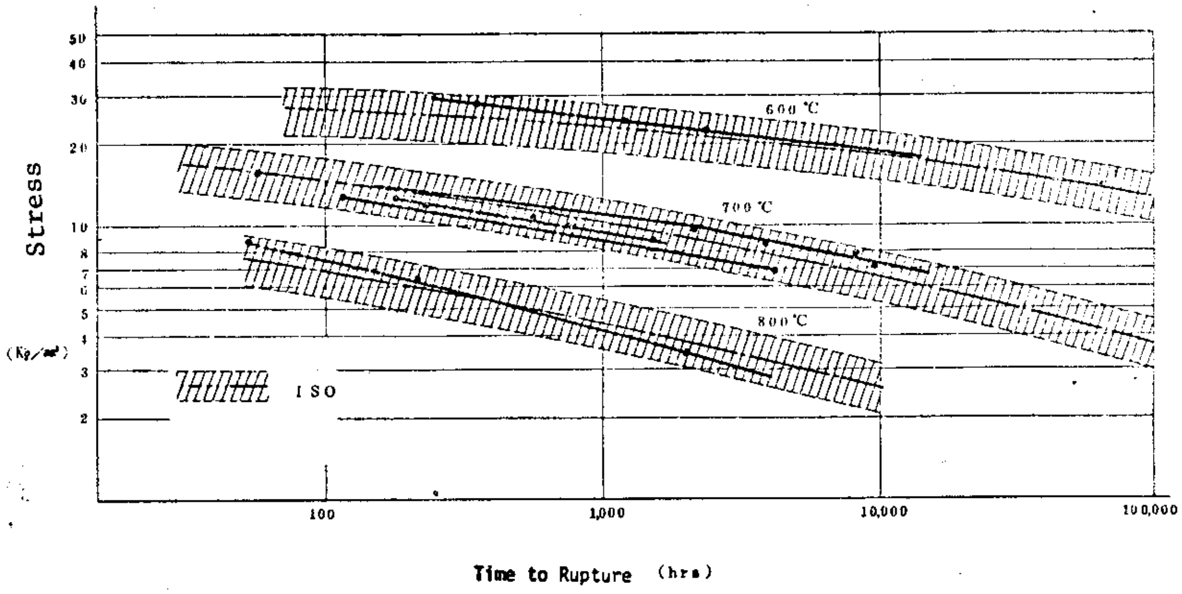

Fig. 2. A.1.3 Creep-Rupture Properties of Type 316 Steel.

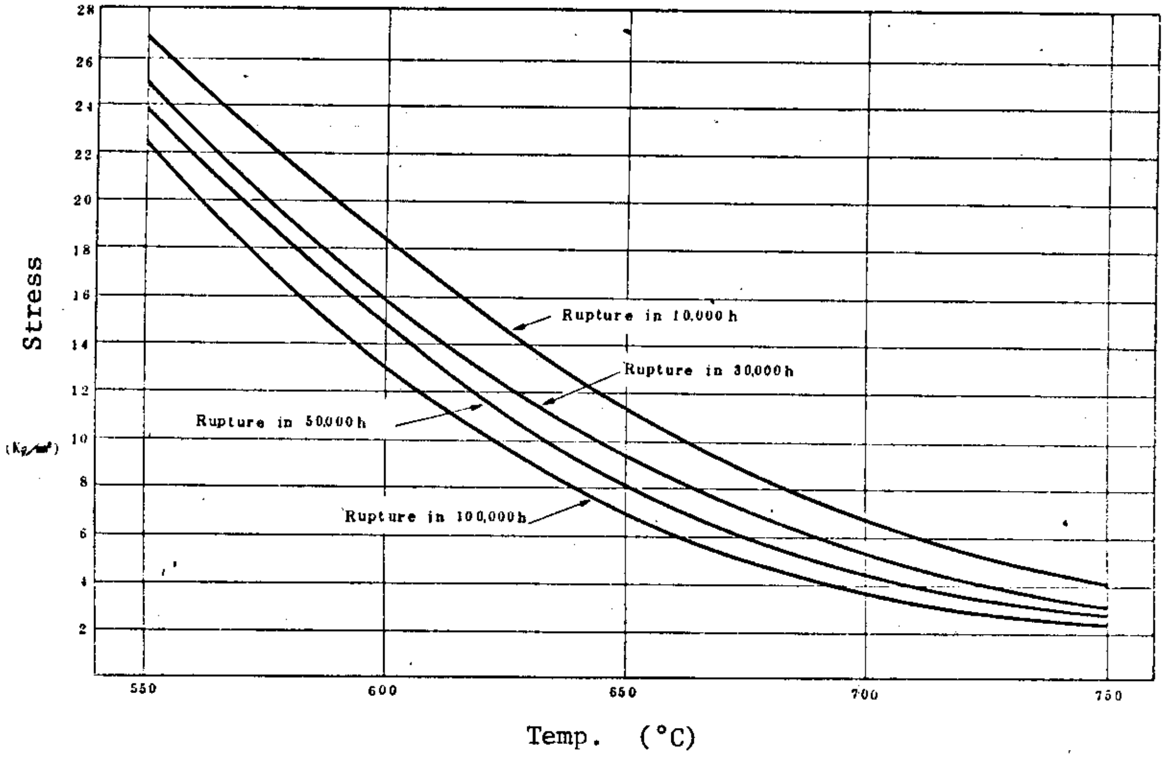

Fig. 2. A.1.4 Estimation of Creep-Rupture Strength of Type 316 Steel.

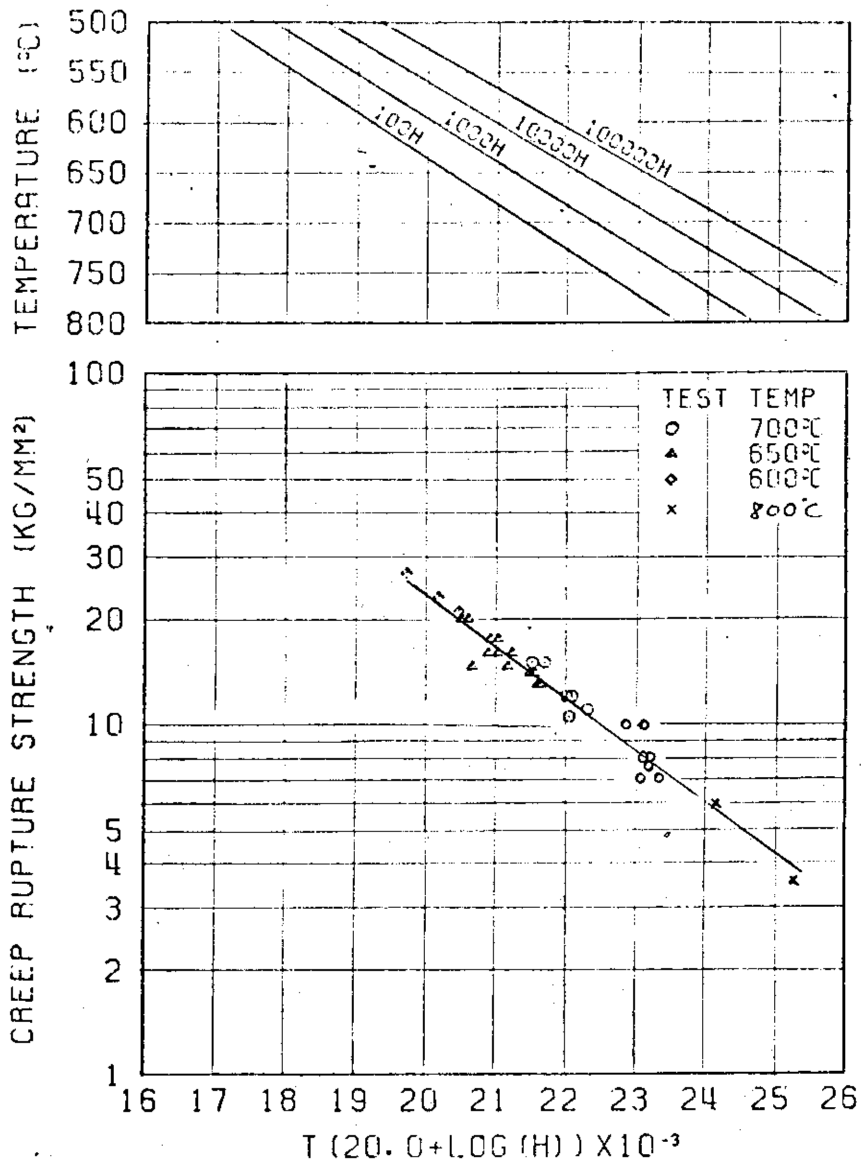

Fig. 2.A.1.5 Relation between Creep-Rupture Strength and Larson Miller Parameter of Type 316 Steel.

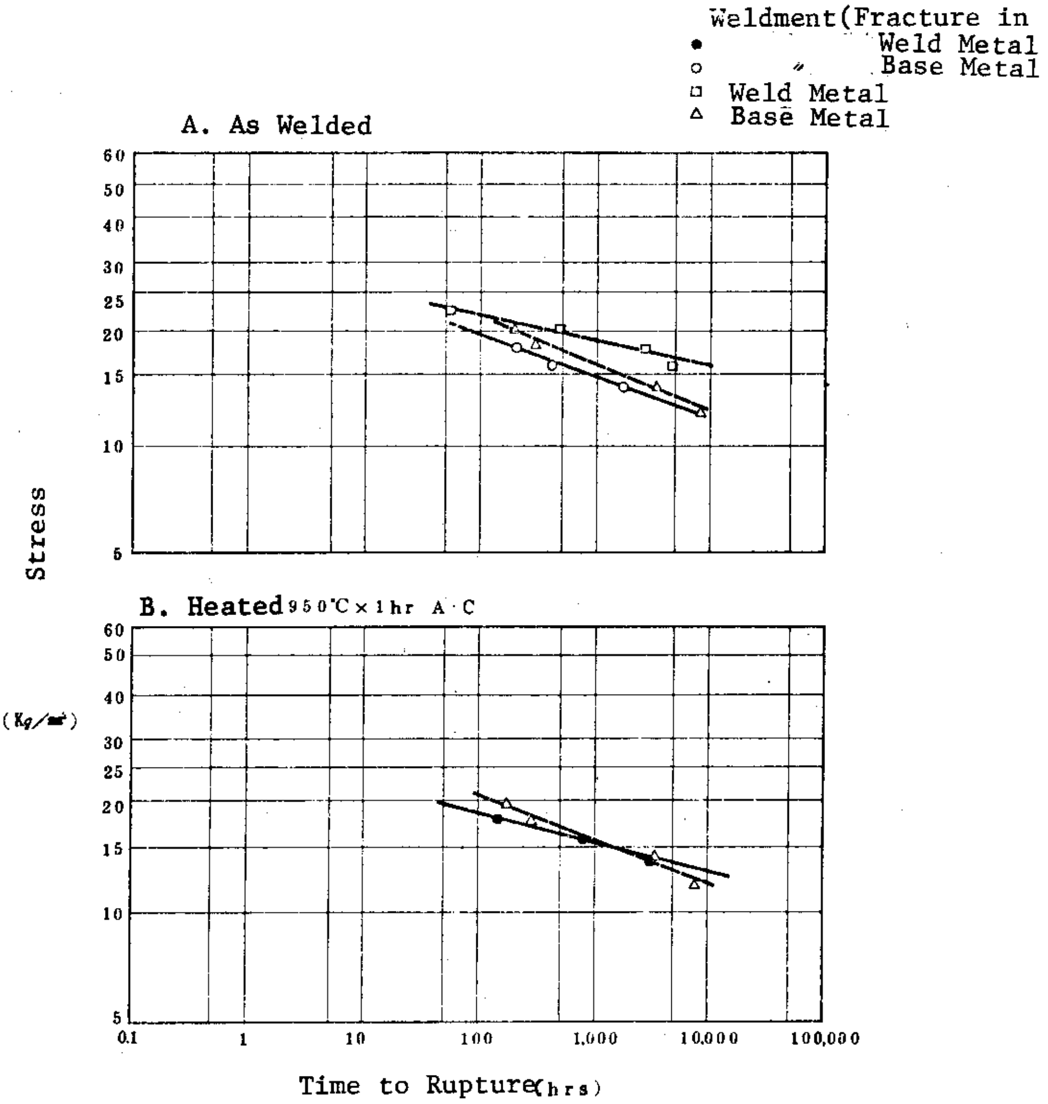

	C	Si	Mn	Ni	Cr	Mo	N.B.
Base Metal	0.07	0.49	1.50	12.48	17.43	2.42	t=16mm Hand Weld
Weld Metal	0.05	0.32	1.28	12.94	19.80	2.27	

Fig. 2.A.1.6 Creep-Rupture Strength at 650°C in Welded Joint of Type 316 Steel.

	C	Si	Mn	P	S	Ni	Cr	Mo
○	0.075	0.24	1.62	0.023	0.014	14.35	18.51	2.03
●	0.028	0.53	1.62	0.008	0.020	14.77	16.65	2.67
×	0.048	0.51	1.55	0.014	0.015	12.60	17.07	2.57

3,000 cpm

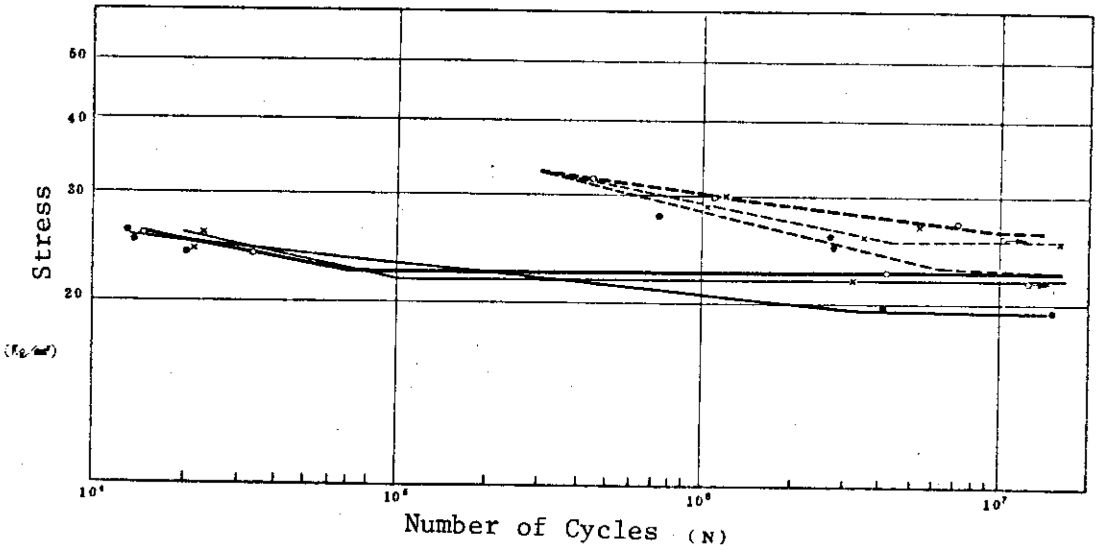

Fig. 2.A.1.7 Fatigue Curves at Room Temperature for Type 316 Steel.

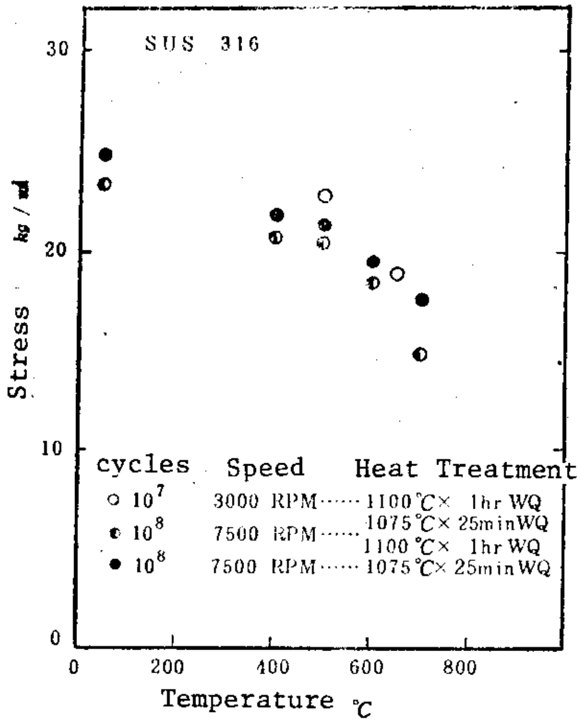

Fig. 2.A.1.8 Fatigue Limit of Type 316 Steel.

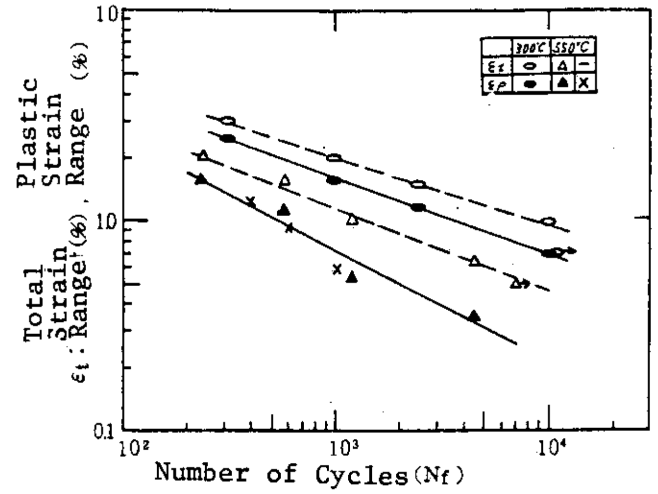

Fig. 2.A.1.9 Fatigue Curves for Type 316 Steel.

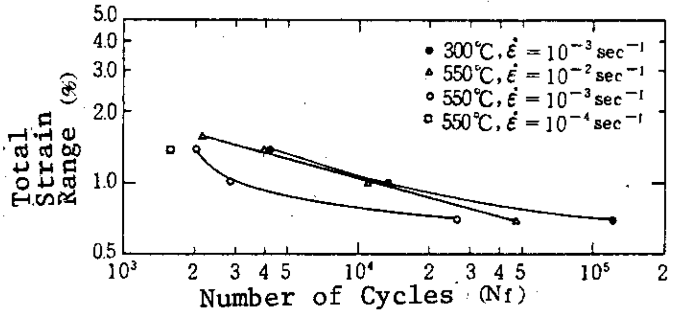

Fig. 2.A.1.10 Fatigue Curves in Vacuum for Type 316 Steel.

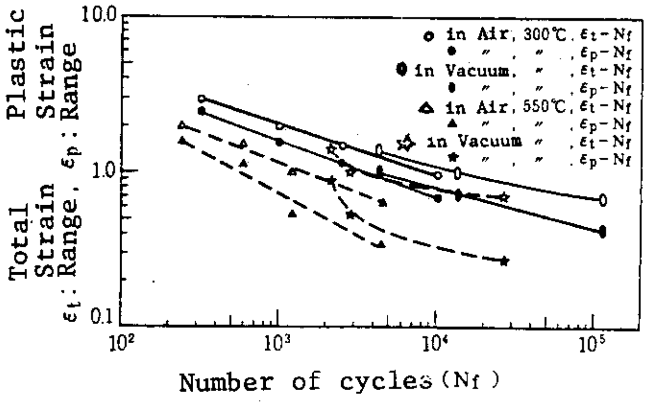

Fig. 2.A.1.11 Effects of Atmosphere and Temperature on Fatigue Curves of Type 316 Steel.

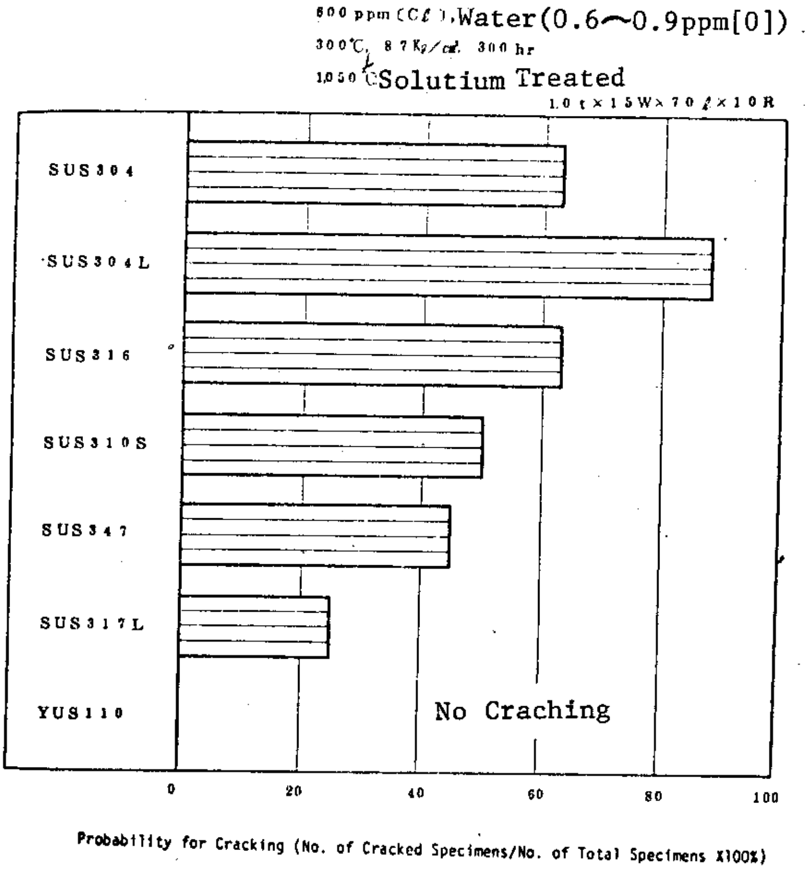

Fig. 2.A.1.12 Stress Corrosion Cracking in High Temperature and High Pressure Water for Austenitic Stainless Steel.

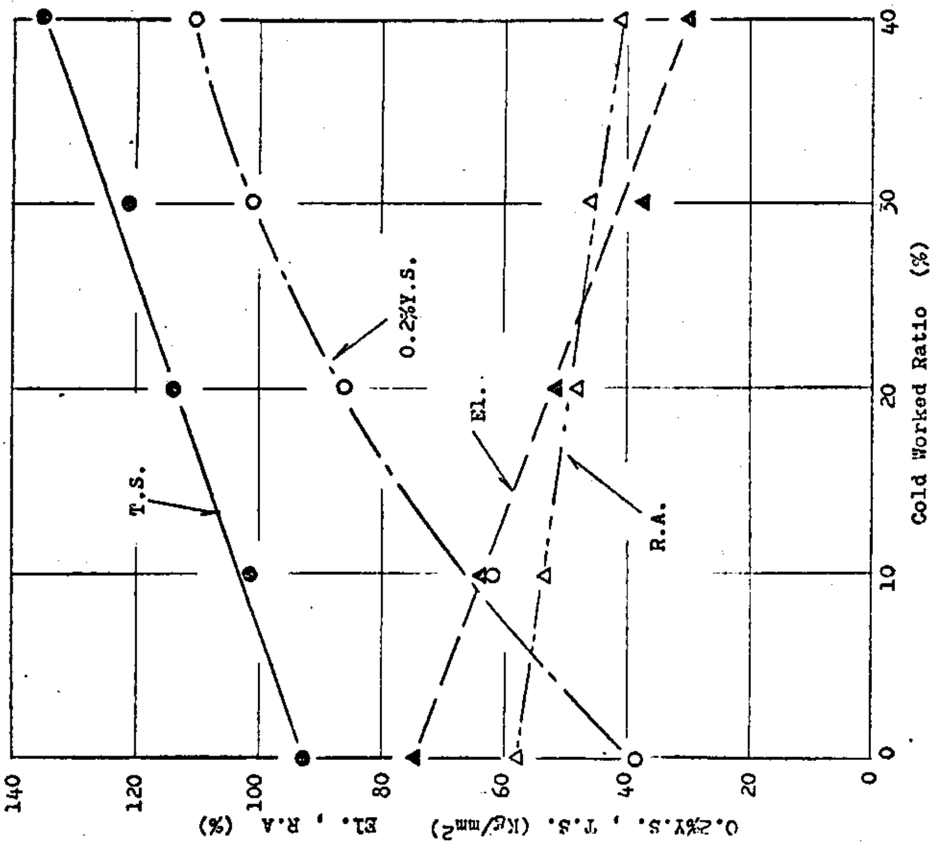

Fig. 2.A.2.1 Effect of Cold Working on Tensile Properties at Room Temperature in 18Mn-5Cr Steel.

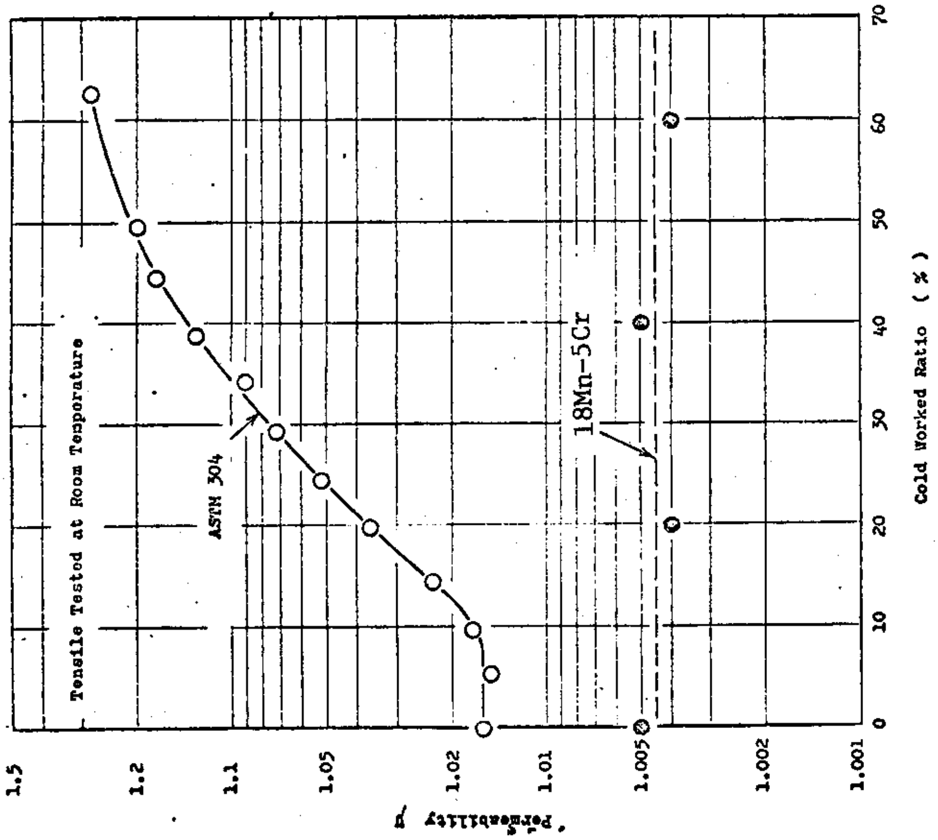

Fig. 2.A.2.2 Change in Permeability with Cold Working in Type 304 and 18Mn-5Cr Steel.

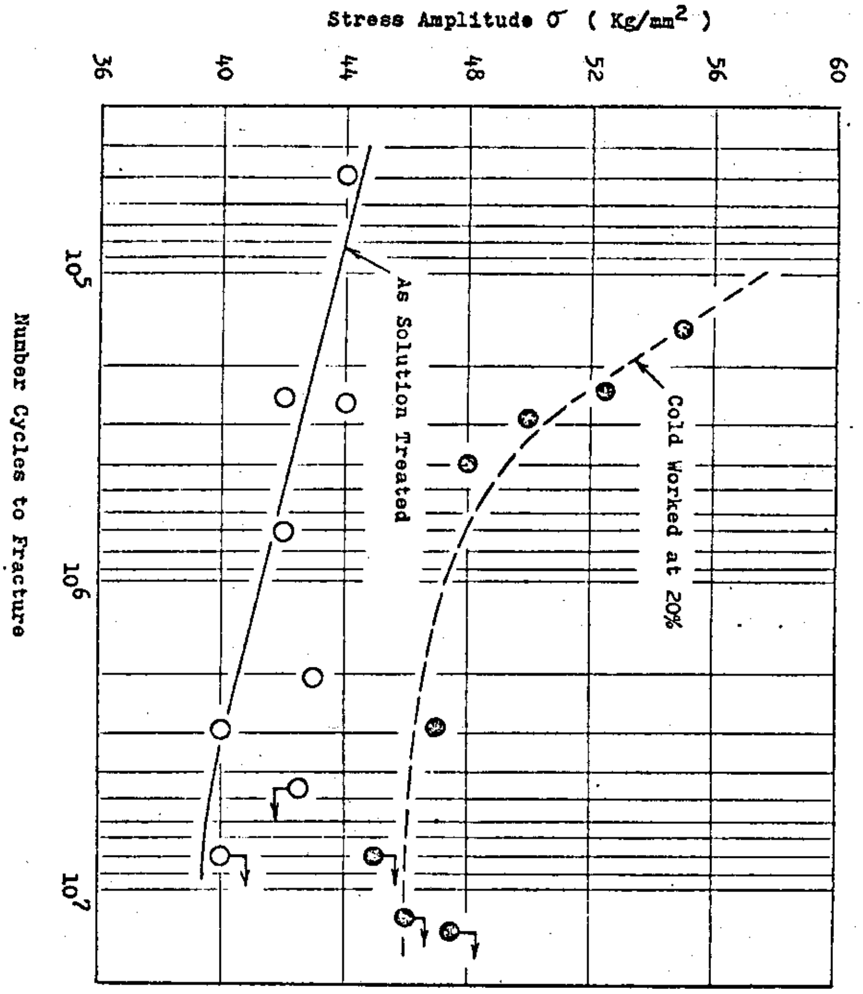

Fig. 2.A.2.3 Fatigue Curves at Room Temperature for 18Mn-5Cr Steel.

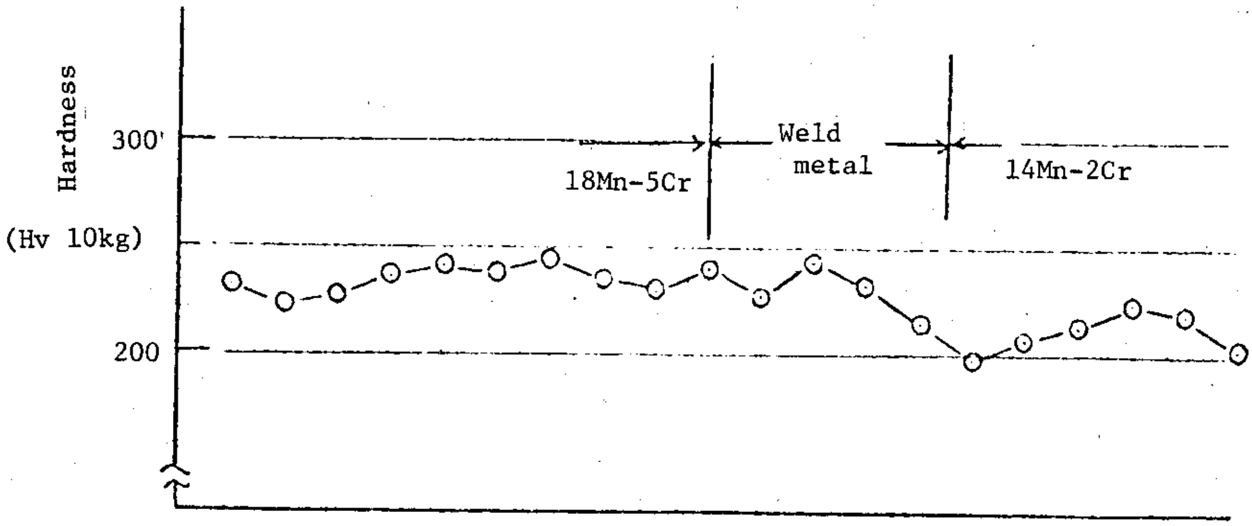

Fig. 2.A.2.6 Hardness in Welded Joint of 18Mn-5Cr and 14Mn-2Cr Steels.

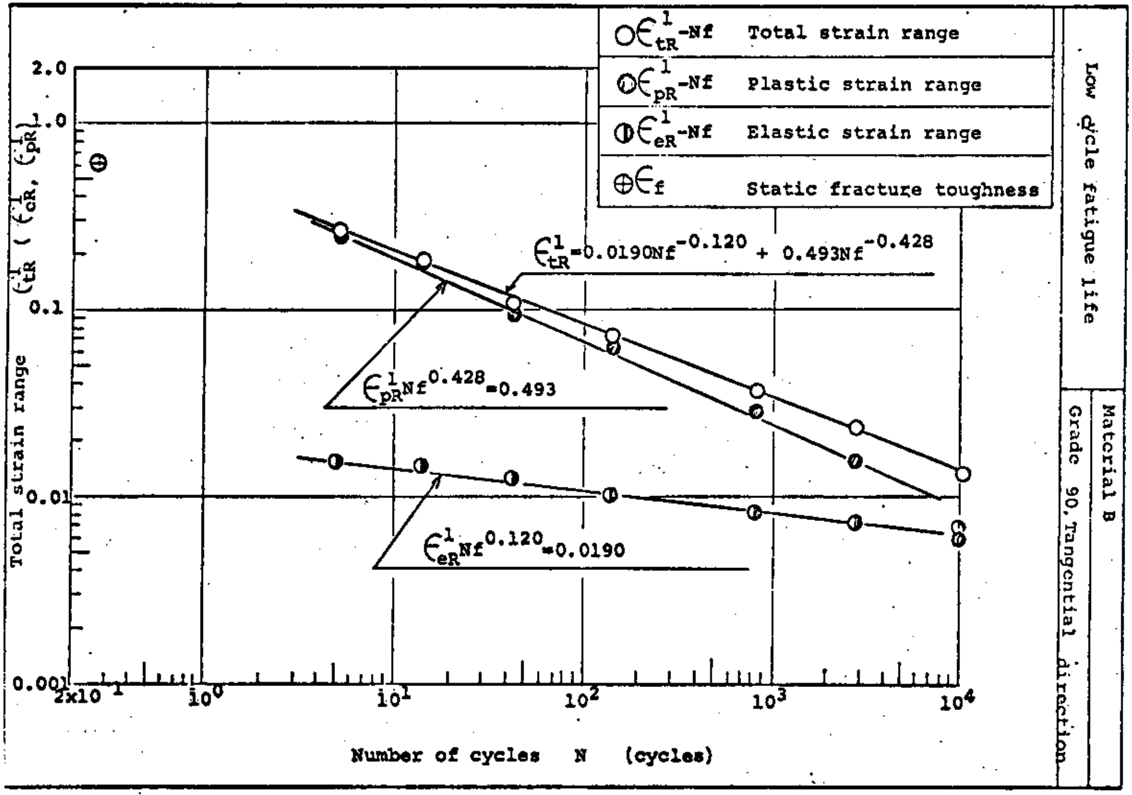

Fig. 2, A.2.4 Fatigue Curves at Room Temperature for 18Mn-5Cr Steel.

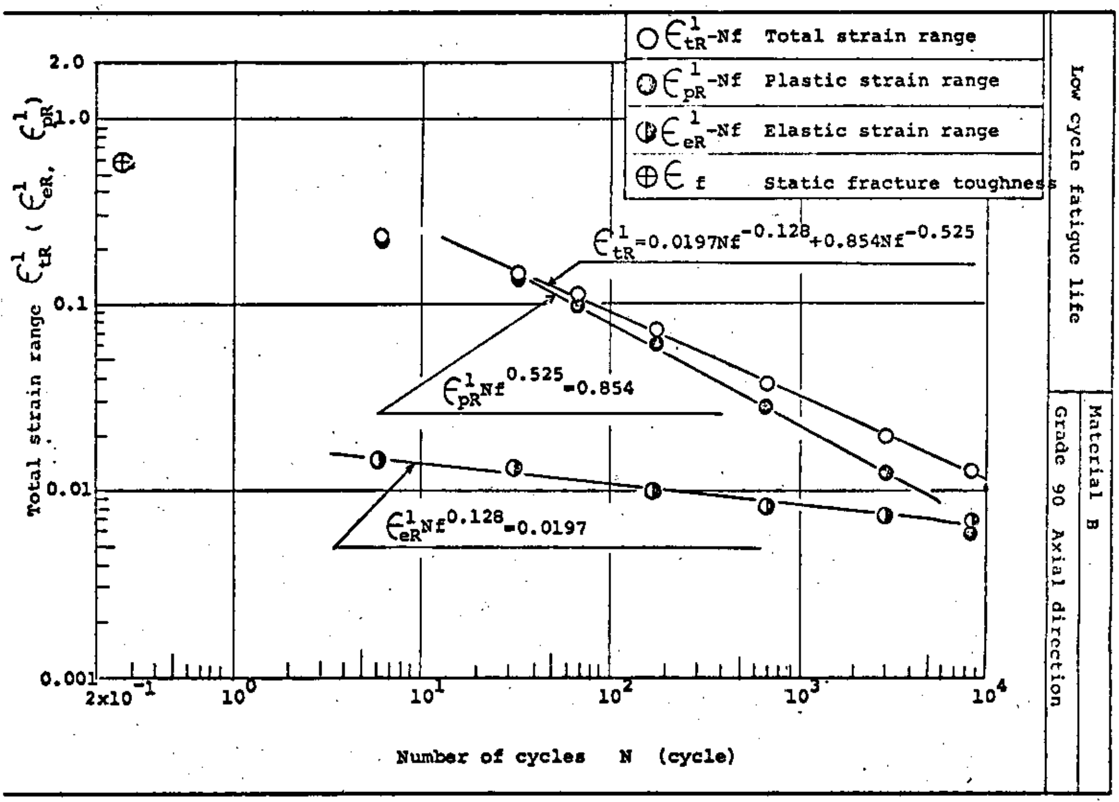

Fig. 2.A.2.5 Fatigue Curves at Room Temperature for 18Mn-5Cr Steel.

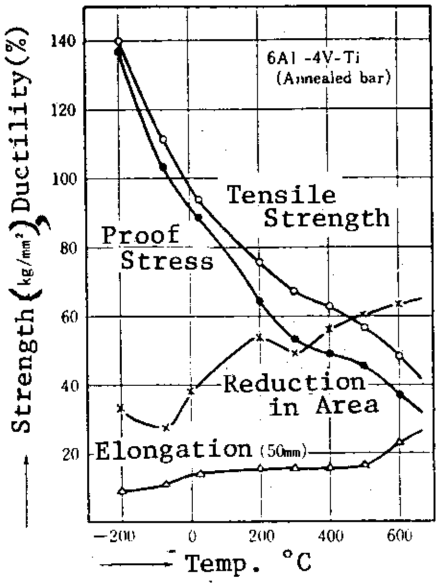

Fig. 2.A.3.1 Tensile Properties of Ti-6Al-4V Alloy.

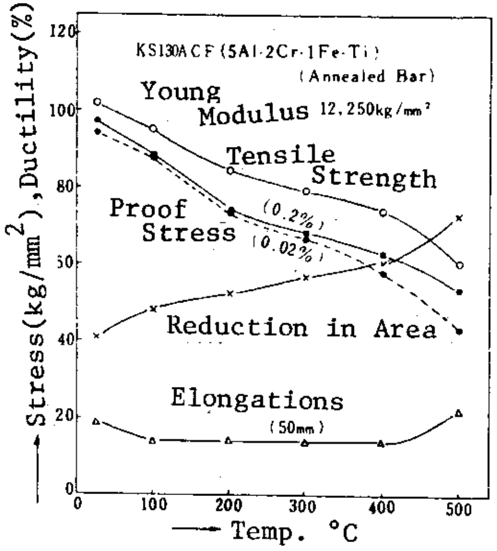

Fig. 2.A.3.2 Tensile Properties of KS130ACF (Ti-5Al-2Cr-1Fe Alloy).

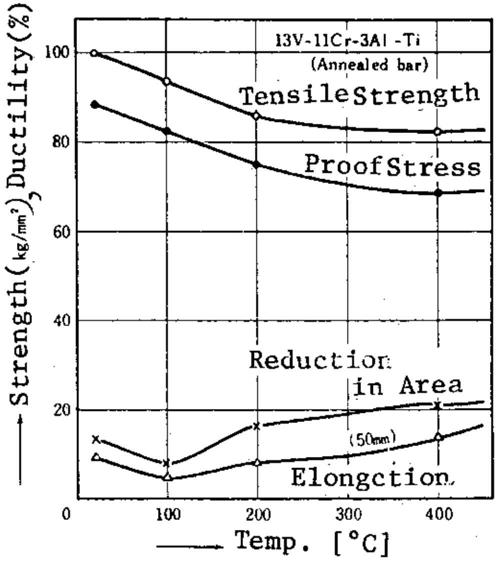

Fig. 2.A.3.3 Tensile Properties of Ti-13V-11Cr-3Al Alloy.

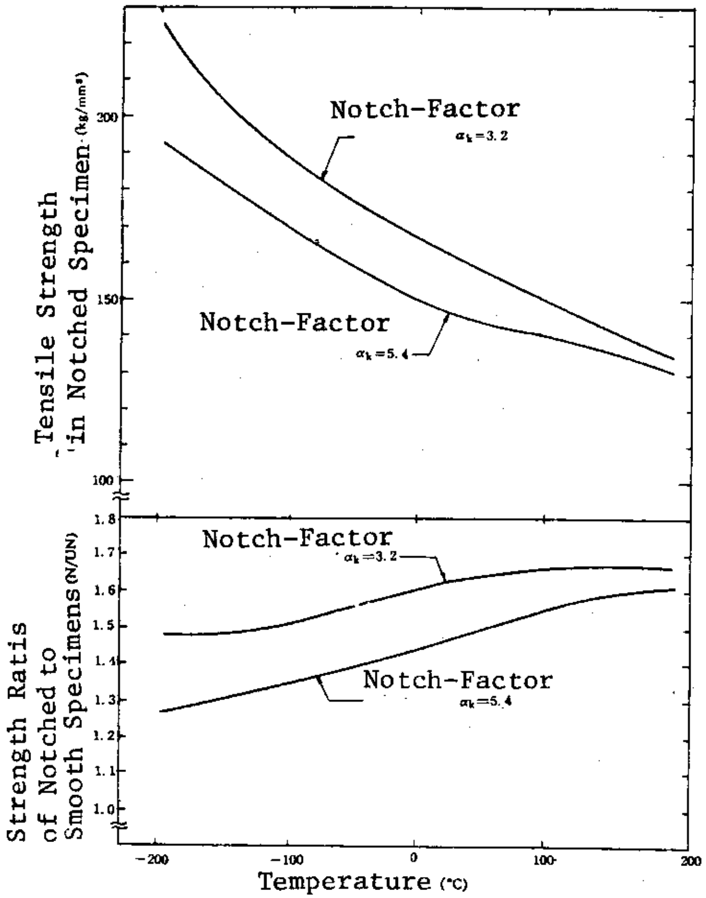

Fig. 2.A.3.4 Tensile Properties for Notched Specimen of Ti-6Al-4V Alloy (700°C × 2hr AC).

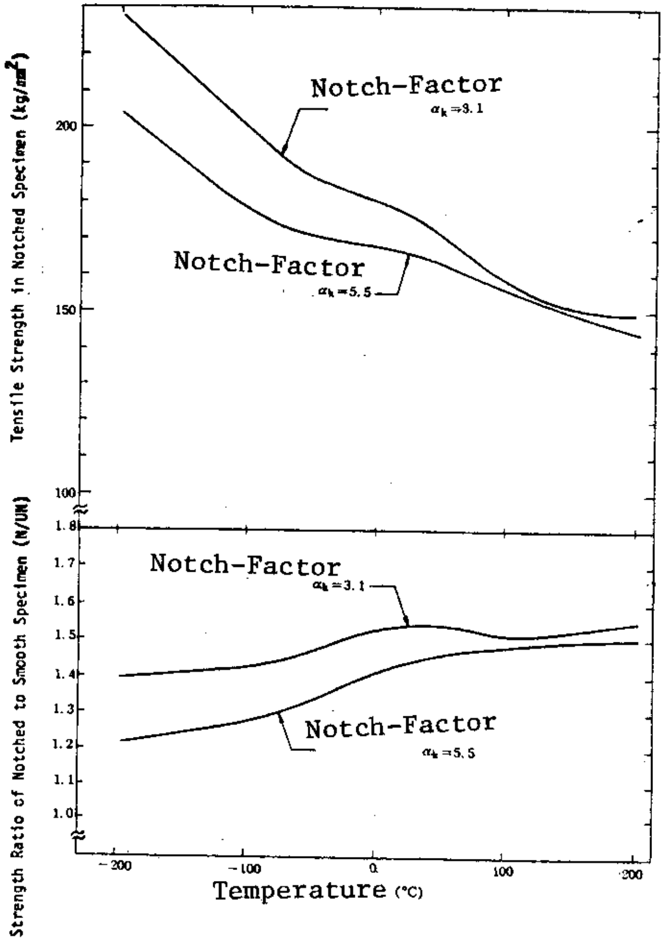

Fig. 2.A.3.5 Tensile Properties for Notched Specimen of Ti-6Al-4V Alloy (925°C × 1hr WQ + 500°C × 4hr AC).

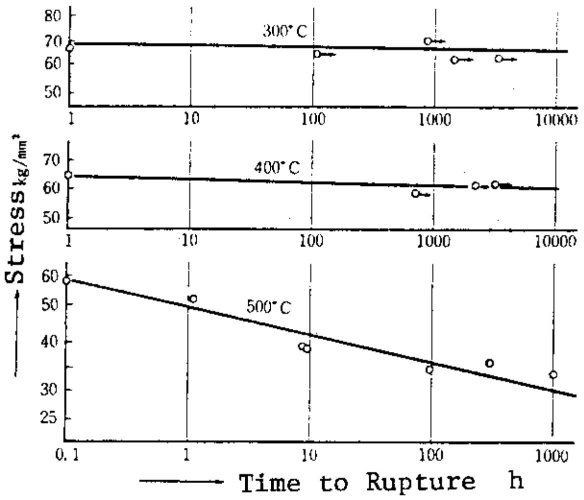

Fig. 2.A.3.6 Creep-Rupture Strength of T-6Al-4V Alloy.

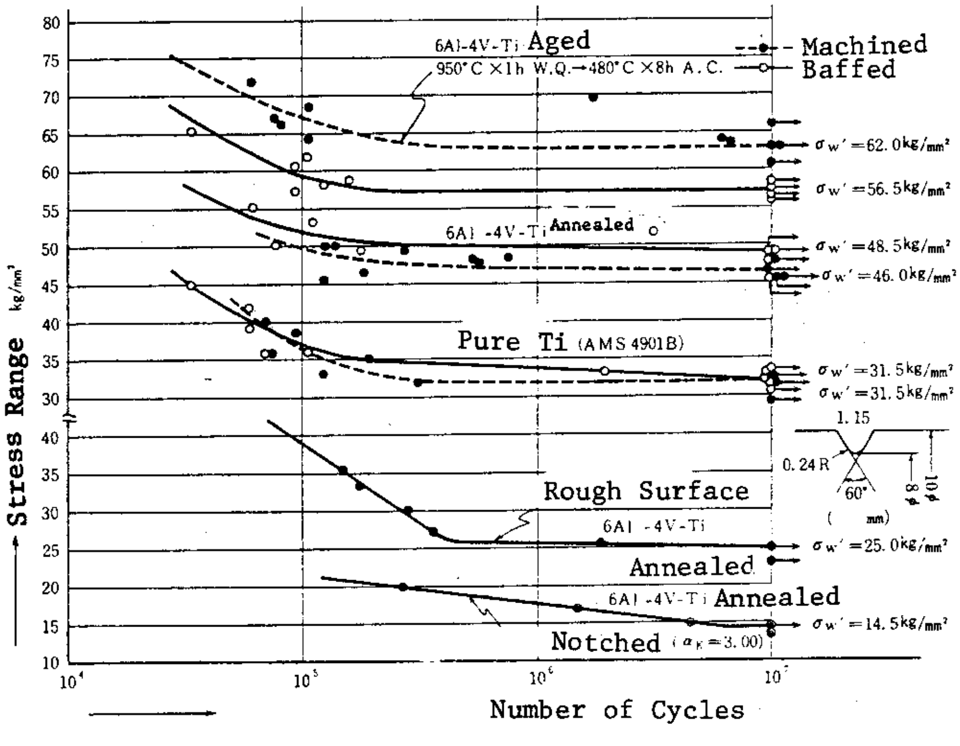

	Aged	Annealed
σ_u kg/mm²	113.8	95.3
σ_y kg/mm²	104.0	90.8
ε %	16	15
δ %	40	37
E_v kg-m/cm²	4.8	6.3
H_v	357	306

Fig. 2.A.3.7 Fatigue Properties at Room Temperature for Ti-6Al-4V Alloy.

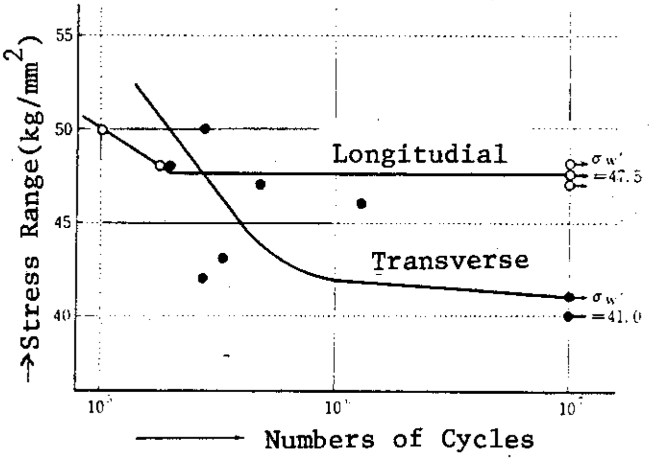

Fig. 2.A.3.8 Effect of Specimen Direction on Fatigue Strength of Ti-6Al-4V Alloy.

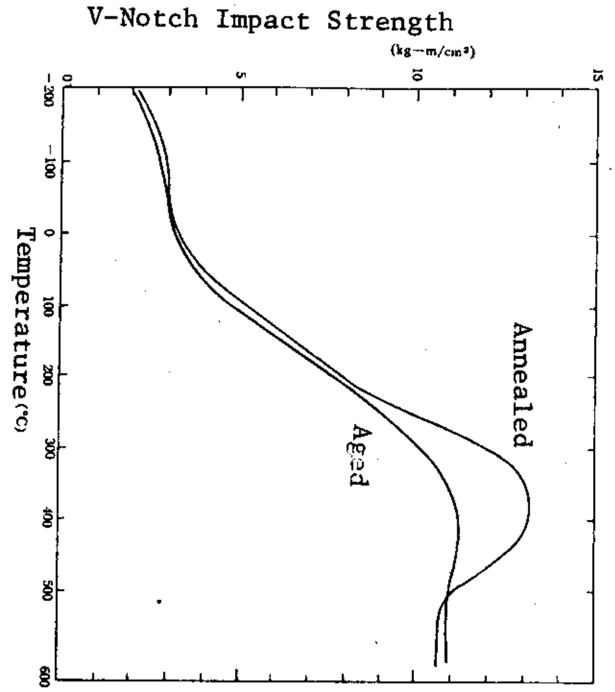

Fig. 2.A.3.9 V-Notched Charpy Impact Test for Ti-6Al-4V Alloy.

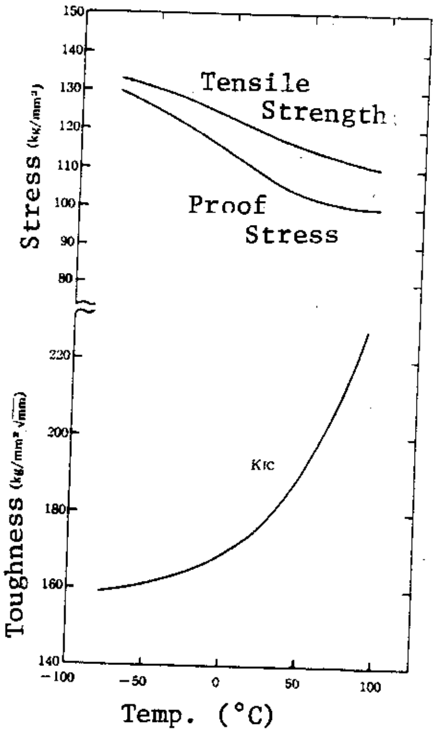

Fig. 2.A.3.10 Tensile Strength and Fracture Toughness of Ti-6Al-4V Alloy.

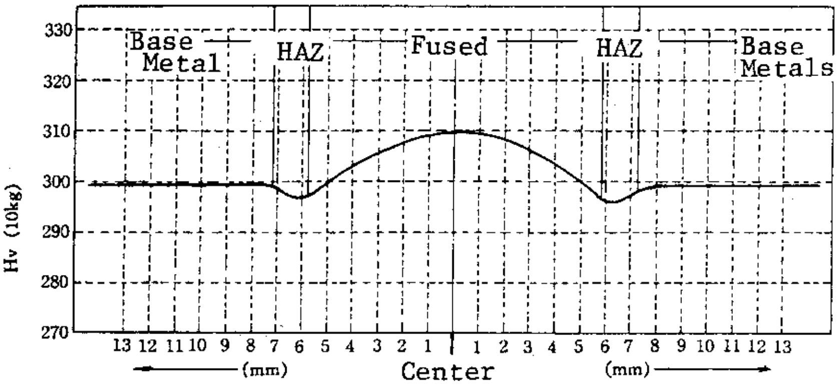

Fig. 2.A.3.11 Hardness in Welded Joint of Ti-6Al-4V Alloy.

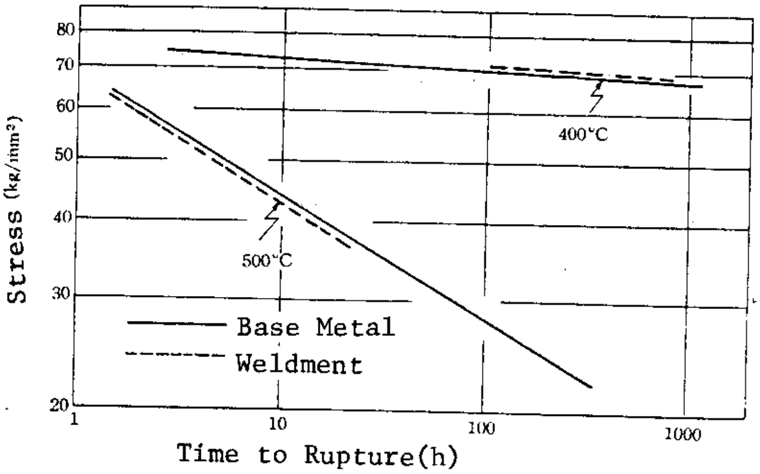

Fig. 2.A.3.12 Creep-Rupture Strength in Welded Joint of Ti-6Al-4V Alloy.

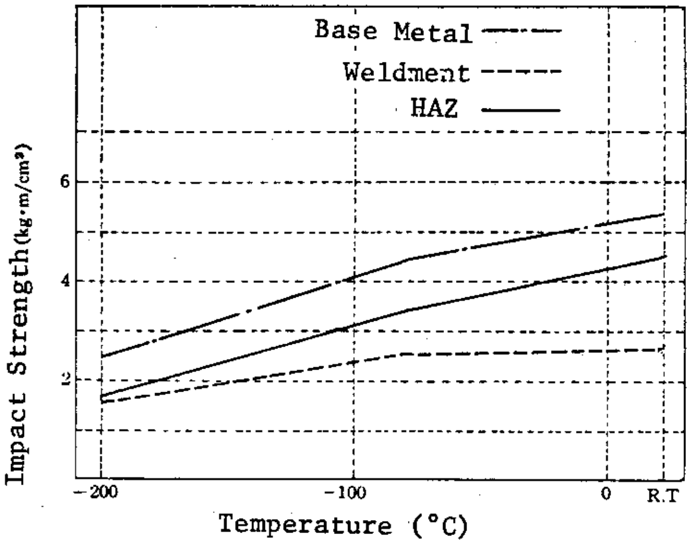

Fig. 2.A.3.13 Impact Strength in Welded Joint of Ti-6Al-4V Alloy.

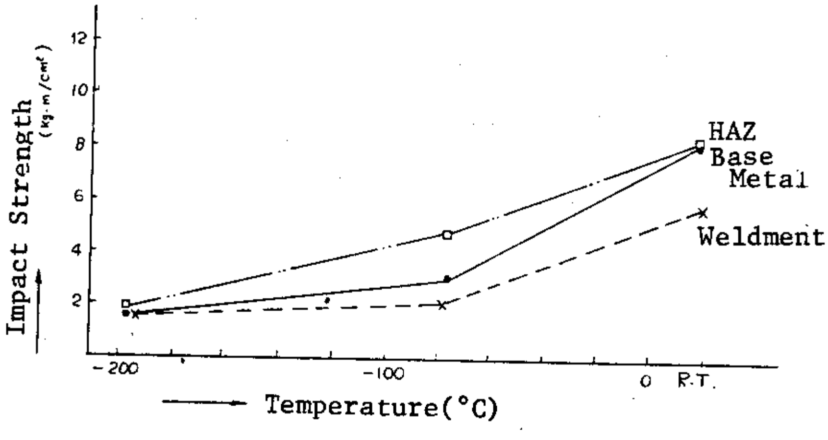

Fig. 2.A.3.14 Impact Strength in Welded Joint ot Ti-5Al-2Cr-1Fe Alloy.

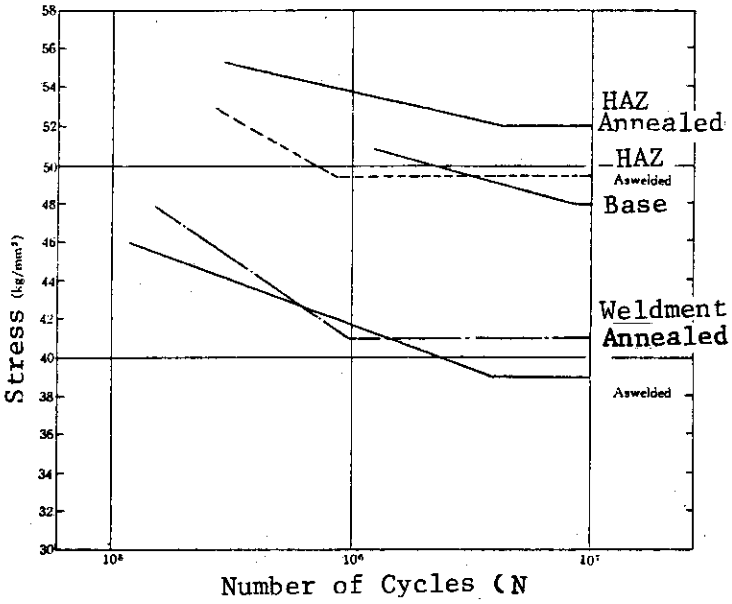

Fig. 2.A.3.15 Fatigue Properties in Welded Joint of Ti-6Al-4V Alloy.

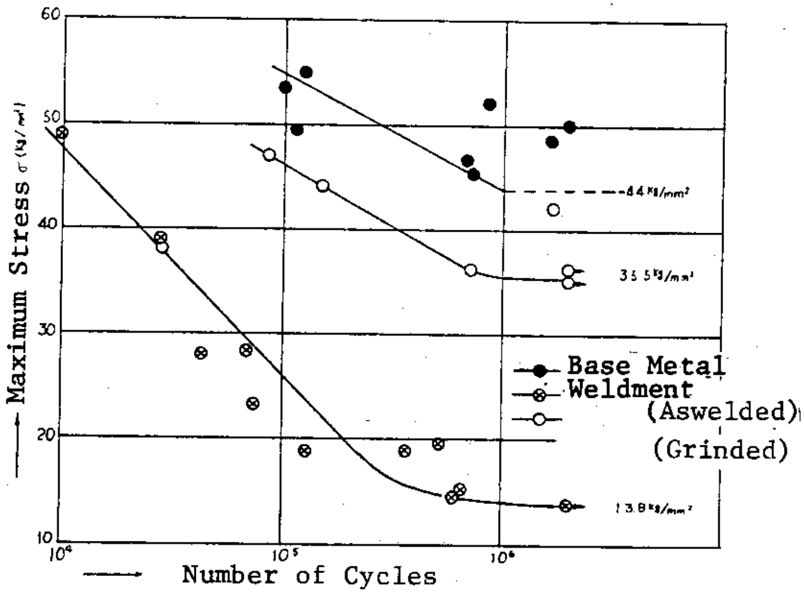

Fig. 2.A.3.16 Fatigue Properties in Welded Joint of Ti-5Al-2Cr-1Fe Alloy.

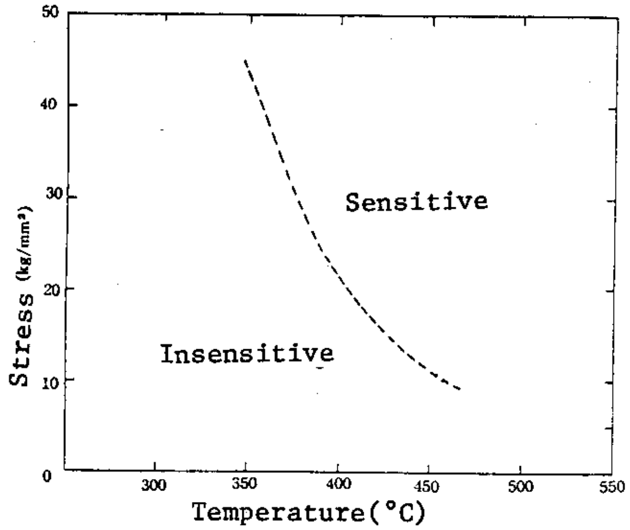

Fig. 2.A.3.17 Stress Corrosion Sensivitity for Ti-6Al-4V Alloy in High Temperature Chloride.

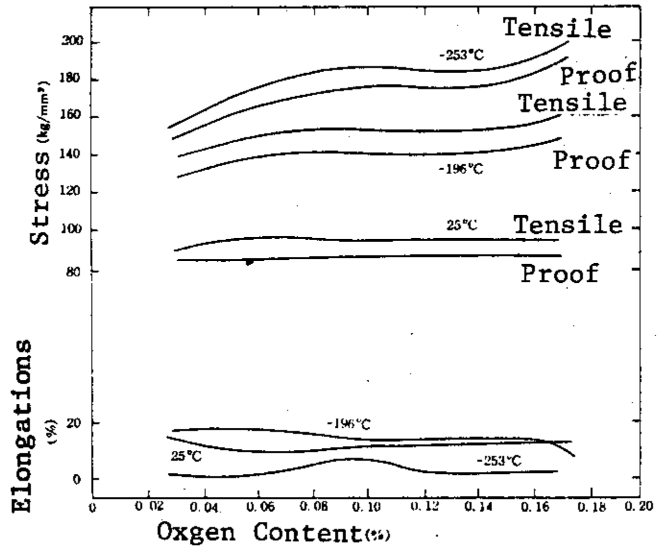

Fig. 2.A.3.18 Effect of Oxygen Content on Tensile Properties of Ti-6Al-4V Alloy.

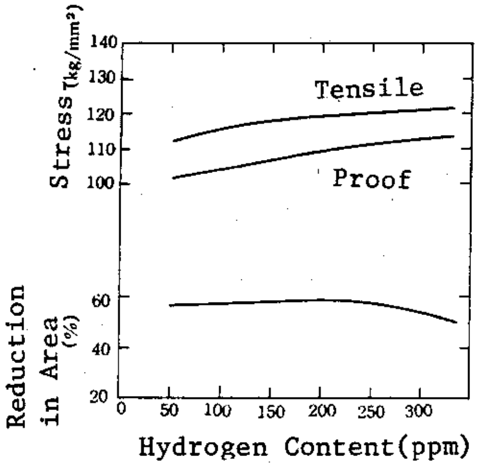

Fig. 2.A.3.19 Effect of Hydrogen Content on Tensile Properties of Ti-6Al-4V Alloy.

3. DATA BASE FOR COOLANT CHOICE

A. Compatibility of Coolant and Structural Metals

1. Introduction

When a new system without much experience is to be designed, the environment where the component materials are used may be exotic in many respects. Thus mere fact that there exists a large amount of data base on the similar but essentially different conditions does not mean that certain material or coolant is at the nearest point to the goal on that basis. Apart from the total appreciation of which material has higher potentiality as a heat carrier, the following discussion may be focused on how a combination of the coolant and metal can be free from troublesome maintainance exercises and/or free from the fear of "unexpected failure" during long time service.

2. General View

(i) Water(steam) cooling

Water or steam is one of the most familiar heat transport media for conventional industrial systems. The uses of this coolant with steels up to temperatures around 550°C are quite common in the fossile power plants. As an extreme case, some steam reforming plants are operated at temperatures of almost 1000°C with the use of heat resistant alloys. In any case, however, the expected lives of the component metals are rather short, and in this sense, the reliability expected in nuclear or its equivalent facility may not be fulfilled being based strictly on the empirical background of such technical fields.

According to the present state conceptual design condition of the INTOR system, about 400°C is the nominated temperature at the metal wall in contact with the coolant. This temperature is about 100°C above the level that is achieved by the light water reactor system, where stainless steels or the nickel based alloys like Inconel alloy 600 are used as the essential pressure boundary materials that have surfaces in direct contact with the water or steam.

In view of the coolants potential in degrading the structural metals in terms of the achievable maximum temperature and pressure, the experience in LWR system gives us an important measure that only approximately 10 years were the conservative longest service time that man has actually established for the water/metal system in the practical nuclear technology; eg. the primary side of the Inconel steam generator tubings in PWR at the moment. The metal/water compatibility in the BWR system represented by the combination of type 304 stainless steel and 288°C pure water without corrosion inhibitor can be insured much less than the above to the moment although the situation is being rapidly improved.

In any case, as long as water is used, there will be, at least, a need for great maintenance exercise and technical know-hows to establish a new systems free from the fear of material failure in the present day technical status.

(ii) Inert gas(helium) cooling

Although helium is not widely employed as coolant in the present day technology, its high potentiality has been demonstrated already in the HTR system; this material is satisfactory in the use as coolant for fission reactors.

In view of the chemical compatibility with metals, helium is probably only one substance that can be used reliably at temperatures above 700°C in the highly safety-risked system like nuclear power station or any of the equivalents.

The essential problem remaining with helium cooling, in the material compatibility aspect, is the control of impurity levels that are intrinsic to the given circulating system. The problem, however, becomes a matter of concern only at temperatures above approximately 700°C, and it may be serious as temperature goes above 800°C for most austenitic steels. The data base for the helium/metal system is being enriched because of its importance in most advanced nuclear systems, particularly for the process heat HTR's to the moment.

3. Specific discussion and recommendation

For the austenitic materials like AISI 300 series stainless steels and iron- and nickel-base heat resistant alloys, typically like Incoloy 800 and Hastelloy X respectively, the probable failure modes during the uses as structural components may be limited in only a few categories if service temperature is below 500°C. This is because of the facts that creep component in the deformation is neglesible, and that the rate of general metal-environment reaction, ie, uniform attack, is low enough except in case of some very localized kinds of reactions.

Provided that the metal retains sufficient ductility during the life time, possible failures may be limited in

(1) fatigue or corrosion fatigue under cyclic load,

(2) stress corrosion cracking under sustained load,

and

(3) localized attack including pitting and intergranular corrosion.

The problem of failure under superposed effects of irradiation and the chemical environment is an unexplored area if exists any, and it should be discussed in a different phase of occasion in future.

(i) Water(steam) cooling and data base

At 400°C water always takes the form of steam as it is above the critical point. At this temperature level water itself is basically an active reactant to interact with major elements contained in the alloys either directly or through hydrogen formation.

Fatigue can occur when the operation is of cyclic nature. The existence of the active chemical environments such as steam can considerably accelerate the initiation and growth of crack under fatigue conditions. For design purpose, it may become necessary to establish a guide to take into account the environmental factor that may lower the threshold stresses for the cyclic crack development conditions hence influencing the allowable design stresses.

The knowledge on the susceptibility of the common austenitic materials to the stress corrosion cracking and the intergranular corrosion in high temperature aqueous environments is now fairly well established, while much uncertainty remains in the steam case.

More uncertainty may remain for the application of such knowledge to the INTOR case where the expected operation temperature is higher by about 100°C than in LWR.

As it has recently been demonstrated through experiments, the austenitic materials that were mentioned above can be sufficiently sensitized by the so called low temperature sensitization mechanism, ie. the cumulative thermal effects to cause the effect equivalent to the high temperature short time exposure through long time exposure at lower temperatures. This happens at the weld-heat-affected-zone of the piping of BWR, where the operating temperature is only at 288°C, but the time of exposure is of the order of 10^4~10^5 hrs. For 400°C the equvalent time could be shortened to some 10^3~10^4 hrs.

There, of cause, can be many evidences that these material had survived in 400°C steam for many years in the conventional system. It may also be of great help to consider the use of some appropriate additives as corrosion-inhibitor for improving water chemistry if any additive is allowable. It is still doubtful, however, if we could easily reach to a status of having a straight forward solution to a well defined design condition without making a considerable reliability confirmation tests. Now most authorities may agree how the confirmation of "never" having the probability of the failure, like stress corrosion cracking, costs money, time and arguements in the high temperature aqueous systems.

The data base for the failure and the protective means is abundant in this metal/environment system.

(ii) Helium cooling and data base

The fact that helium itself is a perfect inert substance can provide both advantage and disadvantage. As far as the purification system has a sufficient capacity to a given circulating system, most material compatibility problems disappear. The fact of having low operating temperature, ie, below approximately 500°C may facilitate the above statement more firmly, and even gives large margin to the allowable impurity level if any problem exists in this respect.

The limited disadvantages of the use of helium are (A) metal surface may maintain "tribological" activity so that the contacting surfaces tend to stick or selfweld to each other thus causing difficulty at any sliding surfaces by increased galling or friction, and (B) there is a slight probability of increased corrosion in extremely dry and pure helium. The latter aspect comes from some very limited but substantial evidences that have been obtained in the HTR and GCFR material studies. The cause of such unexpected phenomenon is that the presently common austenitic alloys are designed to protect themselves by spontaneous oxide film formation upon contact with some "appreciably oxidizing" environments. If temperature is high and the oxidizing potential is lowered, the materials happen to lose their protection by failing to form continuous protective films. This problem again may not be too serious for the system to be operated below 500°C.

The optimism can get a substantial support from the data bases accumulated in the experience of steam cycle HTR. Further support can be obtained by more critical test results for process heat HTR's and the helium cooled GCFR's for which all tests have been made at above 600°C.

In the helium cooling system the only concern, to the moment, may be the levels of possible impurities in helium stream. The expected impurities for most HTR system come from the graphite core which is a very massive body with tremendous amount of effective reaction surfaces. Even in such system the total impurity levels are reported to be below 1 μatm.

The kinetics of oxidation is known to follow a rather well defined time dependence, either $W^2 = kt + C$ or $W^3 = kt + C$, where W, k, t and C are the integrated amount of oxidation reaction, rate constant, time and a constant.

The temperature dependence of this reaction rate is known in the form of a typical Arrhenius relation; ie,

$$k = A \exp(-Q/RT)$$

where Q takes approximate value of 50 kcal/mole. All of the extrapolation of the data for HTR (700~800°C), VHTR (800~1000°C), and GCFR (600~750°C), for stainless steels and some nickel-based alloys gave negligible values, provided that the impurity level in the INTOR helium circuit is nearly equivalent to those system. Therefore there is no essential problem in terms of corrosion attack in the helium-cooled system.

The only problem that needs to be checked critically is fatigue, if the INTOR system employs a pulse type operation mode. The effect of helium environment on fatigue is not completely clear yet. Limited experience showed that the typical HTR or GCFR environment influenced the fatigue behavior of austenitic stainless steel and several nickel-base alloys almost negligibly unless helium was heavily contaminated.

In view of the data base for the helium-metal compatibility the following general statements can be made.

In INTOR system, the possible impurity in helium may be trace of water and hydrogen or their equivalents if the circulation system is constructed only of metals. If any low Z material like graphite is involved, then, CO, CO_2, CH_4 may be found in addition to the above. For such system the related engineering data may be available in the following categories although the data base is not abundant yet;

Reactor System	Nature of Environment	Temperature	Major Compatibility Problems
Steam Cycle HTR	He+(CO,CO_2,CH_4,H_2,H_2O)	700~750°C	Oxidation Carburization Corrosion-Creep Fatigue Tribology
Process Heat VHTR	Same as above (less H_2O,CO_2, more H_2,CO)	800~1000°C	
GCFR	He+(H_2,H_2O)	600~700°C	Oxidation Corrosion-Creep Fatigue Tribology

The major parameters in assessing the problem of a particular system, the followings may be the case;

① Partial pressures and concentrations of possible impurities

② Total pressure

③ Expected life time

④ Operating temperature and its time profile, ie. cyclic or monotonic

⑤ Stress levels and loading pattern

Most data base are focused on

① Austenitic stainless steels (especially type 316 and 304)

② Incoloy 800
and
③ Hastelloy X

including their modified versions in all these three cases.

(iii) Recommendation

From compatibility point of view the use of helium as the coolant is most suitable. The advantage of choosing this substance among many reasons is the greatest margin for the material-system integrity so that is allows the designer to switch the selection from one material to the other without any deep concern about the side effects associated with the sudden switching. For example, nickel base super alloys are known to be much resistant to the irradiation induced swelling. Free switching from stainless steel to such alloys may induce a great concern for new compatibility research duty in case of either sodium or steam cooling, while almost no such care may be required in case of helium cooling even at considerably later stage of the program.

4. DATA BASE FOR BREEDER CHOICE

Solid state blanket breeding materials have certain advantages concerning reactor structure, safety, maintenance, and tritium inventory in addition to lithium resources problems, in comparison with liquid metal or fused salts in a fusion reactor, and lithium oxide (Li_2O) pellets had been selected as a solid state blanket breeding material in the JXFR because its high lithium density (8.2×10^{22} atoms cm^{-3}) and high melting temperature (1,420°C) as shown in Table 4.A.1. At that time, any data on Li_2O compacts had not been available. In this circumstances, a series of experiments on Li_2O have been being carried out to clarify properties and irradiation behaviors of Li_2O pellets and to establish excellent and economical preparation methods of sintered Li_2O pellets.

A. Unirradiated properties

A.a.1. Study of starting materials (1)

The heat capacity and thermal decomposition of Li_2O_2 were investigated by adiabatic scanning calorimetry to establish economical preparation method of Li_2O pellets. The heat capacity equation obtained by the least squares method was given by,

$$C_p = 59.665 + 52.123 \times 10^{-3}T + 5.0848 \times 10^{5}T^{-2} \ (J/mol \cdot K)$$

as shown in Fig. 4.A.1. The smoothed heat capacities and the thermodynamic functions including entropy, enthalpy and Gibbs free energy function were obtained by the least squares method as shown in Table 4.A.2. The decomposition was observed to be endothermic above 570°K as shown in Fig. 4.A.2, and enthalpy of the thermal decomposition was determined to be 25.8 kJ/mol. Studies of the thermal decomposition are now in progress for the starting materials such as Li_2CO_3 and LiOH.

A.a.2. Preparation of sintered pellets (2)

Sintered Li_2O pellets of a wide range of density from 70 to 93% theoretical were prepared by a usual press-sintering method and sintering characteristics of Li_2O were studied with Li_2O powder as starting material, including heat treatment of the powder, compaction pressure and sintering temperature. The effect of sintering temperature in vacuum on bulk density is shown in Fig. 4.A.3 as an example of the results obtained.

Dense Li_2O pellets up to 99% theoretical were also prepared by an isostatic high pressure high temperature hot pressing method under the conditions of 1,000 to 2,000 atm. and 1,000 to 1,200°C after containment of green Li_2O pellets with nickel capsules.

A.a.3. Preparation of single crystals (3)

Large transparent single crystals (8mm in diameter and up to 100mm in length) of Li_2O were prepared by the infrared floating zone method. The crystals showed the growth facet parallel to (111) plane and perfect cleavage along (111) plane.

A.a.4. Ceramograph of the sintered pellets (4)

Effective etching solutions were found in revealing clearly microstructures such as grain boundaries and pores, and ceramographic observations of the Li_2O pellets were successfully done using optical micrographic and scanning electron micrographic techniques. Photo. 4.A.1 shows a photomicrograph of the polished and etched cross section of the dense specimen of 99% theoretical density. Equiaxed grains of hexagonal networks of about 60 μm on average and a small amount of pores are clearly visible inside the pellet. On the other hand, a large columnar grain region of about 100 μm in diameter and about 200 μm in length is visible between the equiaxed grain region and the nickel cladding directly adjacent to it.

Photo. 4.A.2(b) shows a photomicrograph of the polished and etched surface of a sintered Li_2O pellet of 93% theoretical density. Inter- and transgranular pores (average size:4.4 μm) and equiaxed grains (average size: 33 μm) are visible.

Photo. 4.A.2(a) shows a scanning electron micrograph of the fractured surface of a dense Li_2O pellet. Pores are scarcely visible. Typical fracture surfaces are intergranular; sometimes transgranular fracture surfaces are also visible.

Photo. 4.A.2(b) shows a scanning electron micrograph of the fractured surface of a sintered Li_2O pellet of 93% theoretical density. A mixture of inter- and transgranular fractures is visible, on which many inter- and transgranular pores are observed. The shape of the transgranular is almost spherical, whereas that of the intergranular is complex.

Photo. 4.A.2(c) shows a scanning electron micrograph of the polished and etched surface of a dense Li_2O pellet. Pores are scarcely visible. The microstructures observed by the scanning electron microscopy are similar to those observed in the optical photomicrograph.

Photo. 4.A.2(d) shows a scanning electron micrograph of the polished and etched surface of a sintered Li_2O pellet. Many inter- and transgranular pores are also observed more clearly than in the optical photomicrograph.

A.b.1. Vapor pressure (5)

The equilibrium vapor pressures over solid Li_2O have been measured mass-spectrometrically using platinum, molybdenum and tantalum Knudsen cells in the temperature range of 1,300-1,700°K as shown in Fig. 4.A.4.

From the gaseous equilibria obtained in plutinum Knudsen cells the heats of formation and the atomization energies of LiO(g), $Li_2O(g)$, $Li_3O(g)$ and $Li_2O_2(g)$ were determined.

A.b.2. Thermal conductivity (6) and thermal expansion (7)

Thermal diffusivity of sintered Li_2O pellets having a wide range of density (70.8 to 93.4% theoretical) was measured in the temperature range of 473-1,173°K by the laser pulse method. Porosity dependence of the thermal conductivity for Li_2O was determined by using the Maxwell-Eucken formula. Thermal expansion coefficient was also measured in the same temperature range.

A.b.3. Heat capacity (8)

The heat capacity of Li_2O was measured in the temperature range 306~1,073°K using an adiabatic scanning calorimeter, and any heat capacity anomalies such as phase transition were not observed as shown in Fig. 4.A.6. The heat capacity equation obtained by the least squares method was given by,

$$C_p = 75.24 + 9.55 \times 10^{-3}T + 25.05 \times 10^{5}T^{-2} \quad (J/mol\cdot K)$$

The smoothed heat capacities and the thermodynamic functions including entropy, enthalpy and Gibbs free energy function were obtained by the least squares method as shown in Table 4.A.3.

A.b.4. Diffusion (9)

Self diffusion coefficients of lithium ions and oxygen ions in Li_2O and their activation energies were determined in the temperature range of 800~1,500°K. Self diffusion coefficients of lithium ions were much larger than those of oxygen ions, and the intrinsic region of lithium was found to be above 1,300°K.

A.b.5. Optical properties (10)

Optical absorption spectra in Li_2O were measured at room temperature in the ultraviolet, visible and infrared wave length region as shown in Fig. 4.A.7. The fundamental optical absorption edge was obtained to be 300 μm (4.1 eV), and the number of displaced atoms per n-α reaction in Li_2O was calculated to be 132 on the basis of the Seitz model and the Kinchin-Pease approximation by using the value of the fundamental absorption edge as shown in Fig. 4. A.8.

A.b.6. Crystal structure (11)

Study of crystal structure of Li_2O was done at room temperature using X-ray and neutron diffraction methods. It was found that a cubic structure and a rhombohedral structure were in coexistence in Li_2O. The crystal structure and parameters of the rhombohedral Li_2O are shown in Fig. 4.A.9.

A.b.7. Lattice energy (12)

The lattice energy of Li_2O has been derived by a term-by-term calculation on the assumption that atomic binding force in Li_2O is ionic in character. The value was about twice as large as a value obtained by the Born-Harber cycle, and the effective charge in Li_2O was estimated to be $Li_2{}^{+0.4}O^{-0.8}$.

A.c.1. Compatibility of Li_2O with Fe-Ni-Cr alloys (13)

The reaction of Type 316 stainless steel, Incoloy 800, Hastelloy X-R (a modified Hastelloy X), Inconel 600 and pure nickel with sintered Li_2O

pellets was investigated in the temperature range of 1,073~1,373°K under a dynamic vacuum by using the reaction couple method. The reactions of the alloys with Li_2O pellets were studied by the weight loss method and by the reaction depth method as shown in Fig. 4.A.10 and 11, and proceeded measurably in the range of 1,073~1,173°K and appreciably at 1,273°K, being greatest with Incoloy 800 and least with Hastelloy X-R. These reactions showed the similar pattern as follows. Among the primary alloy constitutions, chromium was exclusively attacked by lithium and oxygen diffusion from the Li_2O into the alloys to form $LiCrO_2$. The $LiCrO_2$ phase grew into a reaction bond (subscale) of uniform thickness beneaty the surface of each alloy. Preferential growth of $LiCrO_2$ along grain boundary was observed only in the case of Inconel 600 to temperatures below 950°C. On the other hand, iron diffused toward the Li_2O pellets to form a volatile double oxide, Li_5FeO_4 above 1,000°C. However, any reaction product associated with nickel was not detected and nickel metal was little attacked by the Li_2O pellet in the whole range of reaction temperature.

A.c.2. Compatibility of Li_2O with molybdenum (14, 15)

The reaction of molybdenum and molybdenum-base alloy (TZM) was investigated in the temperature range of 1,073~1,373°K under a dynamic vacuum. The reaction proceeded measurably at about 1,223°K and appreciably above 1,273°K. Metallographic and X-ray diffraction analyses showed that a reaction product scale was formed at the interface and the scale consisted mainly of Li_4MoO_5. TZM showed slightly higher reactivity with Li_2O compared with molybdenum.

In addition, the vaporization of Li_2O has been studied by molybdenum, tantalum and graphite Knudsen cells in the temperature range 1,200-1,500°K to measure the distribution of the partial pressures under these conditions.

It was found, for example, that due to the reaction of Li_2O with the wall of a molybdenum cell, their partial pressure of Li_3O, which was detected as a stable molecule for the first time, was increased by about a factor of 10 compared with its pressure measured in a platinum cell as shown in Fig. 4.A.12.

A.c.3. Vapor pressure of the reaction product ($LiCrO_2$) (15)

A mass spectrometric Knudsen effusion study of the evaporation of $LiCrO_2$ was done in the temperature range of 1,673~1,873°K. The vapor species over solid $LiCrO_2$ are Li(g), Cr(g), CrO(g), CrO_2(g) and $LiCrO_2$(g), of which Li(g) is predominant as shown in Fig. 4.A.13. The evaporation process of $LiCrO_2$ involves the following reactions: a decomposition reaction, $LiCrO_2(s) = \frac{1}{2} Cr_2O_3(s) + Li(g) + \frac{1}{4} O_2(g)$, and a sublimation reaction, $LiCrO_2(s) = LiCrO_2(g)$. The standard heat of formation of $LiCrO_2$ at 298°K was derived to be -935±26 and -967±17 kJ/mol from 2nd- and 3rd- law treatments, respectively.

A.c.4. Vapor pressure of the reaction product (Li_5FeO_4) (16)

The vapor species and pressures of Li_5FeO_4 were measured in the temperature range of 1,200~1,500°K by means of Knudsen effusion mass spectrometric technique as shown in Fig. 4.A.14. The process of evaporation from liquid Li_5FeO_4 was established and expressed by the reaction $Li_5FeO_4(\ell) = LiFeO_2(s) + 4Li(g) + O_2(g)$. On the other hand, although a congruent process was suggested for the sublimation, it could not be confirmed in detail.

B. Irradiation effects

B.a.1. Tritium release due to a diffusion process (17,18,19,20)

Tritium release due to a diffusion process from neutron-irradiated Li_2O pellets and powders was investigated using the post irradiation annealing method. Fig. 4. B.1 shows the data corresponding to each working temperature of the isochronal treatment which represent the release spectra. Fig. 4.B.2 shows the total fractions of tritium release curves of the condensible form and the noncondensible forms (H_2-T and CH_4-T) from the pellets with various densities. Fig. 4.B.3 shows the ratio of the total H_2-T release to the corresponding CH_4-T release after heating up to about 600°C. The following results were obtained from Figs.15~17.

(i) Tritium was almost completely released under vacuum from the pellets of 72.7, 77.7, 81.5 and 88.5 theoretical density after heating up about 900°K, and the release curves were similar to those obtained for the powders. Those for the pellets seem to shift to a little higher side in comparison with those for the powders. By contrast, tritium was incompletely released under vacuum from the pellets of 91.5% theoretical density after heating up to 900°K, and about 19% of tritium still remained in the pellet. This suggests that pore sizes and pore distribution in the pellet may play a role in the tritium release.

(ii) Tritium released from the pellets of 72.7, 77.7, 81.4 and 88.5% theoretical density was almost completely (95.1 to 98.0%) in the condensible form. Although the chemical state of the condensible form has not been identified yet, if tritium produced by the $^6Li(n,\alpha)^3H$ reaction was present as LiOT in the specimens, tritiated water would follow the dehydration of LiOH consuming the stored energy from neutron-irradiated Li_2O. Tritiated water may be also formed by the reaction of the tritium with moisture. It is, however, not clear whether the tritium is oxidized by the reaction cited above, by the exchange reaction with moisture, or by a combination of the two mechanisms.

(iii) A few percent of tritium was released in the non-condensible form from all the pellets, in which H_2-T, CH_4-T, and C_2-hydrocarbons such as ethylene and acetylence labeled with tritium were observed. This release behavior was also similar to that obtained for the powders. It is well known that Li_2O is easy to pick up moisture and carbon dioxide from the air at room temperature. In fact, mass signals of H_2, CH_4 and CO in the gas chromatograph show the presence of hydrogen and carbon in the pellets. In addition, proton backscattering experiments on Li_2O showed that carbon atoms were distributed over the surface of the pellet, and not homogeneously in the pellet as shown in Fig. 4.B.4. Since the pellets are covered with carbons (the chemical form of the carbons is not idenfified) the CH_4-T seemed to be formed by the reaction of tritium with the carbon at the surface of the pellets.

(iv) The ratio of the total fractions of H_2-T release to those of the CH_4-T for the pellet with 91.5% theoretical density was abruptly larger than those for the pellets with lower densities (Fig. 4.B.3).

B.a.2. Tritium release due to a recoil process (21)

Tritium release due to a recoil process from Li_2O pellets was investigated, and a linear relationship between thermal neutron fluence and the number of tritium atoms ejected from the pellets was observed as shown in Fig. 4.B.5. The range of 2.7 MeV tritium in Li_2O was also determined on the basis of the cosine model, and was compared with the theoretical value (36.4 μm), which was calculated on the basis of the Bragg rule as shown in Fig. 4.B.6.

B.b.1. Microhardness (22)

Thermal neutron dose dependence of microhardness of Li_2O sintered pellets was investigated at room temperature, and the recovery of the microhardness was also investigated by the post irradiation annealing method. The Vickers microhardness of Li_2O (99% theoretical density) was 180±8. The microhardness increased almost linearly from 190 to 220 in the fluence range of $1 \times 10^{15} \sim 5 \times 10^{17}$ neutrons cm^{-2}, and a saturation of the microhardness, 230±8 was observed approximately above 5×10^{17} neutrons cm^{-2} as shown in Fig. 4.B.7. The microhardness after irradiation to 1.0×10^{19} neutrons cm^{-2} was 230±7. The annealing behaviors of the microhardness were investigated for the pellets irradiated to 1.7×10^{18} and 1.0×10^{19} neutrons cm^{-2} after annealing in the temperature range of 473 to 873°K. The microhardness recovered abruptly at about 650°K on one stage as shown in Fig. 4.B.8. It is interesting to note that the tritium release rates from Li_2O pellets with various kinds of densities from 72.7-91.5 theoretical were largest between 630~680°K. This fact suggests that both the recovery of the microhardness and the tritium release may result from the same mechanism as the annihilation of point defects.

B.c.1. ESR study (23,24)

Lattice defects induced by thermal neutron irradiation in Li_2O sintered pellets were investigated by electron spin resonance (ESR) method. The ESR spectra of the Li_2O pellets irradiated to 10^{16}~10^{19} neutrons cm^{-2} have a well-resolved hyperfine structure (having about 20 lines) as shown in Fig. 4.B.9. From intensity ratios of hyperfine lines, such spectra were referred to F^+-centers induced by neutron irradiation. In addition to the above spectra, prominent and isotropic spectra were also observed for the pellets irradiated to 10^{19} neutrons cm^{-2}, as shown in Fig. 4.B.10, and these were considered to arise from colloidal lithium metal centers. These ESR spectra observed for the sintered pellets were in good agreement with those for neutron-irradiated Li_2O pressed powder. The spectra due to the F^+ centers decreased above about 160°C and vanished in the temperature range of 580~620°K, while those of colloidal lithium metal centers disappeared at about 600°C (Fig. 4.B.11).

B.c.2. Optical absorption studies (25)

Optical absorption studies of neutron-irradiated Li_2O pellets were done in the neutron fluence range of 10^{15} to 10^{19} neutrons/cm^2. Four absorption bands were observed at about 4.0 eV(310nm), 3.3 eV(375 nm), 3.0 eV(420 nm) and 2.2 eV(560 nm), respectively (Fig. 4.B.12). The 4.0 eV-band, which appeared at lowest fluence (3×10^{15} neutrons/cm^2), is considered to be a band due to F^+-centers (oxygen-ion vacancies each occupied by one electron). Three other absorption bands are considered to be F-aggregate centers such as F_2(M) and F_3(R) centers, because they are located at higher wavelength of the 4.0 eV-band. The detailed experiments are now in progress.

B.d.1. Dimensional change (26)

Experiments on dose dependence of the lattice parameters and densities are now in progress. Preliminary results showed about 0.1 percent increase of lattice parameter and heavy broadening of X-ray diffraction line as shown in Fig. 4.B.13.

B.e.1. Temperature and neutron flux distribution in Li_2O under pile irradiation (27,28)

Cupsule tests of temperature distribution and neutron flux depletion in the Li_2O pellets under irradiation were done in JRR-2. Preliminary results are shown in Figs. 4.B.14~17.

B.f.1. Ion accelarator's experiments (29)

The depth profile of argon ions in Li_2O pellets implanted to ion fluences of 4.4×10^{17} ions cm^{-2} with energies of 300 and 450 keV was investigated by the proton backscattering method using a 2 MV Van de Graaff accelerator in JAERI. The result is shown in Fig. 4.B.18. It is found that implanted argon ions were diffused into the deeper region of the specimen by elevating of temperature during implantation.

References

(1) T. Tanifuji and S. Nasu ; J. Nucl. Mater. in press. 87 (1979) 189.

(2) T. Takahashi and T. Kikuchi ; JAERI-M 7518 (1978).

(3) I. Shindo, S. Kimura, K. Noda, T. Kurasawa and S. Nasu ; J. Nucl. Mater. 79 (1979) 418.

(4) K. Fukai and S. Nasu ; J. Nucl. Mater. 74 (1978) 351.

(5) H. Kudo, C. H. Chu and H. R. Ihle ; J. Nucl. Mater. 78 (1978) 380.

(6) T. Takahashi and T. Kikuchi ; J. Nucl. Mater. submitted.

(7) T. Kurasawa et al. private communications.

(8) T. Tanifuji, K. Shiozawa and S. Nasu ; J. Nucl. Mater. 78 (1978) 422.

(9) Y. Ohishi et al. private communications.

(10) S. Nasu, T. Tanifuji, K. Kawatsura, K. Uchida and A. Kikuchi ; J. Nucl. Mater. 73 (1978) 127.

(11) N. Masaki, K. Doi, S. Nasu, T. Tanifuji and K. Uchida ; J. Nucl. Mater. 84 (1979) 341.

(12) S. Nasu and H. Takeshita ; J. Nucl. Mater. 75 (1978) 110.

(13) T. Kurasawa, H. Takeshita, S. Muraoka, S. Nasu, M. Miyake and T. Sano ; J. Nucl. Mater. 80 (1979) 48.

(14) H. Takeshita, T. Kurasawa, S. Muraoka, S. Nasu, M. Miyake and T. Sano ; J. Nucl. Mater. 80 (1979) 249.

(15) T. Ohmichi, H. Takeshita, S. Nasu, T. Sasayama, A. Maeda, M. Miyake and T. Sano ; J. Nucl. Mater. 82 (1979) 214.

(16) H. Takeshita, T. Ohmichi, S. Nasu, H. Watanabe, T. Sasayama, A. Maeda, M. Miyake and T. Sano ; J. Nucl. Mater. 78 (1978) 281.

(17) S. Nasu, H. Kudo, K. Shiozawa, T. Takahashi, T. Kurasawa, M. Tachiki and K. Tanaka ; J. Nucl. Mater. 68 (1977) 261.

(18) H. Kudo and K. Tanaka ; Radiochem. Radioanal. Letters, 23 (1975) 57.

(19) H. Kudo, K. Tanaka and H. Amano ; J. Inorg. Nucl. Chem. 40 (1978) 363.

(20) S. Nasu, K. Shiozawa and T. Kurasawa ; J. Nucl. Mater. 68 (1977) 355.

(21) M. Akabori, K. Uchida, K. Noda, T. Tanifuji and S. Nasu ; J. Nucl. Mater. 83 (1979) 330.

(22) S. Nasu, K. Fukai and T. Tanifuji ; J. Nucl. Mater. 78 (1978) 254.

(23) K. Noda et al. private communications.

(24) Y. Ueda, Y. Kazumata and M. Nishi ; Japan. J. Appl. Phys. 16 (1977) 1743.

(25) K. Uchida, K. Noda, T. Tanifuji, S. Nasu and T. Kirihara; J. Nucl. Mater. submitted.

(26) S. Nasu et al. private communications.

(27) S. Nasu, K. Uchida, T. Tanifuji, H. Takeshita, M. Isshiki, T. Miyauchi, K. Tanuma, F. Sasajima; J. Nucl. Mater. in press.

(28) S. Nasu et al. private communications.

(29) S. Nasu, K. Shiozawa, T. Tanifuji and K. Noda; J. Nucl. Mater. 73 (1978) 132.

Table 4.A.1 Melting points and lithium densities of some candidated lithium ceramics for fusion reactors.

Li ceramics	melting point (°C)	Li density (10^{22} cm^{-3})
Li_2O	1423	8.2
$LiAlO_2$	1700	2.3
Li_2SiO_3	1200	3.3
Li_2C_2	>1000	4.1
Li_3N	815	7.2
LiF	848.1	6.1
LiH	686.5	5.9
Li	179.1	4.6

Table 4.A.2 Thermodynamic functions of Li_2O_2 at selected temperatures

TEMP K	J/K·mol	$S_T-S^{*}_{298}$ J/k·mol	H_T-H_{298} J/mol	$-(G_T-H_{298})/T$ J/k·mol
300	80.95	0.465	149.7	56.49
320	81.31	5.359	1772	56.68
340	81.79	10.02	3402	57.15
360	82.35	14.47	5044	57.84
380	82.99	18.74	6697	58.70
400	83.69	22.84	8364	59.69
420	84.44	26.80	10045	60.78
440	85.23	30.61	11742	61.96
460	86.04	34.31	13455	63.20
480	86.89	37.89	15184	64.50
500	87.76	41.37	16931	65.83
520	88.65	44.75	18695	67.20
540	89.55	48.05	20477	68.60
560	90.48	51.26	22277	70.01

* S_{298} = 56.484 (J/K·mol) from JANAF Table

Table 4.A.3 Heat capacity and derived thermodynamic functions of lithium oxide at selected temperatures.

Temp. (K)	C_p (J/K · mol)	$S_T - S_{298}$ (J/K · mol)	$H_T - H_{298}$ (J/mol)	$-(G_T - H_{298})/T$ (J/K · mol)
300	50.39	0.311	92.88	37.89
320	53.96	3.680	1137	38.02
340	56.95	7.044	2247	38.32
360	59.49	10.37	3412	38.78
380	61.67	13.65	4625	39.37
400	63.56	16.86	5877	40.06
420	65.22	20.00	7166	40.83
440	66.68	23.07	8485	41.68
460	67.98	26.07	9832	42.58
480	69.14	28.98	11203	43.53
500	70.20	31.83	12597	44.52
520	71.15	34.60	14010	45.55
540	72.02	37.30	15442	46.60
560	72.83	39.94	16891	47.66
580	73.57	42.50	18355	48.75
600	74.25	45.01	19833	49.85
620	74.89	47.46	21325	50.95
640	75.49	49.84	22829	52.06
660	76.06	52.18	24344	53.10
680	76.59	54.45	25871	54.30
700	77.10	56.68	27408	55.42
720	77.57	58.86	28954	56.54
740	78.03	60.99	30510	57.65
760	78.47	63.08	32075	58.76
780	78.89	65.12	33649	59.87
800	79.29	67.12	35231	60.98
820	79.68	69.09	36821	62.07
840	80.05	71.01	38417	63.17
860	80.41	72.90	40023	64.25
880	80.76	74.75	41634	65.33
900	81.11	76.57	43253	66.40
920	81.44	78.36	44879	67.47
940	81.76	80.11	46511	68.52
960	82.08	81.84	48149	69.57
980	82.39	83.53	49794	70.61
1000	82.69	85.20	51444	71.65
1020	82.99	86.84	53101	72.67
1040	83.28	88.45	54764	73.69
1060	83.56	90.04	56432	74.70
1080	83.84	91.61	58106	75.70

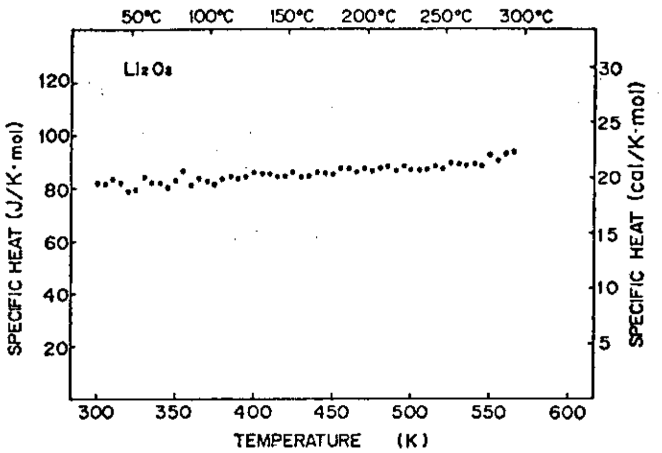

Fig.4.A.1 Heat capacity of Li_2O_2

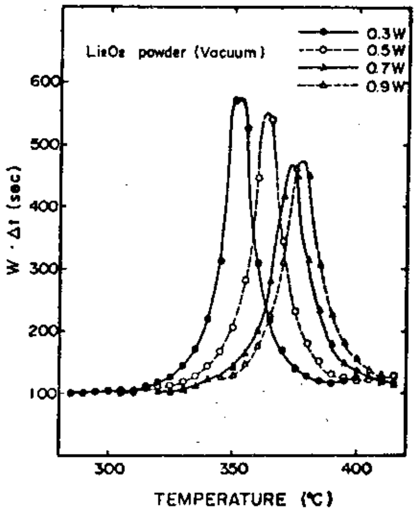

Fig.4.A.2 Endothermic decomposition reaction of Li_2O_2 in vacuum in the various conditions.

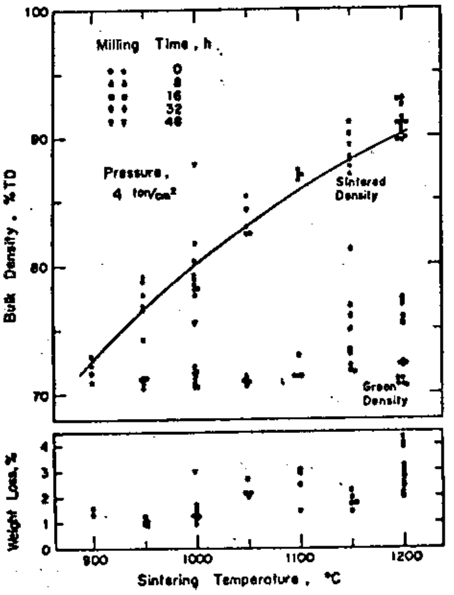

Fig.4.A.3 The effect of sintering temperature in vacuum on bulk density, sintering time 4h.

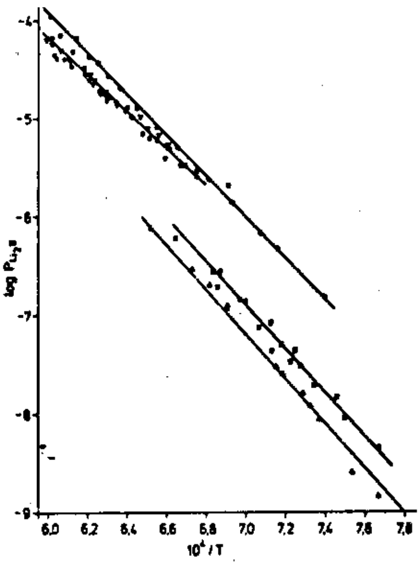

Fig.4.A.4 Partial pressures of Li_2O over Li_2O (s) as a function of the reciprocal temperature : (○) with platinum Knudsen cell, (□) with molybdenum Knudsen cell (■) with tantalum Knudsen cell, (▲) Berkowitz et al. (▽) Hildebrand et al., and (○) White et al.

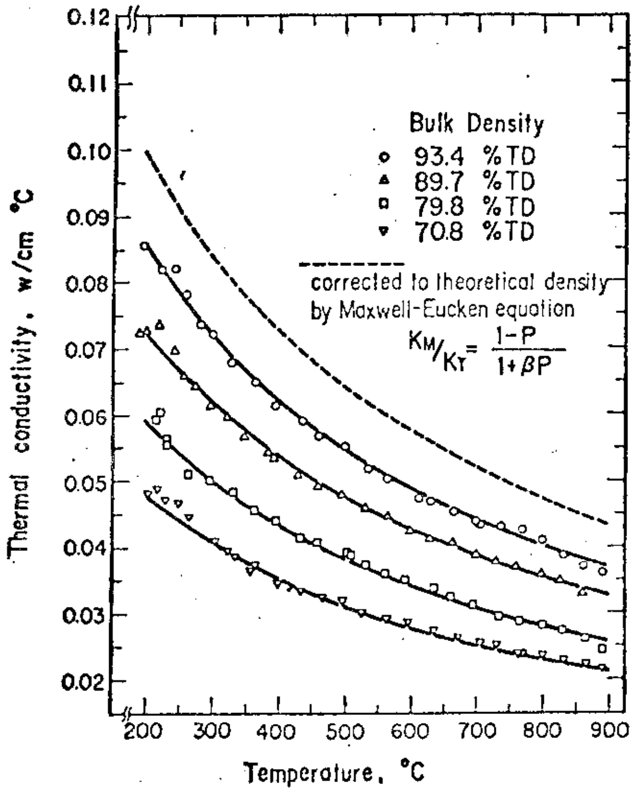

Fig 4.A.5 Temperature dependence of thermal conductivity of Li_2O for various densities.

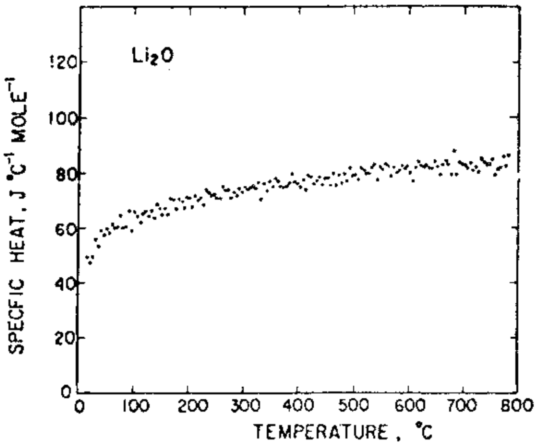

Fig 4.A.6 Heat capacity of Li_2O.

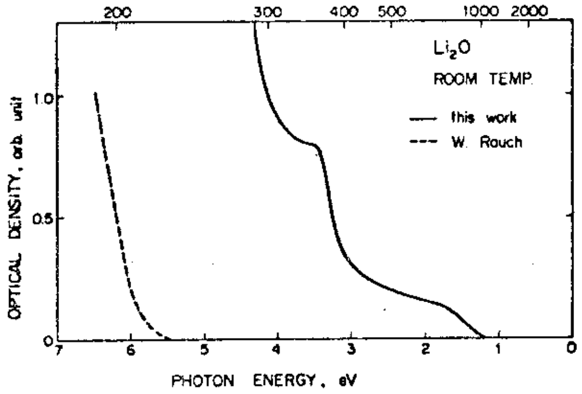

Fig. 4.A.7 Optical absorption spectrum of Li_2O in the interval 1.0-7.0 eV at room temperature.

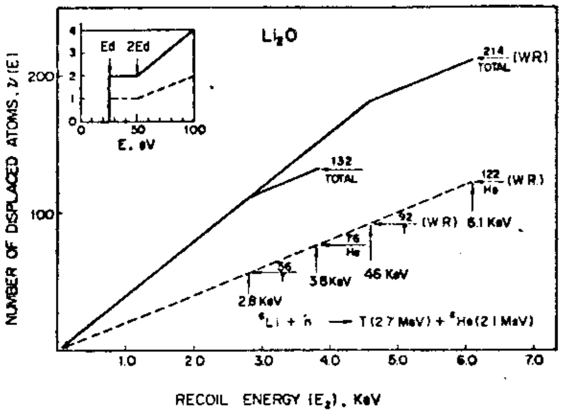

Fig. 4.A.8 Average number of displaced atoms produced by the $^6Li(n,\alpha)^3H$ reaction in Li_2O.

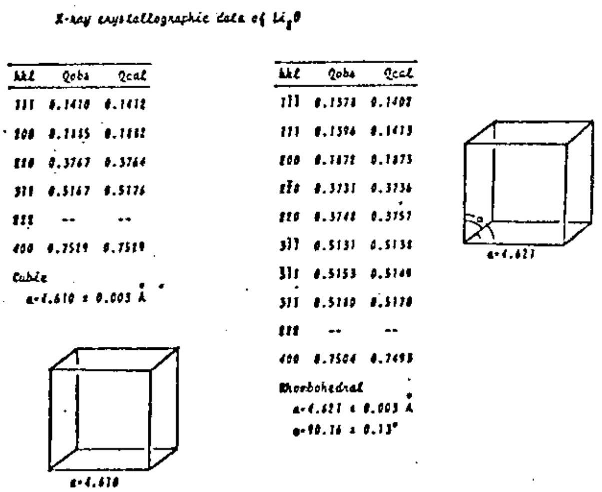

X-ray crystallographic data of Li_2O

hkl	Qobs	Qcal
111	0.1410	0.1412
200	0.1885	0.1882
220	0.3767	0.3764
311	0.5167	0.5176
222	--	--
400	0.7519	0.7519

Cubic
a=4.610 ± 0.003 Å

hkl	Qobs	Qcal
111	0.1378	0.1407
111̄	0.1396	0.1413
200	0.1872	0.1875
2̄20	0.3731	0.3736
220	0.3748	0.3757
31̄1̄	0.5131	0.5134
311̄	0.5153	0.5149
311	0.5180	0.5170
222	--	--
400	0.7504	0.7493

Rhombohedral
a=4.621 ± 0.003 Å
α=90.16 ± 0.13°

Fig. 4.A.9 X-ray crystallographic data of Li_2O

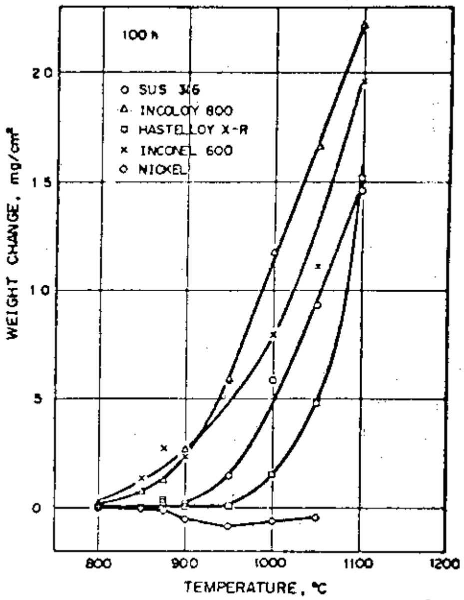

Fig. 4.A.10 Relationship between weight change and temperature for a reaction period of 100h in the reaction of Fe-Ni-Cr based alloys and Li_2O pellets.

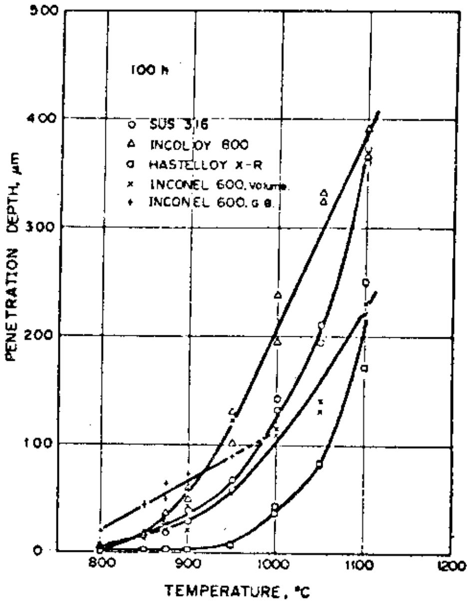

Fig. 4.A.11 Relationship between attacked depth and temperature for a reaction period of 100h in the reaction of Fe-Ni-Cr based alloys and Li_2O pellets.

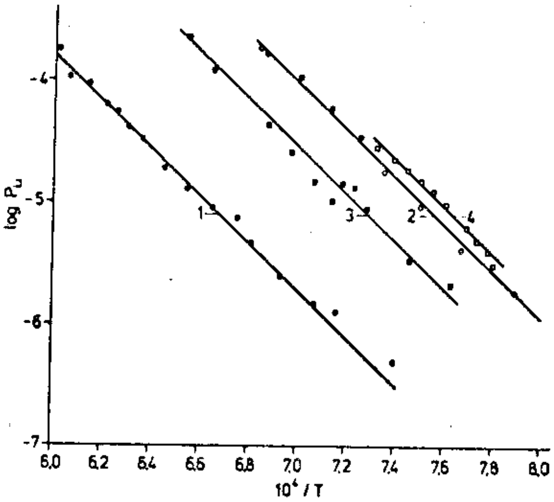

Fig. 4.A.12 Partial pressures of Li_2O over $Li_2O(S)$ as a function of the reciprocal temperature measured with (1) platinum, (2) molybdenum and (3) tantalum Knudsen cells.

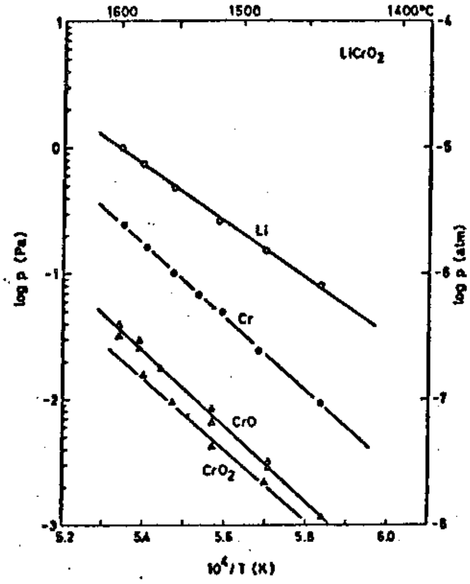

Fig.4.A.13 Partial pressures of Li(g), Cr(g), CrO(g) and CrO_2(g) over $LiCrO_2$(S).

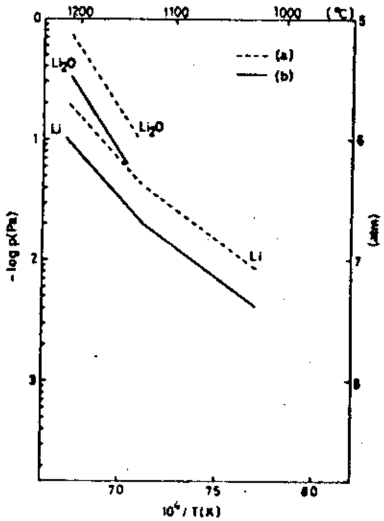

Fig.4.A.14 Partial pressures of Li(g) and Li_2O(g) over Li_5FeO_4(S) obtained by (a) the absolute method and (b) the reference method.

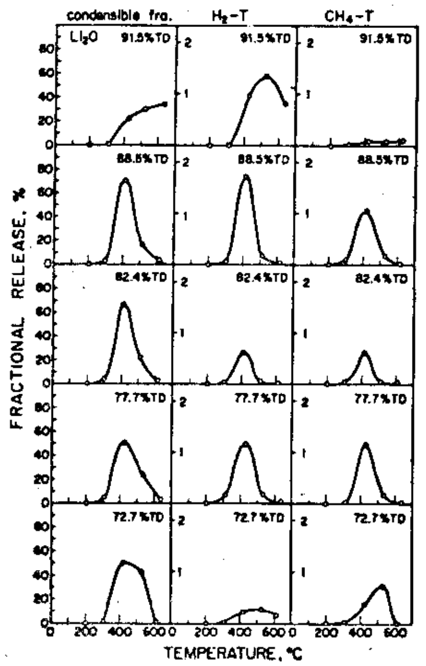

Fig.4.B.1 Tritium release spectra for the condensible form and the noncondensible form (H_2-T and CH_4-T) from neutron-irradiated Li_2O pellets having various densities under vacuum.

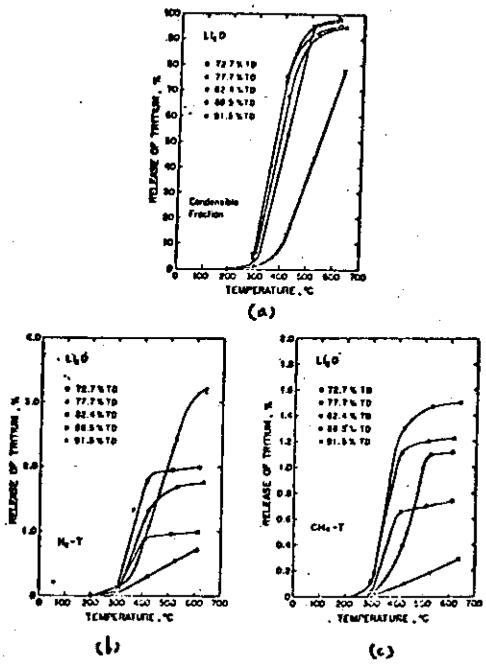

(a)

(b)

(c)

Fig.4.B.2 Total fractions of tritium release curves for the condensible form (a) and the non-condensible [H_2-T(b) and CH_4-T(c)] from neutron irradiated Li_2O pellets having various densities under vacuum.

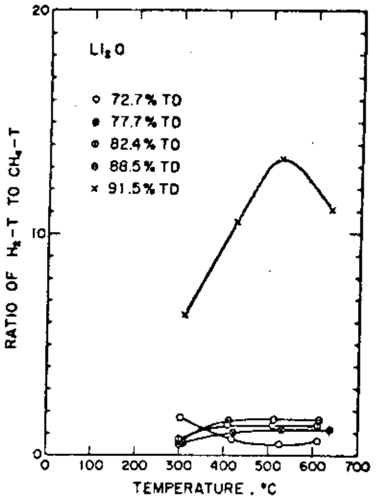

Fig. 4.B.3 Ratio of the total fraction of H_2-T release to those of the CH_4-T.

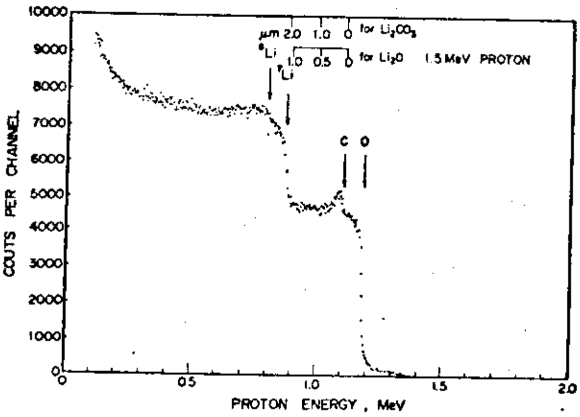

Fig. 4.B.4 Backscattering spectrum for 1.5 MeV proton incident an sintered Li_2O pellets. The arrows indicate the energy positions for scattering from surface atoms of Li, C and O.

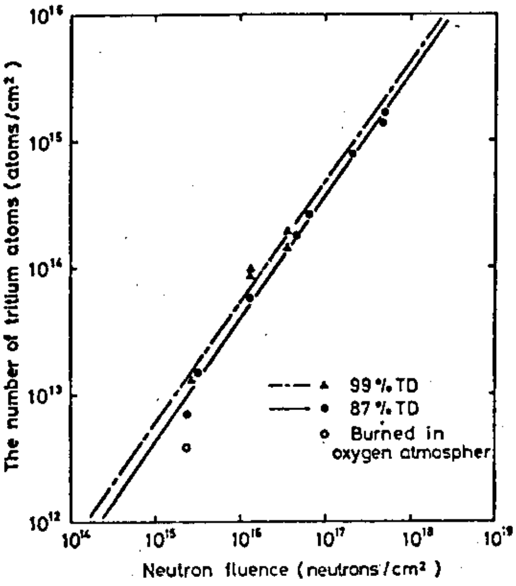

Fig. 4.B.5 The number of tritium atoms ejected from Li_2O pellets versus neutron fluence, showing a linear relationship.

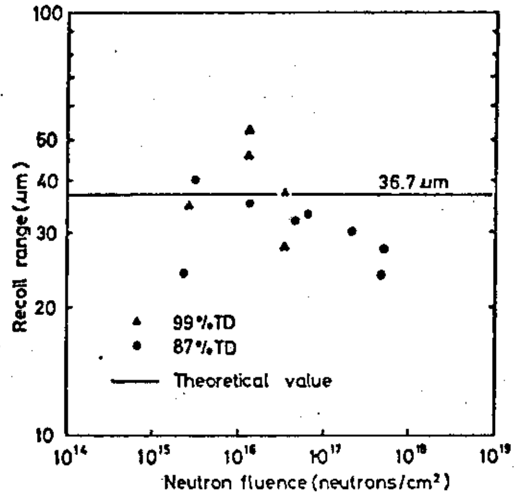

Fig. 4.B.6 The experimental and the theoretical recoil range of tritium in Li_2O.

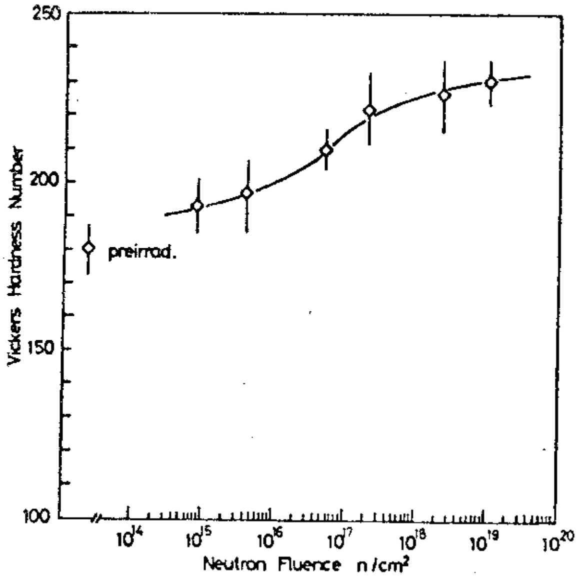

Fig.4.B.7 Vickers microhardness of Li_2O pellets as a function of neutron dose.

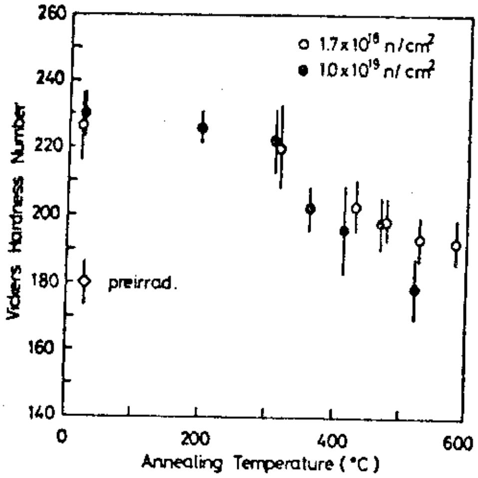

Fig.4.B.8 Microhardness recovery on annealing for Li_2O pellets irradiated to 1.7×10^{18} and 1.0×10^{19} neutrons/cm^2.

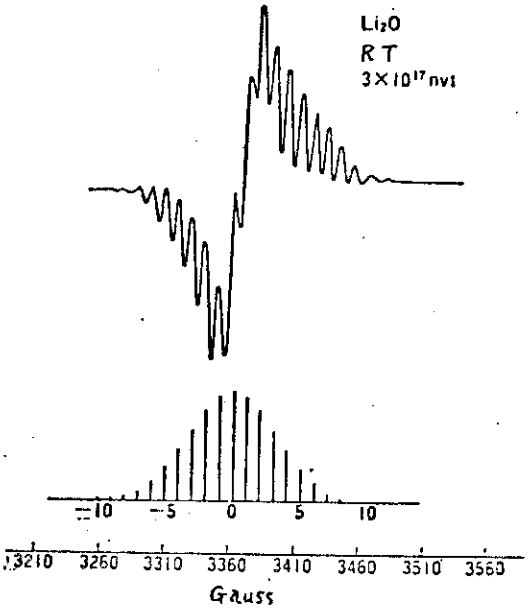

Fig.4.B.9 ESR spectrum of F^+ centers in neutron-irradiated Li_2O pellets. Hyperfine structures between electrons of F^+ centers and surrounding Li nuclei are clearly observed. Predicted patterns of resonance lines are shown by bars under the spectrum.

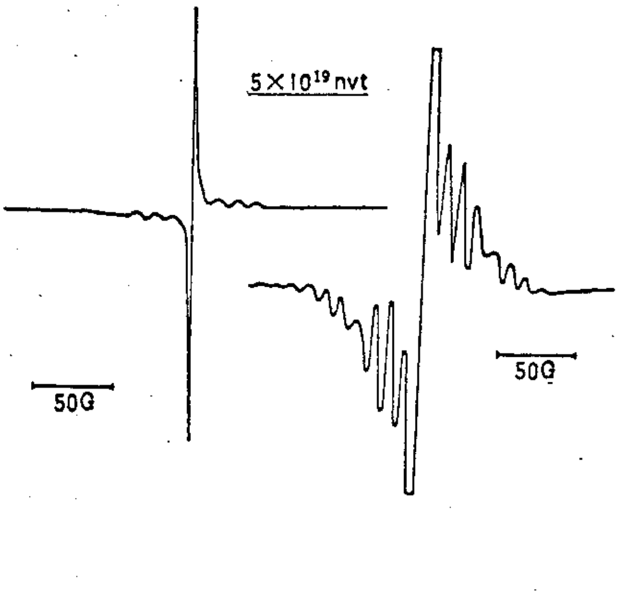

Fig.4.B.10 A spectrum due to colloidal Li metal.

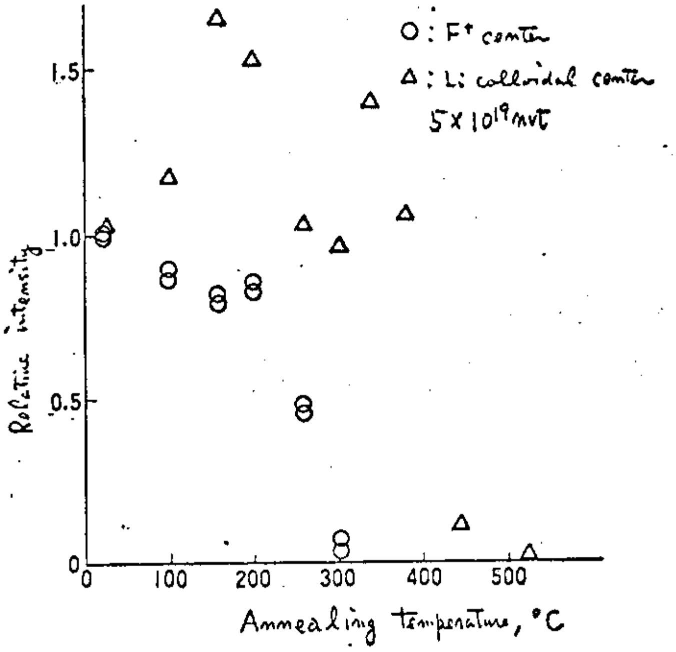

Fig. 4.B.11 Annealing curves of F^+ centers and colloidal Li metal centers.

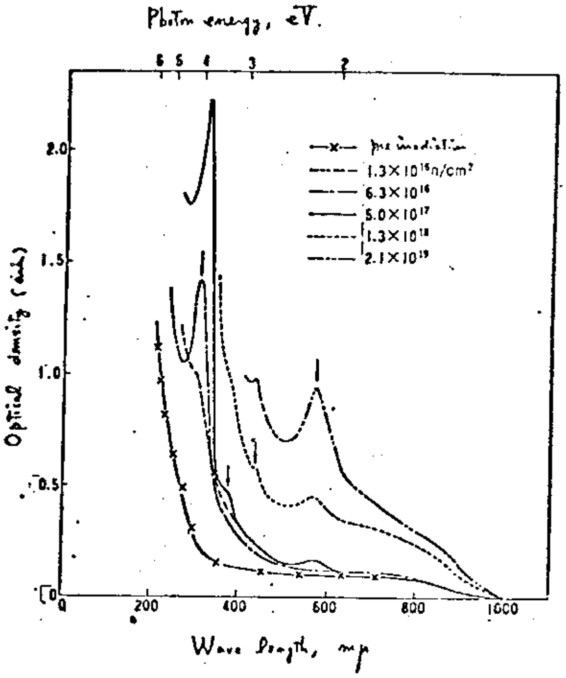

Fig. 4.B.12 Optical absorption spectrum of neutron irradiated Li_2O pellets.

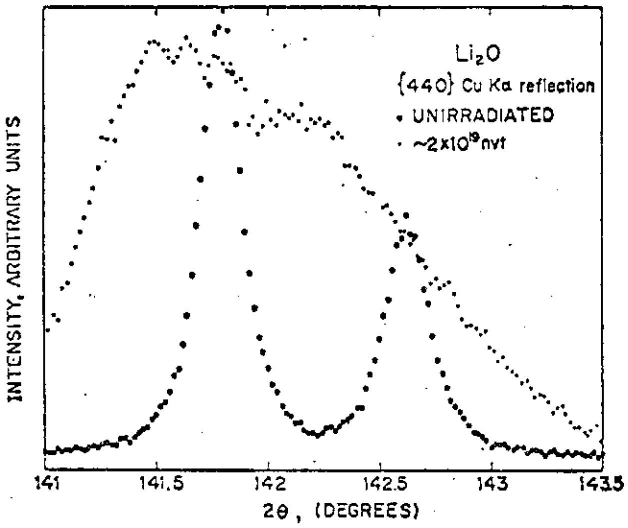

Fig. 4.B.13 X-ray diffraction patterns of (440) of Li_2O before and after irradiation to 2 × 10^{19} neutrons/cm^2.

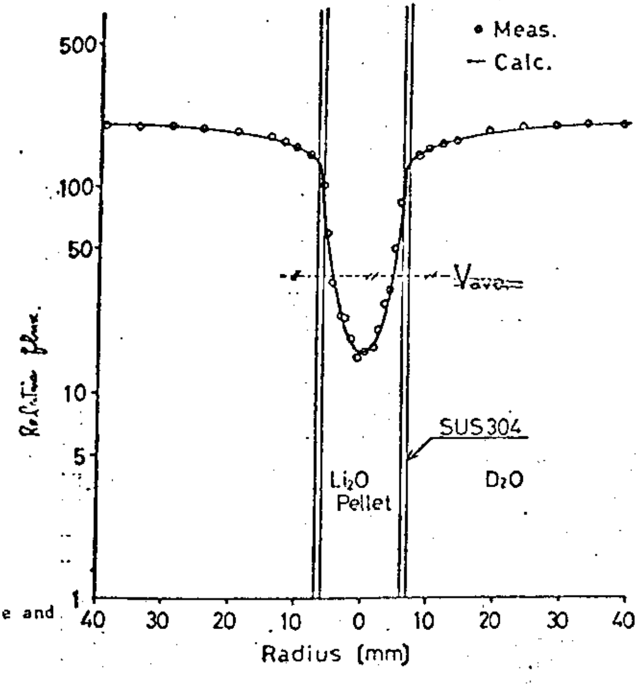

Fig. 4.B.14 Thermal neutron depression of Li_2O pellets.

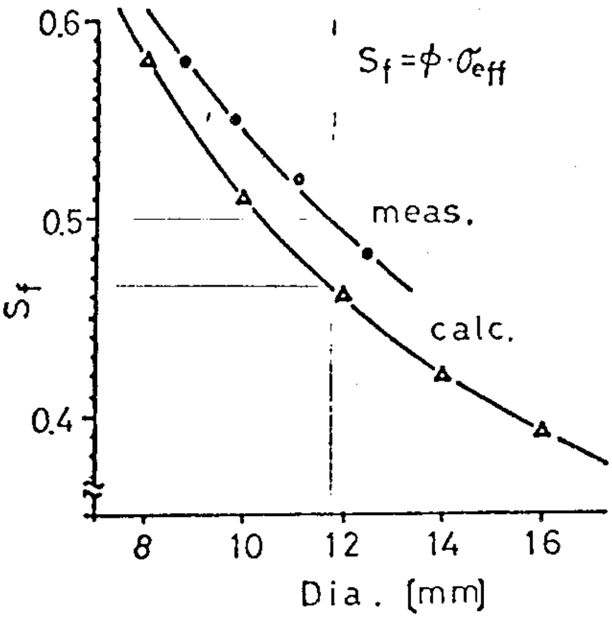

Fig. 4.B.15 Relation between self shielding factor and Li_2O pellet diameter.

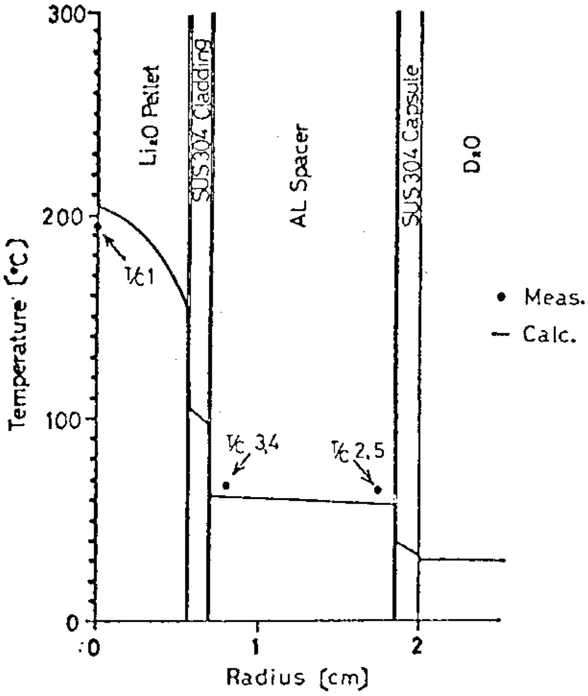

Fig. 4.B.16 Temperature distribution in Li_2O pellets under the conditions of 10 MW in JRR-2.

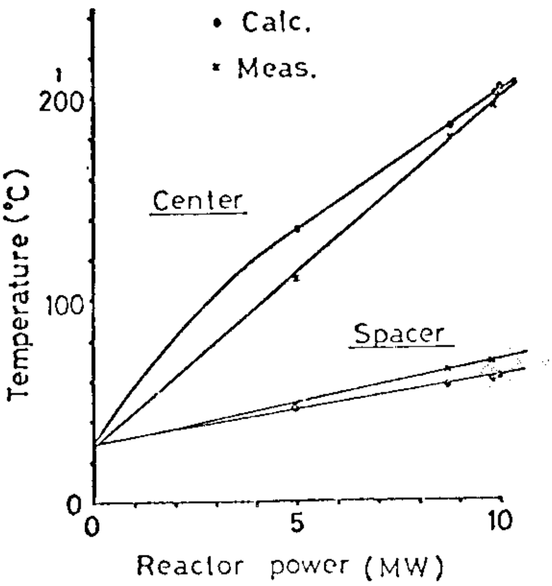

Fig. 4.B.17 Pellet center and surface temperatures versus thermal reactor power.

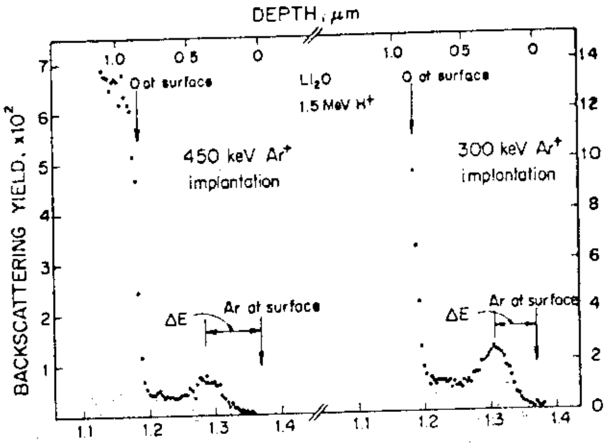

Fig. 4.B.18 Backscattering spectra for 1.5 MeV proton.

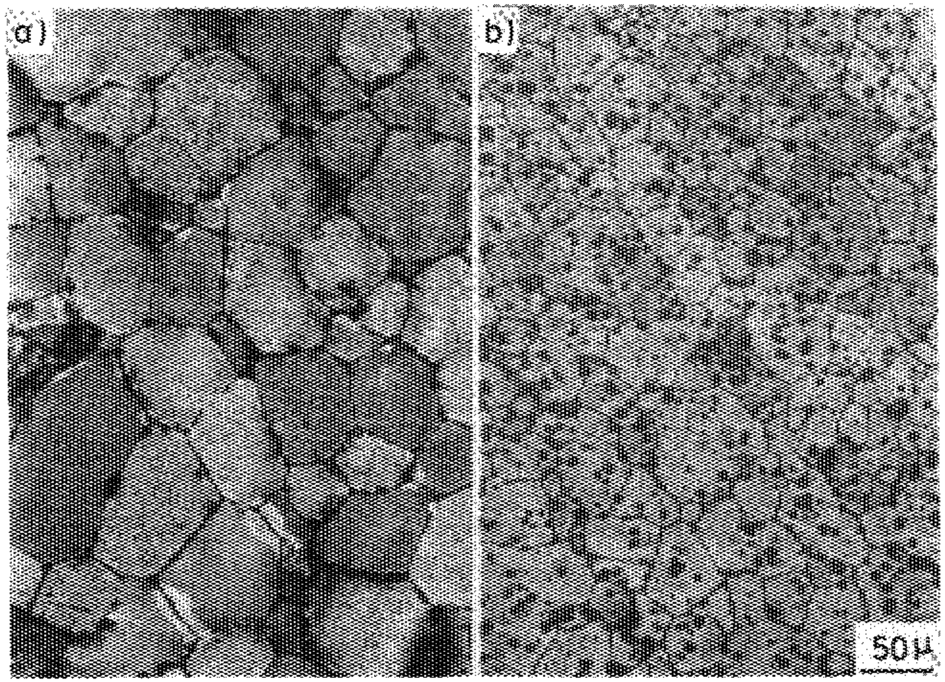

Photo. 4.A.1 Optical micrographs of the polished and etched cross-sections of (a) a dense Li_2O pellet of 99% theoretical density and (b) a sintered Li_2O pellet of 93% theoretical density.

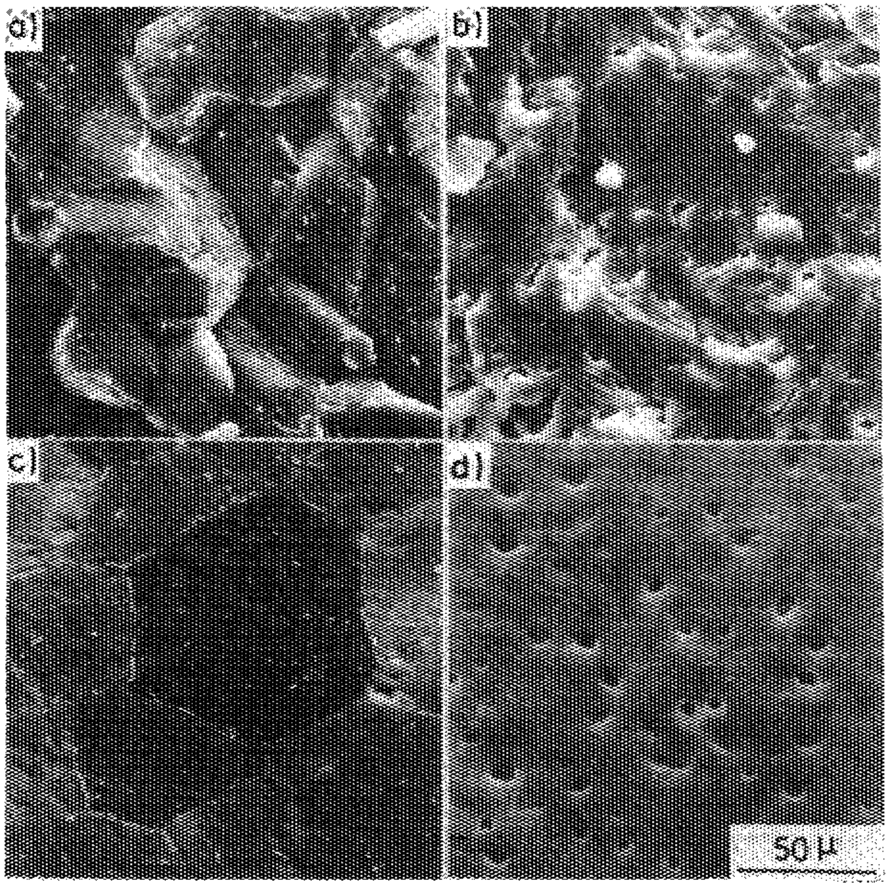

Photo. 4.A.2 Scanning electron micrographs of the fractured surfaces, (a,b) and the etched and polished cross-sections, (c,d). The dense Li_2O pellet in (a) and (c) is of 99% theoretical density, and of 93% theoretical density in (b) and (d).

5. DATA BASE FOR MAGNET MATERIALS CHOICE

A. Anticipated Operating Conditions

A parametric analysis is made on the durability and performance of superconducting composite conductors under irradiation$^{1)}$. The procedure used to evaluate neutron irradiation effect on conductors is as follows. The resistivity ρ of the stabilizer is given in the form: $\rho = \rho_o + \rho_m + \rho_{irr}$, where ρ_o is the residual resistivity, ρ_m the magneto-resistance, ρ_{irr} the radiation induced resistivity. For the stability of the magnet, Stekly's cryogenic stabilization is applied and the condition that the recovery current is equal to the critical current is used. Parameters used for the analysis are given in Table 5.A.1.

Figs.5.A.1 and 2 give the maximum overall transport current density (J_T^m) for a Nb-47.6%Ti and Nb_3Sn, respectively as a function of a fluence at 8T with stabilizer of Cu or Al having various initial resistivities. If the conductor is stabilized by Al, J_T^m decreases more rapidly than in case of Cu. This is mainly due to the larger radiation induced resistivity increase of Al compared with Cu. The J_T^m of NbTi decreases mainly by the stabilizing effect through resistivity change by neutron irradiation. On the other hand, J_T^m of Nb_3Sn fall more steeply because of the changes in the superconducting properties. Fig.5.A.3 shows the J_T^m of Nb_3Sn stabilized by Cu and Al plotted as a function of fluence with applied field B changed. J_{TO} to produce the required magnetic field is fixed on the J_T^m versus fluence curves. If the J_T^m for some conductor degrades below J_{TO} within its operation period, the magnet cannot generate sufficient magnetic field to maintain the original performance of the magnet.

B. Irradiation Effects to Superconducting Properties

The critical current of pure V and Nb, single core Nb-50wt%Ti coated by Cu, single core Nb-Ti-Zr alloy coated by Cu, uncoated Nb_3Sn, single core and multifilament Nb_3Sn coated by Cu are measured after fast neutron irradiation at about 5K and during subsequent annealings2).

The critical current density (J_c) of pure V and Nb remarkably increases after fast neutron irradiation at low temperature. The large recovery of J_c occurs below the room temperature. The recovery is probably due to the reduction of the size of cascade zones produced by neutron irradiation and/or the defect density in the zone. In Fig.5.B.1, results of critical current (I_c) changes for Nb-Ti and uncoated Nb_3Sn (doped with Ge and with Zr) after irradiation of 3.3×10^{17} nvt at low temperature are shown. J_c in Nb-Ti is observed to decrease after irradiation. Fig.5.B.2(a) and (b) show the I_c versus the applied magnetic field (H) for single core Nb_3Sn, NbTiZr coated by Cu and single core NbTi and multifilament Nb_3Sn coated by Cu before and after low temperature irradiation, respectively. I_c of multifilament Nb_3Sn increases after low temperature irradiation. I_c of NbTi alloy and Nb_3Sn does not change after irradiation. For irradiation at about 70°C, Okada and collaborators3,4) studied the effect of the neutron irradiation at ambient temperature on Nb-Ti alloys. They indicate that fast neutron irradiation to a fluence of 1.3×10^{18} nvt of Nb-60 at %Ti alloys containing α-Ti precipitates results in a reduction of J_c and of the critical temperature of 6%. For Nb-48 at %Ti alloys with large J_c, small nonsystematic changes in J_c are observed after irradiation to a fluence of 4.2×10^{18} (E > 1 MeV).

C. Irradiation Effects to Electrical Resistance of Cryogenic Stabilizers (Cu, Al)

The amount of electrical resistivity increases are measured after fast neutron irradiation at about 5K(5,6). Table 5.C.1 shows the damage rates on Cu. The resistivity ratio at room temperature to 4.2K is about 900. By cold work before irradiation, the damage production rate increases and the amount of recovery by annealing up to room temperature enhances compared with as-annealed specimen. Fig.5.C.1 shows the fractional isochronal recovery curves for 6 minutes pulse annealings at each temperature. Fig.5.C.2 shows the isochronal recovery curves of three different treatments: as-annealed specimen, first irradiated then deformed by small deformation of a few percent surface shear strain at 4.2K, and specimen deformed at 4.2K without irradiation. A similar curves for Al are shown in Fig.5.C.3 about 20% of the resistivity increase after irradiation in Cu remains after annealing at room temperature. For deformation at 4.2K, a considerable amount of the resistivity increase in Cu remains after annealing at room temperature.

F. Irradiation Effect to Thermal and Electrical Insulators

Several organic insulators are irradiated in the fission reactor at about 5K and their mechanical properties are measured at liquid nitrogen temperature and liquid helium temperature$^{7,8)}$.

Specimens used are polypropylene, polycarbonate, Mylar (polyester), Nomex (nylon paper), Kapton (polyimide), Vespel (polyimide), Epoxy resins and fiber reinforced epoxies. The thickness of specimens for tensile test are 65μ for polypropylene, 75μ for polycarbonate, 85μ for Mylar, 200μ for Nomex and 50μ for Kapton. They are tested in liquid nitrogen by tension. The size of specimens for compression test are circular cylinder 3mm diameter by 4mm long for Epoxy resins and composites, and then cylinder with dimension of $2 \times 2 \times 4$ mm^3 for Vespel. These specimens for compression test are tested in liquid nitrogen and liquid helium. The irradiation are performed at about 5K in LHTL. Tensile and compression tests are carried out using an Instron type machine at liquid nitrogen temperature (77K) and liquid helium temperature (4.2K) without warmed-up after irradiation.

For the tensile test at 77K, poly-propylene, poly-carbonate and Mylar become very brittle, and the breaking stress and elongation of Nomex decrease after fast neutron irradiation 1.7×10^{17} nvt with γ dose 4.5×10^8R. The breaking stress of Kapton, marketed under the description of H-film, decreases at neutron fluence 3.3×10^{17} nvt with γ dose 8.8×10^8R. Fig.5.F.1 shows the breaking stress of polymers described above as a function of the absorbed dose.

For the compression test at 77K, the relation between the breaking stress and irradiation fluence of epoxy resins which are Epikote 828 hardened by aliphatic amine, aliphatic amine (cyclic), filled aliphatic amine, aromatic amine and aromatic amine is shown in Fig.5.F.2. Vespel and fiber reinforced epoxies hardened by acid anhydride show the most excellent properties against the absorbed dose of 1.1 × 10^9 rad in the compression test at 77K.

Fig.5.F.3 (a), (b), (c), (d), and (e) show the results of Epoxy resins of Epokote 828 hardened by aliphatic amine and by aromatic amine, glass fiber reinforced epoxy, carbon fiber reinforced epoxy and Vespel tested at 4.2K without warmed up after irradiation of the absorbed dose 1.1 × 10^9 rad at 5K. The strength of epoxy resins hardened by amine shows a remarkable decrease after low temperature irradiation.

Vespel and fiber reinforced epoxies hardened by acid anhydride have a good radiation resistance for the mechanical test at 4.2K after low temperature irradiation of 1.1 × 10^9 rad.

To compare the effects of neutron irradiation with that of γ rays, two separate irradiation experiments are made, which are reactor irradiation in 77K and Co-60 γ ray irradiation at 77K9). Fig.5.F.4 (a) and (b) show the changes of the breaking stress distribution caused by γ irradiation and fast neutron fluence 10^{16} nvt with γ dose 3 × 10^8 rad, respectively. The considerable difference of the fracture behaviour are observed between neutron and γ ray irradiation. Therefore, it is dangerous to simulate neutron irradiation effects by that of γ irradiation.

References

1) T. Okada and Y. Hayashiuchi : J. Nucl. Materials 72 (1978) 177

2) S. Takamura and S. Okuda : J. Nucl. Materials 72 (1978) 244

3) H. Tsubakihara, T. Okada, T. Suita, T. Horiuchi, K. Matsumoto and S. Tsurutani : J. Nucl. Sci. Tech. 11 (1974) 452

4) T. Okada, H. Tsubakihara, S. Katoh, T. Horiuchi, T. Monjhu and S. Tsurutani : Proc. Conf. Radiation Effects and Tritium Technology for Fusion Reactors, Vol.2, CONF-750989 (1975)

5) S. Takamura, H. Maeta and S. Okuda : J. Phys. Soc. Japan 26 (1969) 1120

6) S. Takamura, R. Hanada and S. Okuda : J. Phys. Soc. Japan 30 (1971) 1360

7) S. Takamura and T. Kato : Nonmetallic Materials and Composites at low Temperatures, edited by A.F. clark et al. (Plenum Press, New York and London, 1978) P.155

8) S. Takamura and T. Kato : to be published

9) S. Nishijima and T. Okada : 6th Intern. Conf. Magnet Technology (MT-6) paper 121, Bratislava, Czechoslovakia (1977)

Table 5.A.1 Data used for the analysis in this study.

Superconductor	Nb–47%Ti a)	Nb_3Sn b)
Heat treatment	Aged 10 min at 380°C	–
J_c(A/cm^2)	3.2×10^4 before irr. 2.7×10^4 after 4.2×10^{18} n/cm^2	3.0×10^5 before irr. 1.5×10^4 after 7.8×10^{18} n/cm^2
T_c(K)	Little change	$T_c/T_{c0} \simeq 0.5$ after 1×10^{19} n/cm^2
Stabilizer	**Cu**	**Al**
ρ_0 (ohm · cm)	$10^{-8} \sim 10^{-7}$	$10^{-9} \sim 10^{-7}$
ρ_m(ohm · cm)	40×10^{-9} at 8 T	5×10^{-9} at 8 T
ρ_{irr}(ohm · cm/n/cm^2)	6.2×10^{-26} [Total resistivity $\rho = \rho_0 + \rho_m + \rho_{irr}$]	21×10^{-26}
Heat transfer coefficient h and heat flux q		
h(W/cm^2 · K)	$h = 1.32\,(T - T_b)^{0.4}$	for both Cu–liq. He and AL–liq. He
q(W/cm^2)	$q = 1.32\,(T - T_b)^{1.4}$	
	T = Temperature of stabilizer	
	T_b = Bath temperature	

For more details, see a) T. Okada et al., ref. [6], b) A. Sweedler et al., ref. [7].
For the definition of fast neutron flux, $E_n > 0.1$ MeV is used for a), whereas $E_n > 1.0$ MeV in case of b).

Table 5.C.1 The damage rates on Cu

	Neutron fluence (>0.1 MeV)(nvt)	resistivity increase ($\times 10^{-9}$ Ωcm)
as-annealed	12×10^{16}	7.4
as-annealed	4.1×10^{16}	2.5
as-annealed	4.1×10^{16}	2.9
53% twisted	4.1×10^{16}	3.2
106% twisted	4.1×10^{16}	3.2

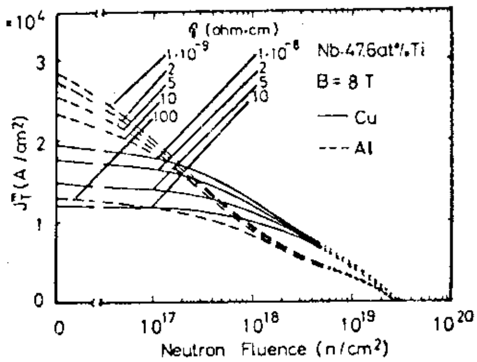

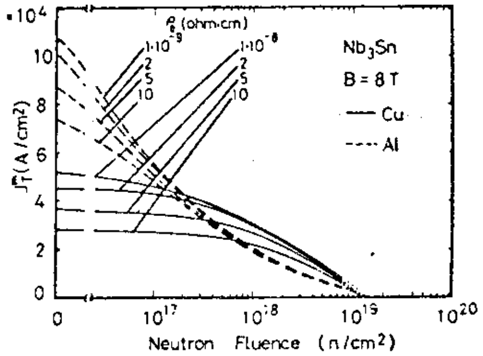

Fig.5.A.1 Maximum transport current density J_T^m at 8T is plotted as a function of fluence in case of Nb-46%Ti. The influence of initial residual resistivity of stabilizer is also shown.

Fig.5.A.2 Maximum transport current density at 8T is plotted as a function of fluence in case of Nb_3Sn (19 multifilament) conductor.

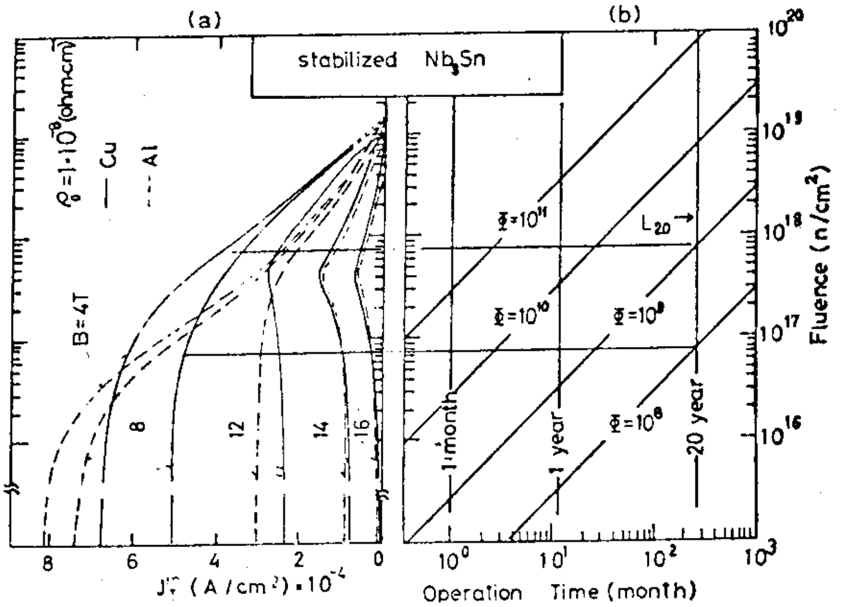

Fig.5.A.3(a) Maximum transport current density J_T^m of Nb_3Sn stabilized by Cu and Al.($\rho_0 = 1 \times 10^{-8}$ ohm·cm) is plotted as a function of fluence with applied field B changed, (b) A knife-edge diagram is shown to evaluate tolerable fluence for required overall current density to assure the necessary magnetic field in fusion reactor.

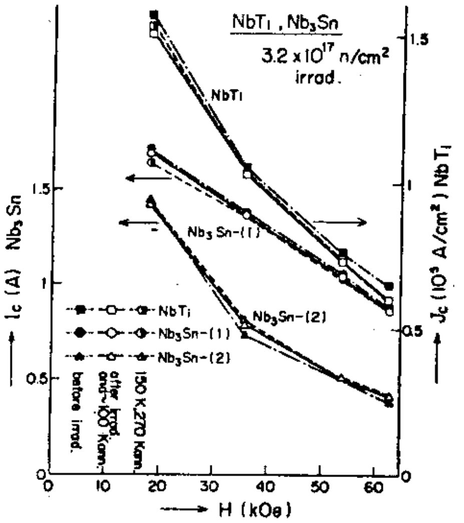

Fig.5.B.1 Critical current of Nb_3Sn doped with Ge (Nb_3Sn-(1)) and with Zr(Nb_3Sn-(2)) and critical current density of NbTi as a function of magnetic field, after fast neutron irradiation for 80 h at ~5K.

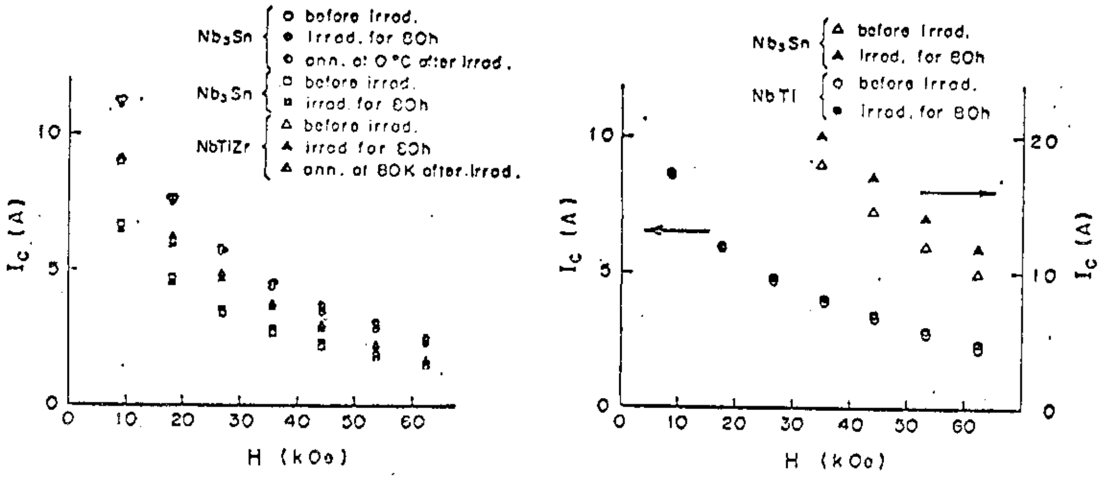

(a)

(b)

Fig.5.B.2 Critical current of Nb_3Sn and NbTiZr coated by Cu(a) and Nb_3Sn and NbTi coated by Cu(b) as a function of magnetic field, after fast neutron irradiation for 80h at 5K.

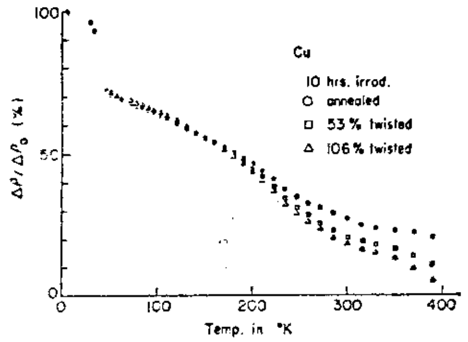

Fig.5.C.1 Fractional isochronal recovery curves for 6 minutes pulse annealings at each temperature for the annealed and the cold worked Cu.

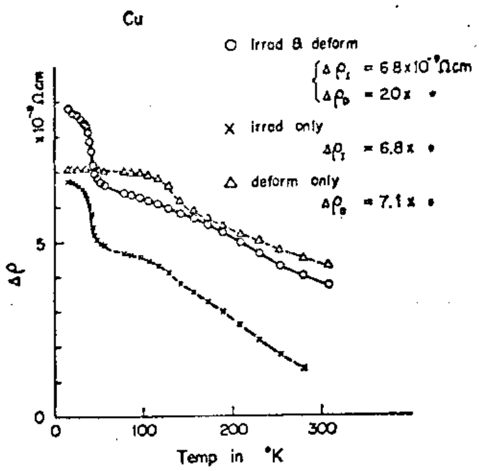

Fig.5.C.2 The isochronal recovery curves for Cu specimens of three different treatments: 30h irradiation at low temperature of as-annealed specimen (treatment 1)(×), as-annealed specimen is first irradiated for 30h then deformed by twisting at 4.2°K (treatment 3) (initial resistivity increase is normalized to that of treatment 1)(○), specimen deformed at 4.2°K without irradiation (treatment 2)(△).

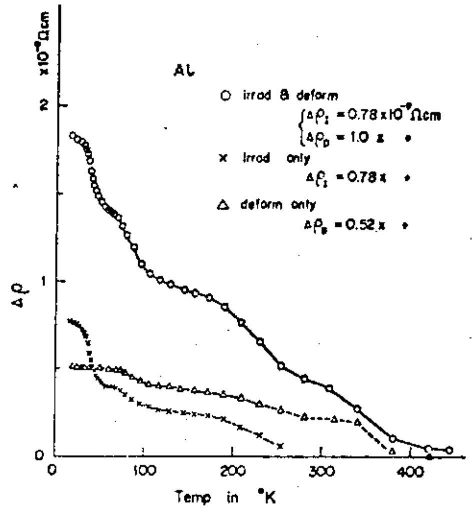

Fig.5.C.3 The isochronal recovery curves for Al specimens of three different treatments, treatment 1 (×), treatment 2(△) and treatment 3(○).

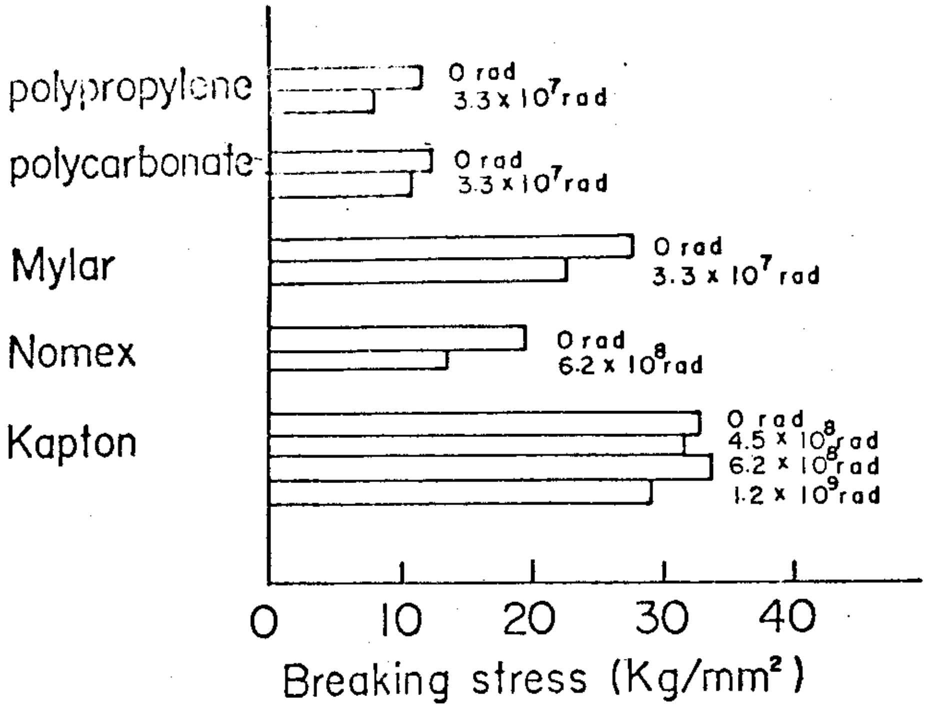

Fig.5.F.1 Relation between breaking stress and absorbed doses for several organic materials.

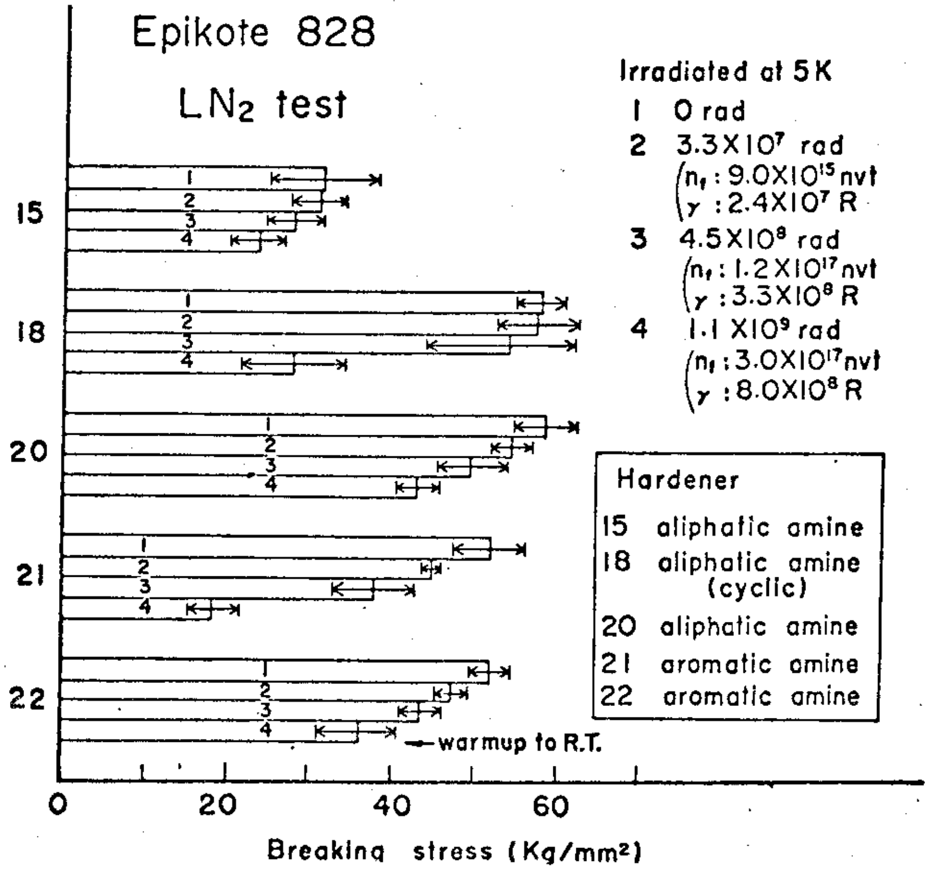

Fig.5.F.2 Relation between breaking stress and absorbed dose for Epoxy resins.

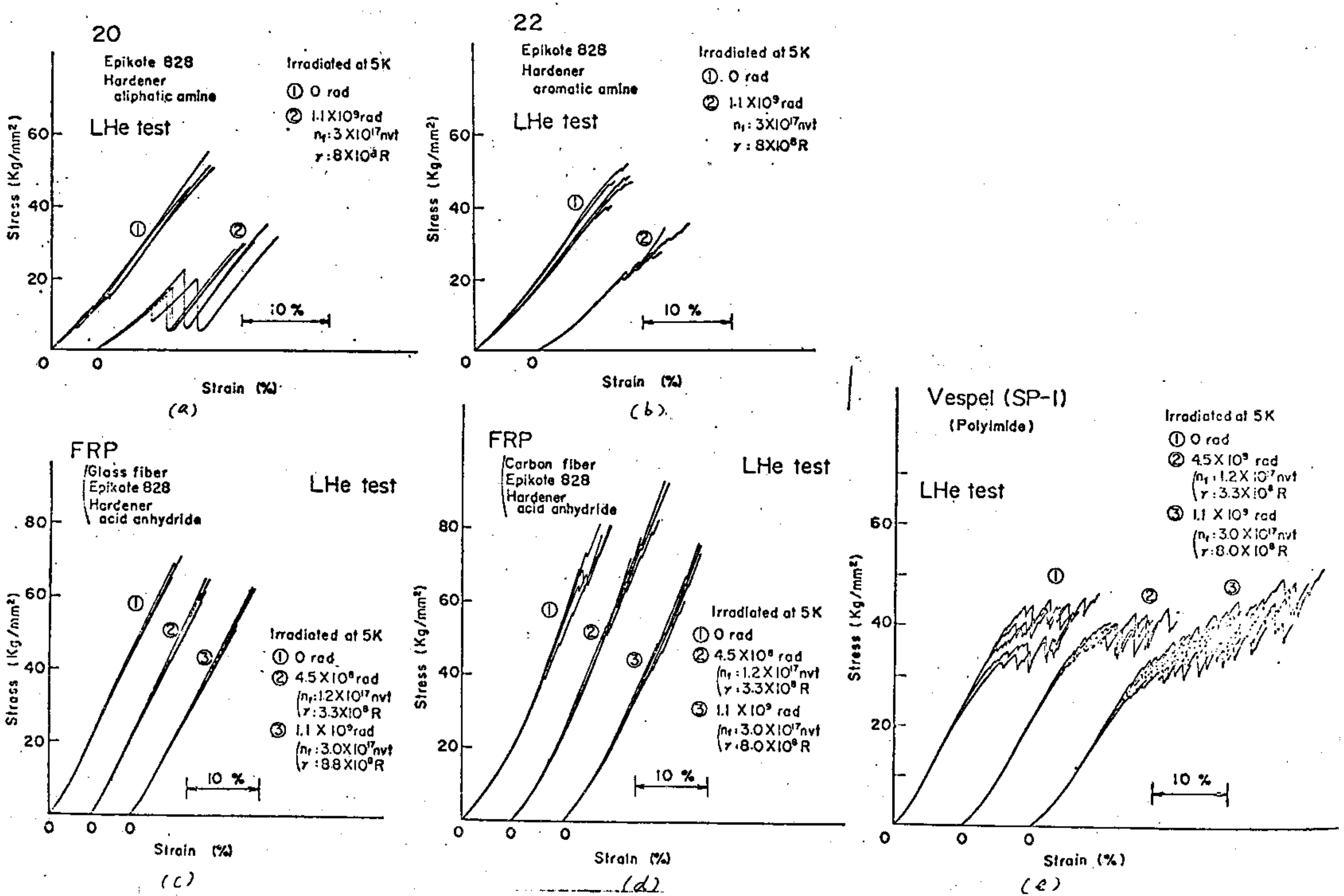

Fig.5.F.3 The stress-strain curves of Epikote 828 hardened by aliphatic amine(a), Epikote 828 hardened by aromatic amine(b), glassfiber reinforced epoxy(c), Carbon fiber reinforced epoxy(d) and Vespel(e) after fission neutron irradiation with γ ray at about 5K.

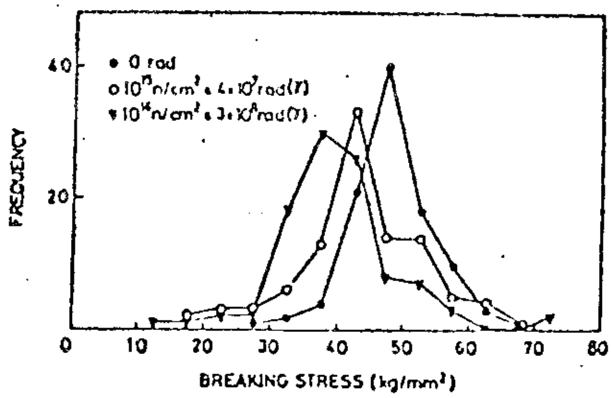

Fig.5.F.4(a) The change of frequency polygons of breaking stress caused by gamma irradiation.

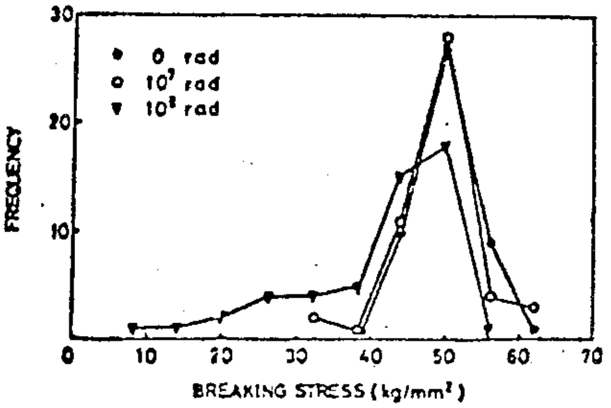

Fig.5.F.4(b) The change of frequency polygons of breaking stress caused by reactor irradiation ($E_n \geq 0.1$ MeV).

6. DATA BASE FOR NON-METALLIC MATERIALS CHOICE

B. Irradiation Effects on Graphite

B.1 Mechanical Properties of Graphite 1) 2)

B.1.1 Experimental Details

All the data tested below were obtained in JAERI by using JMTR, JRR-2 and HFR in Petten, the Netherlands. Neutron fluence ranged from 0.07×10^{21} to 3.9×10^{21} n/cm^2 (>0.18 MeV) and irradiation temperature ranged from 200 to 1,400°C. The Young's modulus was measured by a 100 KHz super-sonic longitudinal wave propagation velocity method. Tensile, compressive, and four point bending tests were conducted by using an Instron type testing machine at a crosshead speed of 0.5 mm/min at room temperature.

Tested materials are listed in Table 6.B.1.

B.1.2 Tensile and Compressive Stress-Strain Curves

Tensile and compressive stress-strain curves of unirradiated and irradiated nuclear graphites are shown in Figs. 6.B.1 and 2.

B.1.3 Young's Modulus

Relative Young's moduli of some graphites are given as a function of neutron fluence in Fig. 6.B.3 where E and E_0 are moduli of irradiated and unirradiated graphites, respectively.

B.1.4 Tensile Strength

Relative tensile strengths of graphites are shown as a function of neutron fluence in Fig. 6.B.4.

B.1.5 Compressive Strength and Compressive Fracture Strain

Relative compressive strengths and compressive fracture strains of some graphites are shown as a function of neutron fluence in Fig. 6.B.5.

B.1.6 Bending Strength

Relative bending strengths of graphites are shown as a function of neutron fluence in Fig. 6.B.6.

B.2 Irradiation Creep of Graphite

Irradiation creep strain of graphite can be expressed by

$$\varepsilon_c = \frac{\sigma}{E} + K_c \sigma \Phi \quad , \qquad (6.B.1)$$

where σ is applied stress, E is unirradiated Young's modulus in the direction of the creep, Φ is neutron fluence, and K_c is irradiation creep constant. The irradiation creep constant depends upon the irradiation temperature. Creep constant data are shown in Fig. 6.B.7 together with the data obtained in the other institutes.

B.3 Physical Properties of Graphite

B.3.1 Dimensional Changes[3)]

Petroleum coke near-isotropic graphite (SM1-24) and petroleum core fine-grained isotropic graphite (IG-11) were irradiated in HFR, Petten. Results of dimensional changes are shown in Figs. 6.B.8 and 9. Dimensional changes of isotropic high strength graphites (IG-11 and SM1-24) are smaller than those of anisotropic ones (H-327, etc.).

B.3.2 Thermal Expansion Coefficient[4)]

Thermal expansion coefficients of some graphites are shown as a function of neutron fluence in Figs. 6.B.10 and 11.

B.3.3 Thermal Conductivity[3)]

Thermal conductivity of SM1-24 and IG-11 graphites are shown as a function of testing temperature in Fig. 6.B.12.

B.3.4 Electrical Resistivity[3)]

Electrical resistivity of graphite has a parallel relation to thermal resistivity. Fig. 6.B.13(a) and (b) show the thermal conductivities of SM1-24 and IG-11 graphites irradiated in HFR with unirradiated data.

B.4 Chemical Reaction Rate of Graphite with Impurity Water Vapor in Helium[5)]

B.4.1 Chemical Reaction Rate of Neutron Irradiated Graphite

Figs. 6. B.14 and 15 show chemical reaction rate of irradiated and unirradiated graphites with impurity water vapor in helium. Generally reaction rates of irradiated graphites increases as compared with unirradiated ones.

B.4.2 Effect of Gamma-Ray Irradiation on the Chemical Reaction Rate

Gamma ray promotes the chemical reaction rate of graphite with water vapor in helium as shown in Figs. 6.B.16 and 17.

B.5 Pore Structures of Graphite[6)]

Mercury pore distribution curve of graphite changes during irradiation. Fig. 6. B.18~20 shows that the pore distribution curve of the irradiated material deviates from that of unirradiated one, and that the total porosity decreases during irradiation.

References

1) T. Oku, M. Eto, K. Fujisaki, JAERI-M 7647 (1978)

2) T. Oku, M. Eto, T. Arai, Proc. US-Japan Seminar on HTGR Safety Technology Vol.III, 20-1 (1978)

3) S. Nomura, J. Shimokawa, Y. Sasaki, T. Oku, H. Imai, et al., JAERI-M 8068 (1979)

4) H. Matsuo, private comunication

5) Y. Sasaki, H. Imai, S. Nomura, T. Kurosawa, K. Fujii, Proc. US-Japan Seminar on HTGR Safety Technology Vol.II, 1-1 (1978)

6) T. Oku, T. Usui, M. Eto, Y. Fukuda, Carbon, 15, 3 (1977)

Table 6. B.1 Room Temperature Properties of Tested Graphites

Coke	Brand	Forming	Density [g/cm^3]	Dir.	Young's Modulus [10^3kg/mm^2]	Poisson's Ratio	Tensile Strength [kg/mm^2]	Compressive Strength [kg/mm^2]	Bending Strength [kg/mm^2]
Gilsonite	IM-2	M	1.78	//	1.22	0.15	2.24	7.98	3.43
				⊥	1.21	0.18	2.12	7.31	3.51
	IM2-24	M	1.78	//	1.21	0.16	1.98	7.30	2.76
				⊥	1.30	0.20	2.18	7.09	3.18
	IE1-24	E	1.80	//	1.42	-	2.84	6.15	3.50
				⊥	1.18	-	1.54	5.32	-
Petroleum	7477PT	IM	1.74	//	0.98	0.12	2.24	8.49	3.48
				⊥	0.99	0.11	2.07	7.96	3.38
	SM1-24	M	1.77	//	0.95	-	1.68	5.44	2.81
				⊥	0.99	0.17	1.53	5.23	2.55
	IG-11	IM	1.78	//	1.00	0.14	3.43	8.89	4.40
				⊥	1.01	0.15	2.95	8.94	3.93
	H-327	E	1.78	//	1.51	-	1.23	3.20	2.60
				⊥	0.71	0.06	0.70	2.80	1.49

M=Molded, E=Extruded, IM=Isostatically Molded

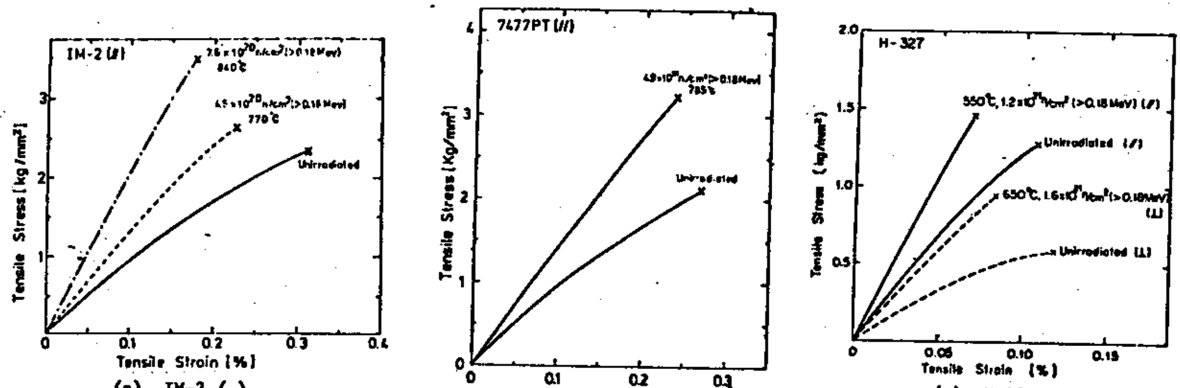

(a) IM-2 ( )

(b) 7477PT ( )

(c) H-327

Fig. 6.B.1 Tensile stress-strain curves of graphites

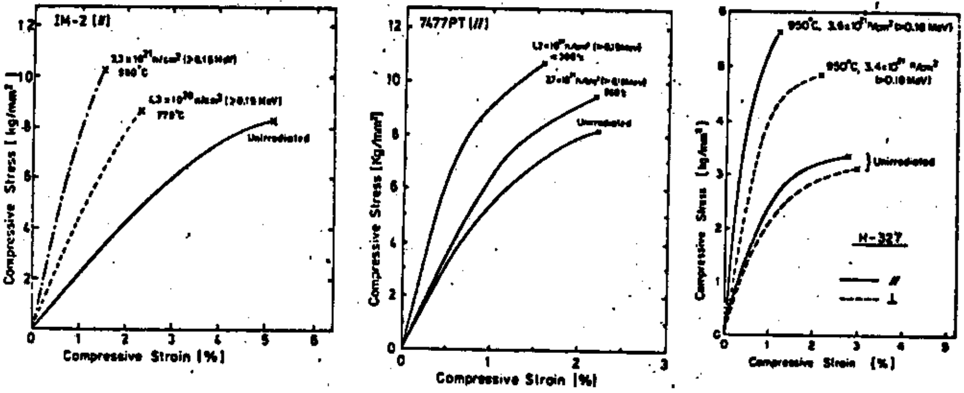

(a) IM-2 (//)

(b) 7477PT (//)

(c) H-327

Fig. 6.B.2 Compressive stress-strain curves of graphites

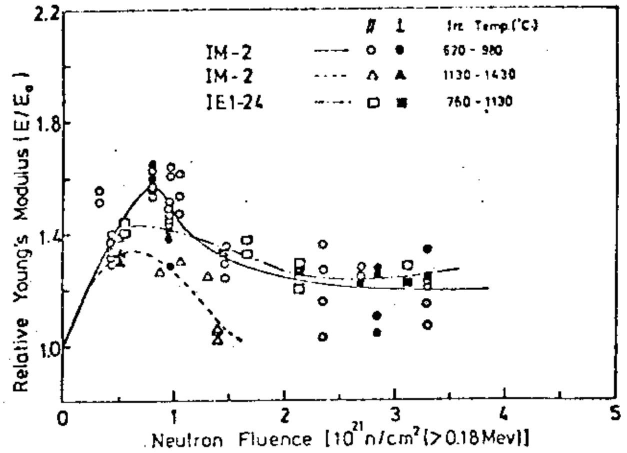

(a) IM-2 and IE1-24

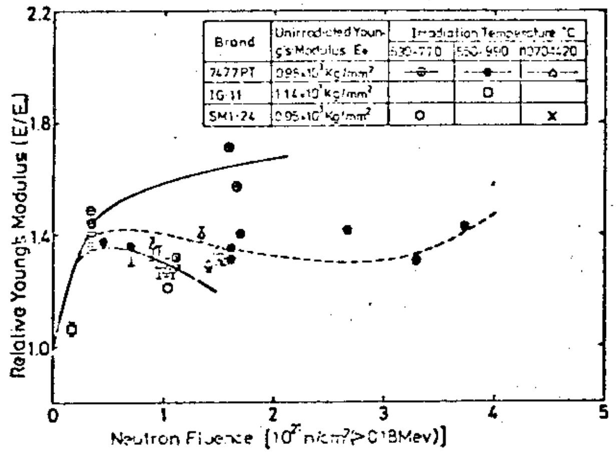

(b) 7477PT, SM1-24, and IG-11

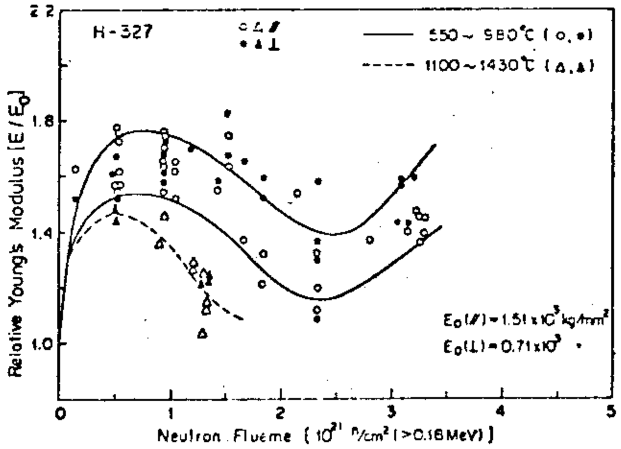

(c) H-327

Fig. 6.B.3 Relative Young's moduli of graphites as as a function of neutron fluence.

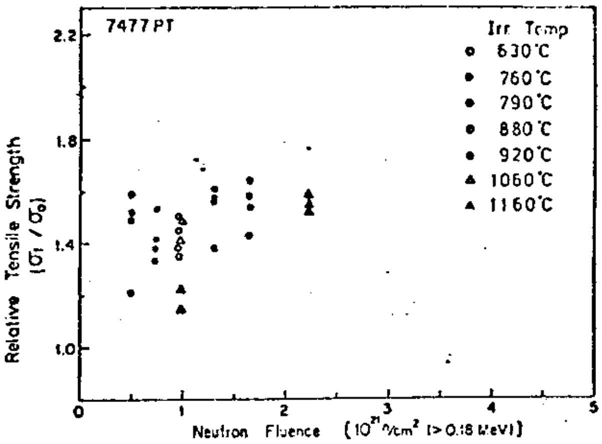

(a) 7477PT

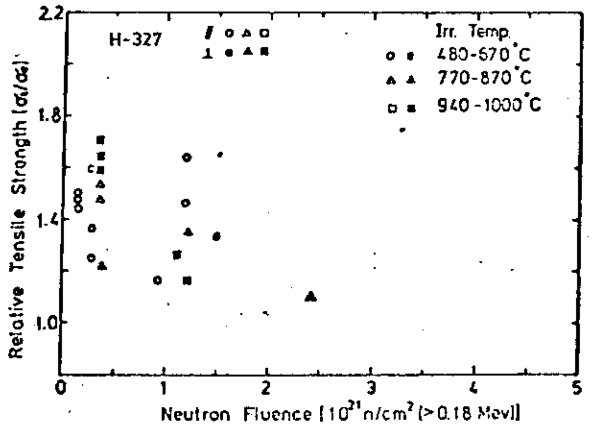

(b) H-327

Fig. 6.B.4 Relative tensile strengths of graphites as a function of neutron fluence.

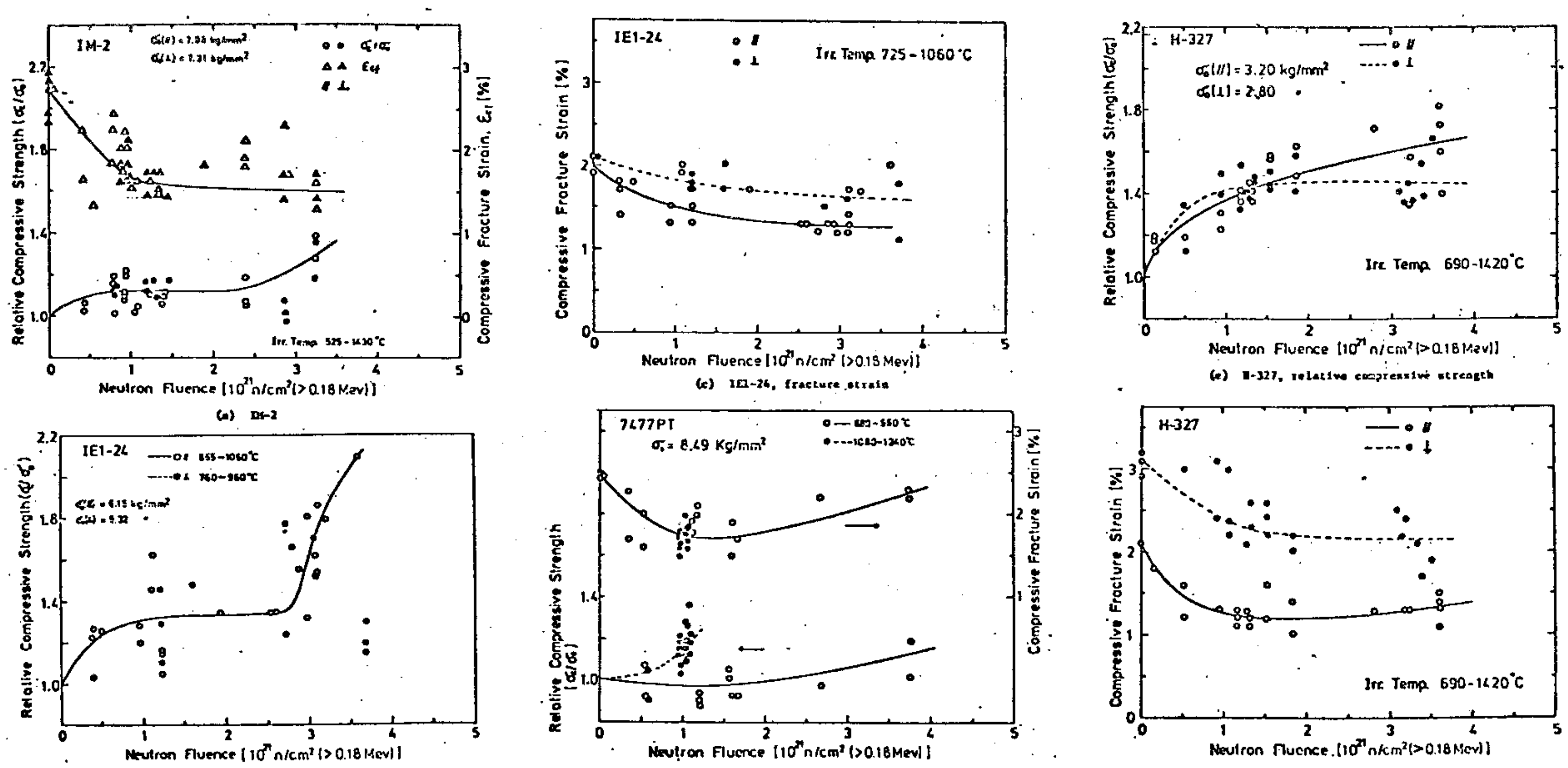

(a) IM-2

(c) IE1-24, fracture strain

(e) H-327, relative compressive strength

(b) IE1-24, relative compressive strength

(d) 7477PT

(f) H-327, fracture strain

Fig. 6.B.5 Relative compressive strengths and fracture strains of graphites as a function of neutron fluence.

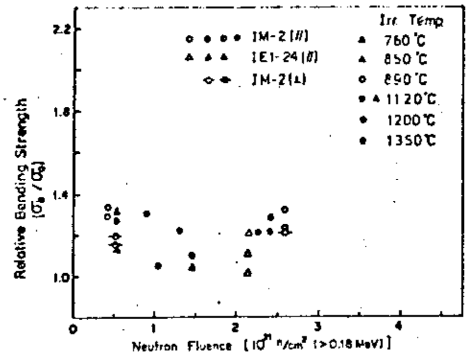

(a) IM-2 and IE1-24

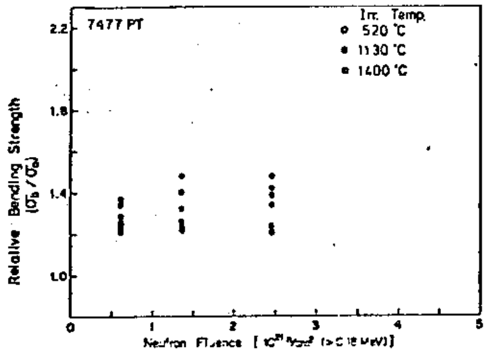

(b) 7477PT

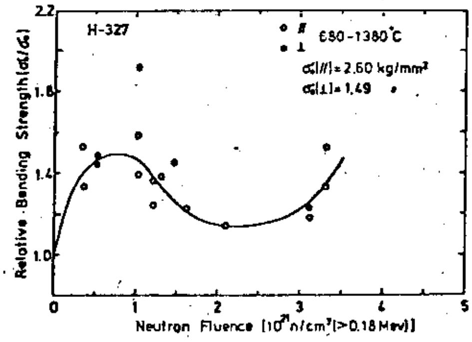

(c) H-327

Fig. 6.B.6 Relative bending strengths of graphites as a function of neutron fluence.

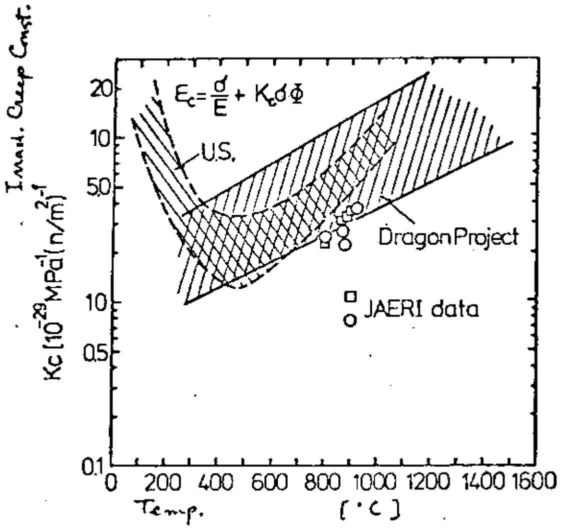

Fig. 6.B.7 Irradiation creep constant as a function of irradiation temperature.

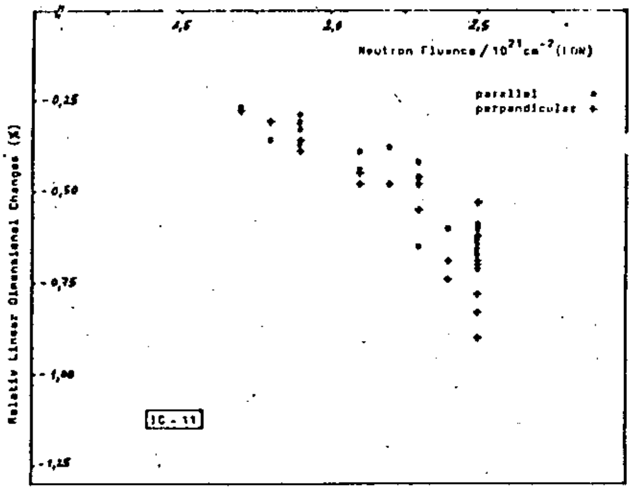

Fig. 6.B.8 Irradiation Induced Dimensional Changes for Graphite Grade IG-11.

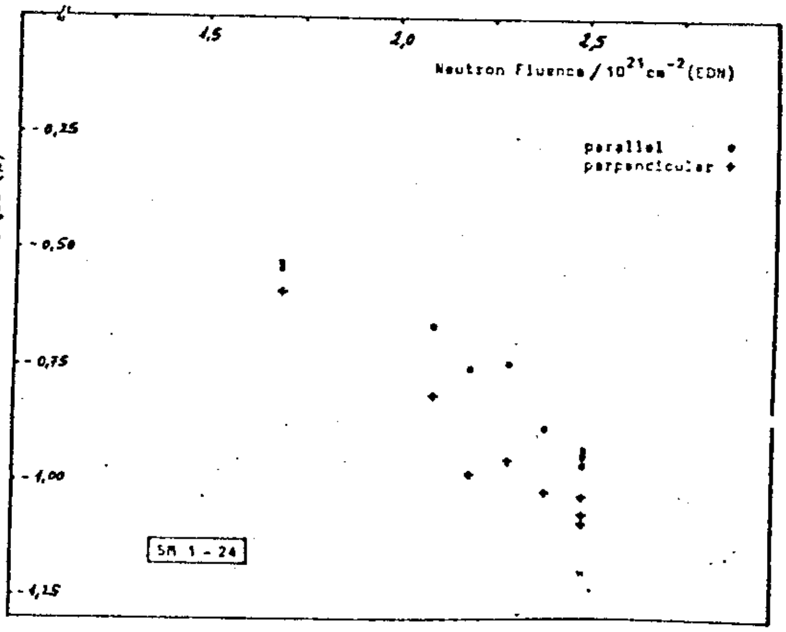

Fig. 6. B.9 Irradiation Induced Dimensional Changes for Graphite Grade SM1-24.

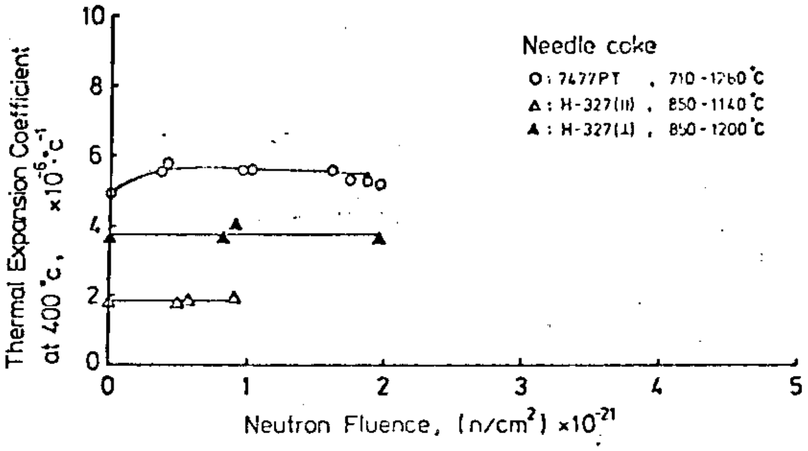

Fig. 6 .B.10 Changes in the thermal expansion coefficient of the needle coke graphite irradiated at high temperature in JMTR.

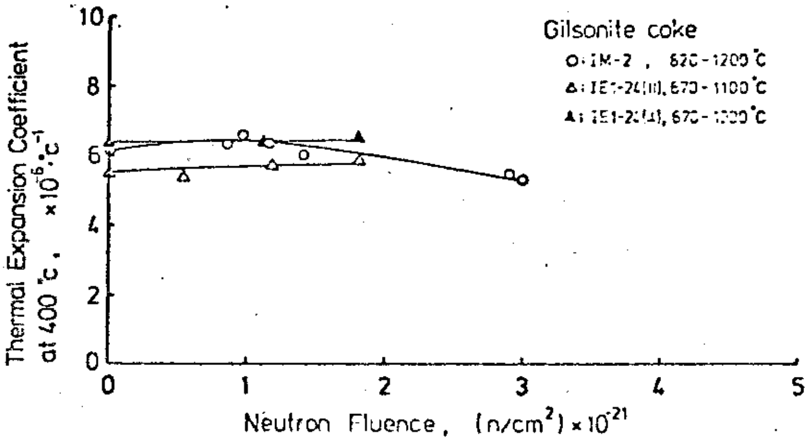

Fig. 6 .B.11 Changes in the thermal expansion coefficient of the gilsonite coke graphite irradiated at high temperature in JMTR.

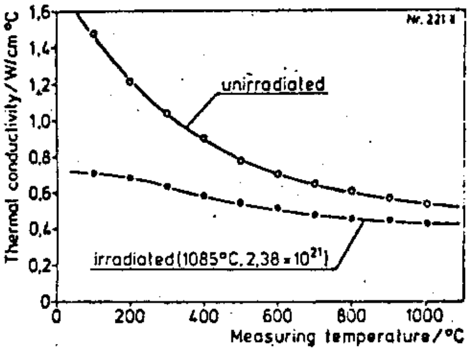

(a) Petroleum coke near-isotropic graphite (SM1-24, ∥)

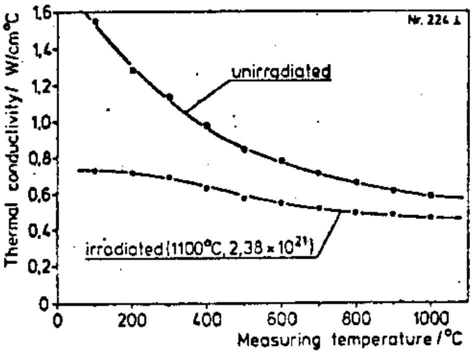

(b) Petroleum coke near-isotropic graphite (SM1-24, ⊥)

Fig. 6.B.12 Irradiation effects on the thermal conductivity of unirradiated and irradiated graphites.

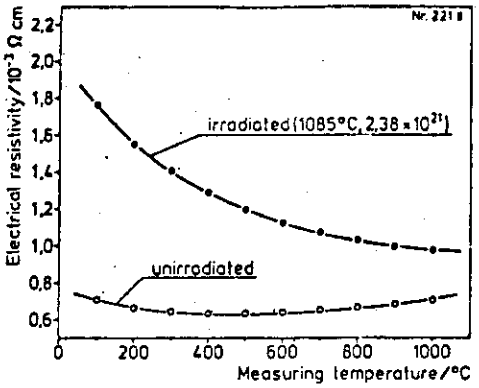

(a) Petroleum coke near-isotropic graphite (SM1-24, ∥)

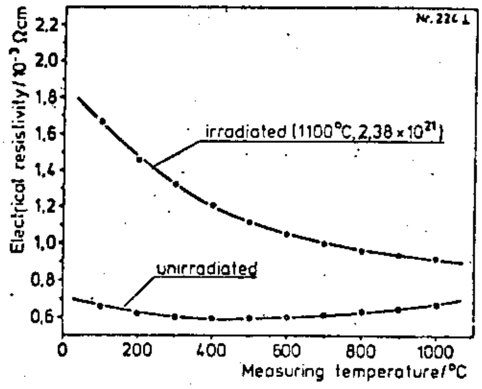

(b) Petroleum coke near-isotropic graphite (SM1-24, ⊥)

Fig. 6.B.13 Irradiation effects on the electrical resistivity of unirradiated and irradiated graphites.

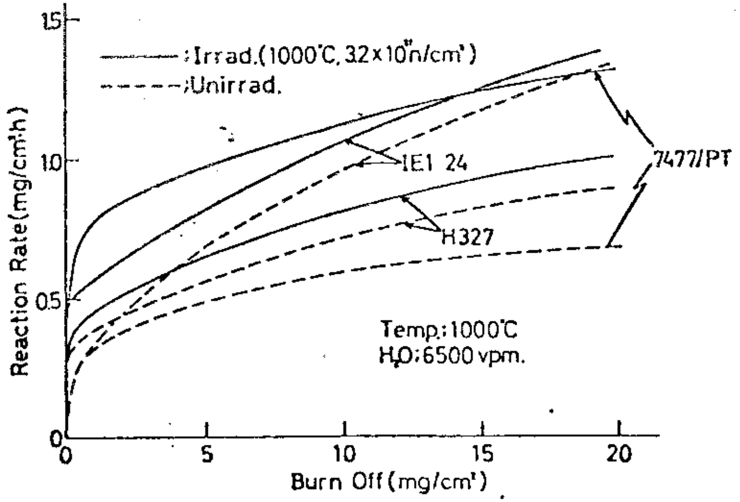

Fig.6.B.14 Irradiation effects on the reaction rate as a function of burnoff for various graphites.

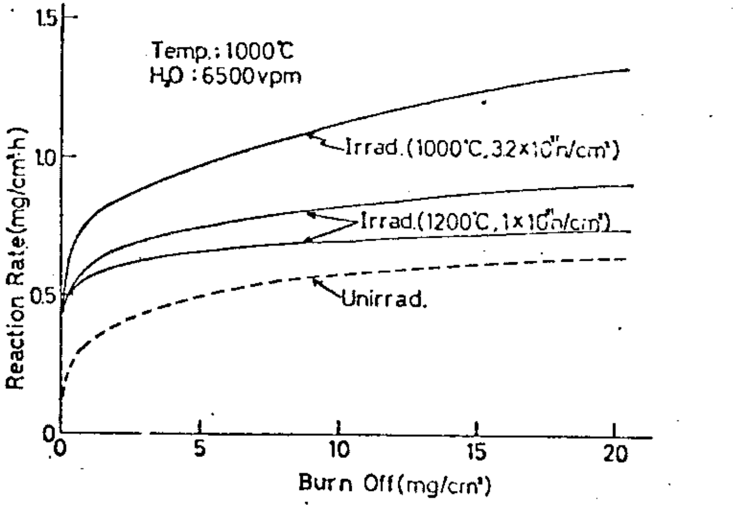

Fig.6.B.15 Neutron irradiation effects on the reaction rate as a function of burnoff for 7477/PT graphite.

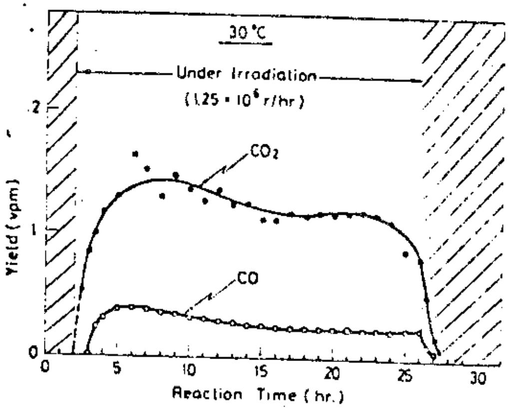

Fig.6.B.16 Carbon mono- and di-oxide formed in the reaction of 7477/PT with water vapor under gamma-ray irradiation.

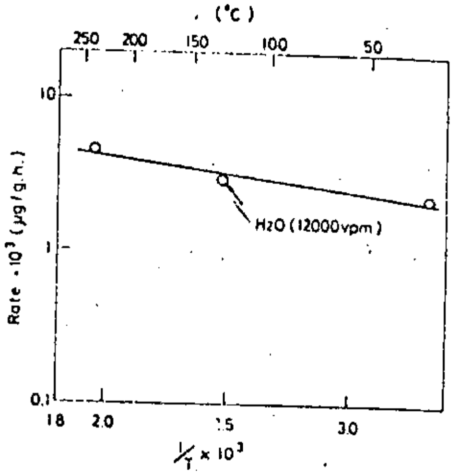

Fig.6.B.17 Temperature dependence of the rate of reaction of 7477/PT under gamma-ray irradiation.

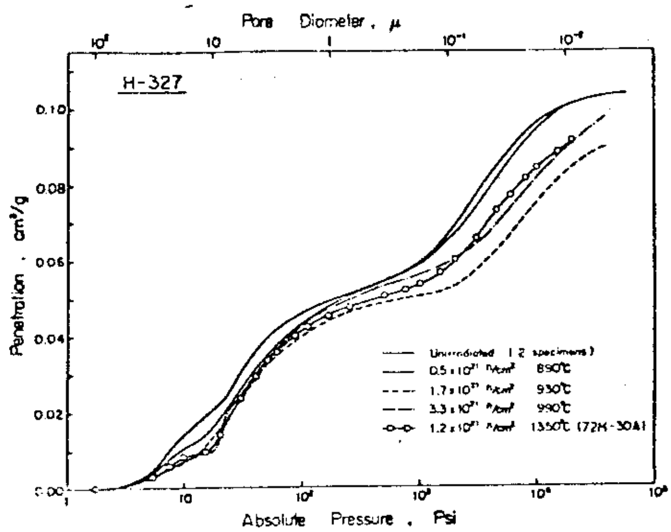

Fig.6. B.18 Effect of the high temperature irradiation on pore size distribution of H-327 graphite.

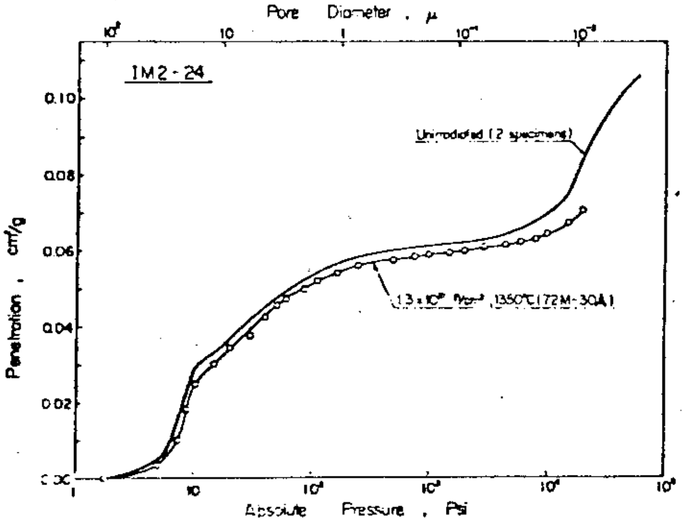

Fig. 6.B.19 Effect of the high temperature irradiation on pore size distribution of IM2-24 graphite.

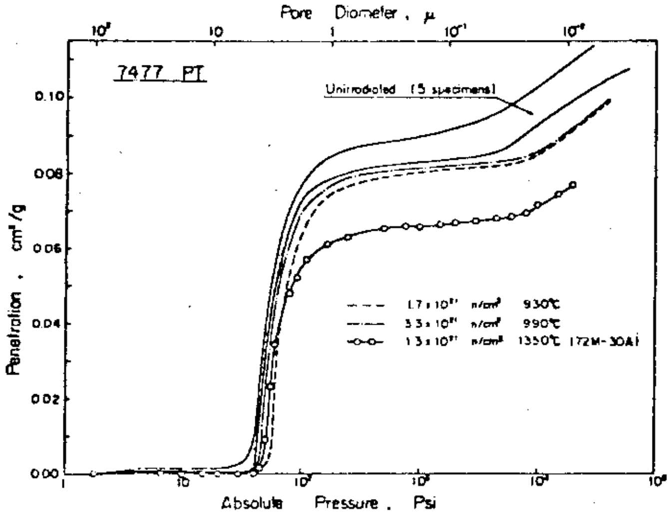

Fig. 6.B.20 Effect of the high temperature irradiation on pore size distribution of 7477/PT graphite.

7. DATA BASE FOR PLASMA WALL INTERACTION ASSESSMENT

Please refer Report of Group 3, Impurity Control.

8. STATE OF THE ART SUMMARY ON RELEVANT COATING TECHNOLOGY

Please refer Report of Group 2, First Wall.

9. OVERALL CONCLUSIONS AND OBSERVATIONS FOR MATERIAL DATA BASE WITH RESPECT TO INTOR

Appendix:

HOME WORKS BETWEEN SESSIONS 2 AND 3

At Session 2 of Workshop, the following requirements were give as home tasks between Sessions 2 and 3.

1) It has been proposed that water cooled alloys, operating at low temperatures (50 to 150°C) could be used as first walls in combination with high temperature (250-350°C) electricity producing stainless steel blankets. The reason for such a dual system has to do with the thermal stresses associated with the possibility of abnormally high heat fluxes (>50 W-cm^{-2}) in some regions of the first wall.

   Each country is asked to document the case for and against the use of Al alloys in this configuration.
2) A more complete assessment of high energy (14 MeV or spallation sources) neutron facilities is necessary. Each country should state what facilities and what time table for their operation is envisaged.
3) The reaction of hydrogen with carbon (or carbides) needs to be documented. The Japanese have agreed to provide information on their most recent erosion experiments.
4) The maximum allowable thermal stresses for potential INTOR first wall materials need to be determined. Each country will provide a graph of such stresses with supporting data used in the calculations.
5) The wall erosion rates due to energetic ions leaking from the plasma shall be presented. The effect of non-uniform particle leadage from the magnetic ripple between TF coils should be estimated. Each country shall make a table of particle fluxes assumed, sputtering coefficients assumed, energies of ions and neutrals, etc.
6) The use of TZM has been proposed for INTOR. The Japanese have agreed to provide information on the justification of that material for INTOR conditions.

7) The ultimate limitation for the TF coil useful lifetime appears to be connected with damage to the stabilizer material. Each country will examine data in its possession about damage rates of Cu and/or Al at low temperatures and the annealing of such damage at higher temperatures. Particular attention will be paid to the interactions of such damage with dislocations produced by plastic deformation before irradiation commences.

8) The data base maps (dpa vs. He content) for austenitic steels, ferretic steels, Ti alloys and Al alloys should be constructed for the October meeting. The data should only be for the host country (or EC). Where no data is available, it should be so stated.

9) The data base on coatings needs to be expanded. Each country should state its current research program and the levels of irradiation to which the coatings have been subjected.

10) The chemical stability of the Li_2O-LiOT system needs to be documented. The Japanese have consented to establish the weight loss rates for a Li_2O breeding system operating under INTOR conditions.

11) Each country shall estimate and document the major R & D needs for the materials to be used in INTOR. This assessment should only consider those items of top priority, and estimates of man-years of effort required (up to 1985) to solve those problems will be made.

Homework between Sessions 2 and 3

1. Use of water cooled alloy

   We do not consider it.

2. Program of neutron irradiation facilities

   The program is not yet formally fixed.

3. Reaction of hydrogen with carbon

   See Appendix III "Chemical Sputtering of Low Z Materials" of "Impurity Control" (report of design options).

4. Maximum allowable thermal stresses

   See Report of Group 2.

5. Particle fluxes, sputtering coefficients and energies of particle

   See Report of Group 2 of Session 2.

6. The use of molybdenum alloy for INTOR (K. Shiraishi)

   The most serious problem for use of molybdenum alloys as protection wall in INTOR is neutron-irradiation embrittlement. Commercial pure molybdenum and TZM could not be used in the nuclear environment. A certain molybdenum alloy is expected to be possibly used for INTOR. For example, electron-beam-melted Mo-0.5%Nb alloy shows about 3 % in total elongation at room temperature tensile testing after neutron irradiation to 1.2×10^{20} n/cm^2 at 800°C. In contrast to the damage induced in powder-metallurgied molybdenum and arc-melted TZM, the damage of the electron-beam-melted Mo-0.5%Nb alloy recovers almost completely on annealing at higher temperatures. In addition, the irradiated alloy shows good ductility in testing at temperatures above 400°C. Thus, the electron-beam-melted alloy has a good prospect for use in nuclear environment at high temperature.

   Intensive R & D are required to utilize the molybdenum alloy for the protection wall in INTOR. The items of top priority are

   - high temperature mechanical properties including recrystallization behavior in relation to service condition,

- radiation damage, especially ductility at room temperature, as a function of neutron fluence, temperature and helium content,
- coating of low Z materials,

and

- fabrication and joining technology.

7. Damage rates of Cu and Al and annealing of the damage at room temperature (S. Takamura)

1) Damage rates

Table Al shows typical data of resistivity increase by fast neutron irradiation. From these data, the resistivity increase at fast neutron fluence of 10^{18}nvt in Cu and Al are about 7 × $10^{-8}\Omega$cm and 23 × $10^{-8}\Omega$cm, respectively.

For cold worked Cu specimen, Blewitt et al.$^{1)}$ observed that the damage rate was approximately 10 % greater than that of annealed one. Swanson et al.$^{2)}$ also reported the similar result. In our experiments,$^{3)}$ the enhancement of 13~14 % was observed, where cold worked specimens were prepared by twisting at room temperature and annealed at 50°C.

2) Recovery

The fraction not recovered at room temperature to the total resistivity increase due to neutron irradiation is about 15 % in Cu as shown in Table Al. In Al, the resistivity increase by irradiation recovers completely.

The recovery is enhanced below room temperature by cold work and the recovered amount is approximately 9 % greater than that of annealed one.

1) T. H. Blewitt et al. : ORNL Report No.2614 (1958) 67.
2) M. L. Swanson et al. : Canad. J. Phys. 42 (1964) 1605.
3) S. Takamura et al. : J. Phys. Soc. Japan 26 (1969) 1120.
4) J. A. Horak et al. : Nucl. Technology 27 (1975) 416.
5) J. A. Horak et al. : Phys. Stat. So. (a) 9 (1972) 721.
6) M. Nakagawa et al. : Phys. Rev. B 16 (1977) 5285.
7) S. Takamura et al. : J. Phys. Soc. Japan 30 (1971) 1360.

8. The data base maps for structural materials

No data is available.

9. Data base and current research program on surface coatings

(Y. Murakami)

The concept of a first wall coating originated several years ago in the tokamak fusion community. It has received steadily-increasing attention, probably because it permits selection of one material for the first wall with optimum structural and electrical properties and another material for the surface with optimum properties such as minimum plasma contamination and wall erosion under exposure to plasma.

The incidence of energetic and/or chemically active particles on the first wall surface gives rise to the introduction of impurities into the tokamak plasma by particle-surface interaction. These impurities will lose energy by line and recombination radiation and bremsstrahlung, and the higher atomic number impurities will radiate greater amounts of power. Recently, there is particular interest in the use of low-Z surface coatings for the first wall.

The possible coating techniques which might be used include in-situ coating with insertible deposition devices and external coating which will be done before assembly or by removal of components. In JAERI, a technique of impurity control by in-situ coating with titanium has been applied successfully to JFT-2$^{1)}$ and JFT-2a (DIVA)$^{2)}$. Titanium was evaporated from Ti-balls* in a high vacuum and was deposited on the limiters and walls during the intervals between successive shots. As to the coating technique, however, there is some concern that the coated films may peel and cause a deterioration in the system.

Recently, a testing was made on the vacuum coating of molybdenum. In this case, peeling of the coated films occured at the thickness of 10 μm. In order to improve the bondability between the coating material and the substrate surface, an rf-sputtering method was proposed as an in-situ coating technique. Figure 1 shows a schematic drawing of the insertible sputtering device for molybdenum coatings$^{3)}$. It applies the principle of the coaxial magnetron. Argon plasma is confined along the cylindrical target by magnetic field, in which the target is sputtered by argon ion bombardment. The arc burning relation between argon pressure and magnetic field is shown in Fig. 2 for the rf power of 4 kW. The deposition rate is sufficiently high as shown in Fig. 3. From the

---

* Trademark of Varian

experiment, it was found that the bondability of the coated films to molybdenum substrates depends on the deposition rate and the substrate temperature. Thick films (up to 45 μm) deposited at a rate of 200 Å/min and 500°C did not peel even after 126 thermal cycles between 50 and 500°C.

More recently, in-situ coatings of walls with carbon have been performed tentatively in JFT-2a by using the coaxial magnetron type sputtering devices$^{4)}$. The deposition was done at room temperature. In this case, the carbon films were partially peeled off and carbon powders were formed inside the vacuum vessel. This may be due to low substrate temperature during deposition. The optimization of in-situ coating conditions will be made with an exclusive machine called JVX-I (JAERI Vacuum Experiment I) in the JT-60 project. The materials to be tested include molybdenum, titanium, aluminum and carbon.

As to external coatings, JAERI has completed a preliminary estimate of coating requirements and is now preparing a coating development plan for JT-60. The R&D items include the preparation of industry manufactured large samples, the measurement of physical and chemical erosion and vacuum properties, the evaluation in thermal shock and low cycle thermal fatigue, and the intorduction of samples as a limiter and wall material into existing tokamaks. The low-Z coating materials will be selected from C, SiC, Ti, TiB_2, TiC, TiN, B_4C, etc.

Generally, the criteria for an ideal adherent coating-substrate system are that there are no stresses introduced at the interface, either during formation or in service, and that there are intimate contacts between the coating material and the substrate surface. The possible external coating techniques include evaporation or sputtering, ion plating, chemical vapor deposition (CVD), plasma spraying and electroplating. Of direct interest to the coatings development program are the low-Z surface coatings on refractory metals by ion plating and CVD being pursued by NRIM in cooperation with JAERI, the work at Hokkaido University on the SiC coating by rf-sputtering$^{5)}$, and the work at ULVAC on the TiN coating by ion plating$^{6)}$. About physical features, see Appendix-1 of "impurity control".

References of Item 9.

1) S. Konoshima, et al., J. Nucl. Materials 76&77 (1978) 581.

2) H. Maeda, et al., 7th释nternl. Conf. on Plasma Physics and Controlled Nuclear Fusion Research, Insbruck, 1978, T-3-1.

3) T. Tazima, JAERI-M 7717 (1978).

4) T. Abe, et al.,in preparation for publication.

5) Y. Hiroshita, et al.,7th Internl. Vacuum Metallurgy Conference on Special Melting and Metallurgical Coatings, San Diego, 1979.

6) S. Komiya, et al., ibid.

10. Chemical stability of Li_2D-LiOT system (S. Nasu)

1) Thermal decomposition of LiOH (1)

Thermal decomposition of powdered LiOH is now being investigated by thermobalance technique as a function of temperature, atmosphere, vessel volume and sample weight. The following preliminary results are already obtained.

(1) Assuming the thermal decomposition reaction of $2LiOH(s) \rightarrow Li_2O(s) + H_2O(g)$, conversion in vacuum is determined to be above 0.99 in the temperature range of 310 to 550°C, and 1.00 to 1.01 above 550°C. It is probably due to the thermal decomposition of impurity Li_2CO_3 in the LiOH sample that conversion is above 1.00.

(2) Activation energies of the thermal decomposition reaction of LiOH are obtained to be 112 ± 2KJ mol^{-1} (242~323°C) and 82 ± 3KJ mol^{-1} (323 to 419°C) for LiOH of 200 mg in a vessel of 18mmϕ × 17mml. On the other hand, for LiOH of 180mg in a vessel of 6.2mmϕ × 19mml, activation energy of the reaction is determined to be 123 ± 4KJ mol^{-1}.

(3) The vessel diameter dependence of the rate constant for the reaction is examined. For example, at 340°C, the rate constant is 1.4×10^{-9} sec^{-1} for the bigger vessel, and 5.3×10^{-6} sec^{-1} for the smaller vessel, that is, the bigger the vessel diameter is, the faster the reaction is.

(4) The sample weight dependence of the reaction shows that the heavier the sample weight is, the smaller the rate constant is.

2) Reaction of Li_2O pellets with H_2O in air (2)

Reaction of Li_2O pellets with H_2O in air is now being investigated. The following preliminary results are obtained.

(1) Below 50 % relative humidity, the Li_2O pellets seem hardly

to react with H_2O at 25°C.

(2) Above 60 % relative humidity, the Li_2O pellets react appreciably with H_2O at 25°C. For example, for a pellet of about 11mmϕ × 6mml, about 1 % of Li_2O reacts with H_2O at 60 % relative humidity at 25°C for 110 hours.

(3) Carbon dioxide (CO_2) may play an important role in the reaction of Li_2O with H_2O in air.

(1) T. Takahashi and S. Nasu; unpublished data

(2) T. Takahashi and S. Nasu; unpublished data

11. Major R & D needs for the materials to be used in INTOR (K. Shiraishi)

1) Neutron irradiation effects on austenitic stainless steel for solution treated, cold worked and welded specimens

(i) Fatigue properties 300~500°C
- Non-irradiation tests
- Post-irradiation tests on crack initiation and propagation as a function of dpa and He content

(ii) Tensile tests to make temperature - dpa - He content map (300~550°C, 0~100 dpa, 0~1000 appmHe)

(iii) Swelling with and without applied stress under irradiation of controlled He/dpa ratio

(iv) Creep under irradiation of controlled He/dpa ratio

(v) Fundamental research to establish the correlation between fission reactor and fusion reactor irradiations

2) Research on Li_2O

(i) Chemical stability of Li_2O-LiOT system

(ii) Tritium release under irradiation

(iii) Mechanical properties including creep deformation and thermal shock

(iv) Fundamental research on diffusion, radiation damage, etc.

3) Establishment of the coating technology

(i) Selection of coating material and procedure

(ii) Sandarization of evaluation for coating material and procedure

(iii) Characterization of coated materials
(iv) Estimation of surface damage

4) Evaluation of radiation damage on the materials for stabilizer and insulator of TF coil and divertor plate

5) Development of molybdenum alloy, if necessary

Table A1 Damage rates and annealing at room temperature

ρ_o : residual resistivities at 4.2K~4.5K prior to irradiation
ρ_i : resistivity increases by fast neutron irradiation
ϕ_t : fast neutron fluence
f : fraction not recovered at 300K

	ρ_o ($\times 10^{-9}\Omega$cm)	ρ_i ($\times 10^{-9}\Omega$cm)	ϕ_t ($\geq$0.1MeV)	f (%)	
Cu	1.7	40.6	5.8×10^{17}	15	Horak[4)]
	0.8	116	2×10^{18}		Horak[5)]
	1.2	~70	1×10^{18}	16	Nakagawa[6)]
	1.5	2.9		26	Takamura[3)]
	5.8(cold worked)	3.2	4.2×10^{16}	20	
	9.2(cold worked)	3.2		17	
	—	6.8	1.1×10^{17}	14	Takamura[7)]
	—	2.5	0.36×10^{17}		
Al	1	322	2×10^{18}		Horak[5)]
	1.8	~240	1×10^{18}		Nakagawa[6)]